TU WIEN
DEPARTMENT OF
GEODESY AND
GEOINFORMATION

DISSERTATION

Towards instantaneous PPP convergence using multiple GNSS signals

Ausgeführt zum Zwecke der Erlangung des akademischen Grades eines/r Doktors/in
der technischen Wissenschaften unter Leitung von

Ao. Univ-Prof. Dipl.-Ing. Dr.techn. Robert Weber
E120-4
Department für Geodäsie und Geoinformation
Forschungsbereich Höhere Geodäsie

eingereicht an der Technischen Universität Wien
Fakultät für Mathematik und Geoinformation

von

Marcus Franz Glaner
Matrikelnummer: 1027081

Wien, im August 2022

Unterschrift (Verfasser/in)   Unterschrift (Betreuer/in)

Eidesstaatliche Erklärung

Ich erkläre an Eides statt, dass die vorliegende Arbeit nach den anerkannten Grundsätzen für wissenschaftliche Abhandlungen von mir selbstständig erstellt wurde. Alle verwendeten Hilfsmittel, insbesondere die zugrunde gelegte Literatur, sind in dieser Arbeit genannt und aufgelistet. Die aus den Quellen wörtlich entnommenen Stellen, sind als solche kenntlich gemacht.

Das Thema dieser Arbeit wurde von mir bisher weder im In- noch Ausland einer Beurteilerin/einem Beurteiler zur Begutachtung in irgendeiner Form als Prüfungsarbeit vorgelegt. Diese Arbeit stimmt mit der von den Begutachterinnen/Begutachtern beurteilten Arbeit überein.

Wien, im August 2022

Danksagungen

Zu Beginn dieser Arbeit möchte ich mich herzlichst bei Prof. Robert Weber bedanken - ohne dich würde es diese Arbeit nicht geben. Danke für all deine präzisen Verbesserungsvorschläge, deine Offenheit und Anregungen und dass du mir die Möglichkeit eröffnet hast, in einem so faszinierenden Themenbereich arbeiten zu können.

Außerdem möchte ich mich bei Prof. Philipp Berglez und Prof. Markus Rothacher für die Zweitbegutachtung meiner Arbeit bedanken. Danke für das Interesse und die wertvollen Kommentare.

Ein weiterer Dank geht an Prof. Johannes Böhm für seine Unterstützung und die großartige Leitung unserer Forschungsgruppe der Höheren Geodäsie.

Danke an alle Kolleg:innen der GNSS- und auch VLBI-Gruppe für die tolle Arbeitsatmosphäre, Zusammenarbeit und große Hilfsbereitschaft. Ich genieße jeden Tag in diesem wunderbaren Umfeld.

Ganz besonders bedanke ich mich bei meinen lieben Eltern für ihre immerwährende Unterstützung und einfach alles!

Zu guter Letzt möchte ich mich bei meiner eigenen kleinen Familie - Sabine, Felix und ??? - bedanken. Ich liebe euch und dich, Sabine, ganz besonders.

Kurzfassung

In den letzten Jahrzehnten hat sich Precise Point Positioning (kurz PPP, Präzise Einzelpunkt-bestimmung) als Technik etabliert, um, basierend auf den Signalen von Globalen Navigationssatellitensystemen (GNSS), die Position der Nutzer:innen zu berechnen. Mit PPP wird eine Positionsgenauigkeit im Zentimeter- oder sogar Millimeter-Bereich erreicht. Dabei werden Code- und Phasen-Beobachtungen, präzise Satellitenprodukte (z.B. Bahnen, Uhren und Biases) und ausgeklügelte Algorithmen verwendet. Ein derzeit noch großer Nachteil von PPP ist die meist beträchtliche Konvergenzzeit - also jene Zeitdauer, bis die Koordinaten den Zentimeter-Genauigkeitsbereich erreicht haben. Typischerweise benötigt eine PPP-Lösung, basierend auf GPS-Beobachtungen auch bei guter Satellitengeometrie, 20-30 Minuten um Koordinaten-Konvergenz zu erreichen.

Das Hauptziel dieser Arbeit ist die Entwicklung von PPP-Ansätzen, welche die Konvergenzzeit der Koordinaten so weit wie möglich reduzieren. Dabei werden die Multi-Frequenz-Signale von allen global funktionstüchtigen GNSS zur Berechnung der Nutzer-Position verwendet. Darüber hinaus wird das sogenannte „uncombined model" als Alternative zum konventionellen PPP-Ansatz, welcher die ionosphären-freie Linearkombination verwendet, eingeführt. Dieses flexible PPP-Model basiert auf den rohen GNSS-Beobachtungsgleichungen und bietet mehrere Vorteile gegenüber der ionosphären-freien Linearkombination. Zum einen weisen die GNSS-Grundbeobachtungen ein geringeres Signalrauschen auf und zum anderen können ionosphärische Pseudobeobachtungen gewichtet in die Berechnung der PPP-Lösung einfließen, was zum „uncombined model with ionspheric constraint" führt. Außerdem werden die Phasen-Mehrdeutigkeiten in beiden PPP Modellen ganzzahlig fixiert.

Die gezeigten Ansätze und Algorithmen sind in *raPPPid*, dem PPP-Modul der *Vienna VLBI and Satellite Software* (VieVS), implementiert. Diese Software wurde vom Autor im Zuge dieser Dissertation entwickelt. Mit raPPPid werden für statische GNSS-Empfänger unter guten Bedingungen Koordinaten-Konvergenzzeiten von einer Minute oder kürzer erreicht.

Abstract

Over the past decades, the principle of Precise Point Positioning (PPP) has become a well-established technique for determining the user's position with Global Navigation Satellite Systems' (GNSS) signals. A position accuracy at the centimeter or even millimeter level is accomplished by using code and phase observations, exploiting precise satellite products (e.g. orbits, clocks, and biases), and applying sophisticated algorithms. However, the convergence time until the coordinates have reached this accuracy is well known as the primary concern of PPP. Typically, the convergence time of a PPP solution using GPS observations is 20-30 minutes, even with favorable satellite geometry.

The main objective of this thesis is to develop PPP processing schemes reducing the coordinate convergence time as far as possible. Therefore, multi-frequency signals of all four globally-working GNSS are exploited and used to estimate the user's position. The uncombined model is developed as an alternative to the observation model of the conventional PPP approach using the ionosphere-free linear combination. This flexible model is based on the raw GNSS observation equations and shows several benefits compared with the ionosphere-free linear combination. For example, the raw observation noise is preserved and ionospheric pseudo-observations are included in the calculation of the PPP solution, resulting in the uncombined model with ionospheric constraint. Finally, integer ambiguity resolution is performed in the conventional as well as the uncombined model.

The presented approaches, models, and algorithms are implemented in *raPPPid*, the PPP module of the *Vienna VLBI and Satellite Software* (VieVS). This software was developed in the course of this thesis. With raPPPid, convergence times of 1 minute or below to centimeter-level position accuracy are achieved for static receivers under good conditions.

Contents

Contents

Contents

List of Figures

List of Tables

List of Abbreviations

AC Analysis Center

ANTEX Antenna Exchange (ANTEX) format

APC Antenna Phase Center

ARP Antenna Reference Point

BDS BeiDou Navigation Satellite System

BNC BKG Ntrip Client

CNES Centre National d'Etudes Spatiales

CDMA Code Division Multiple Access

CODE Center for Orbit Determination in Europe

COM Center of Mass

DCB Differential Code Bias

DSB Differential Signal Bias

ECEF Earth Centered Earth Fixed

EPOSA Echtzeit-Positionierung-Austria

ESA European Space Agency

EW Extra-Wide-Lane

FCB Fractional Cycle Biases

FDMA Frequency Division Multiple Access

FOC Full Operational Capability

GDV Group Delay Variation

GEO Geostationary Earth Orbit

GF Geometry-free

GIM Global Ionosphere Map

GLONASS Globalnaja Nawigazionnaja Sputnikowaja Sistema

GNSS Global Navigation Satellite System(s)

GPS Global Positioning System

GPT3 Global Pressure and Temperature 3

HMW Hatch-Melbourne-Wübbena

HAS (Galileo) High Accuracy Service

ICD Interface Control Document

IERS International Earth Rotation and Reference Systems Service

IF Ionosphere-free

IFCB Inter-Frequency Clock Bias

IGS International GNSS Service

IGSO Inclined Geostationary Orbit

IOD Issue of Data

IRC Integer Recovery Clock

ISB Ionosphere-free Signal Bias

ITRF International Terrestrial Reference Frame

ITRS International Terrestrial Reference System

LAMBDA Least-squares AMBiguity Decorrelation Adjustment

LC Linear Combination

LLI Loss of Lock Index

los line-of-sight

MEO Medium Earth Orbit

MGEX (IGS) Multi-GNSS Experiment

ML Medium-Lane

MP Multipath

NL Narrow-Lane

Ntrip Network Transport of RTCM via Internet Protocol

ORBEX Orbit Exchange (format)

OSB Observable-specific Signal Bias

PC Phase Center

PCO Antenna Phase Center Offset

PCV Phase Center Variation

PPP Precise Point Positioning

PPP-AR PPP with integer Ambiguity Resolution

QZSS Quasi-Zenith Satellite System

RINEX Receiver Independent Exchange

RTCM Radio Technical Commission for Maritime Services

RT Real-Time

LIST OF ABBREVIATIONS

RTS IGS Real-Time Service

RTK Real-Time Kinematik

SGG School of Geodesy and Geomatics, Wuhan University

SISRE Signal-in-space range error

SNR Signal to Noise Ratio

SPP Single Point Positioning

SSR State Space Representation

SD Single-Difference(d)

STD standard deviation

TEC Total Electron Content

TECU Total Electron Content Unit

TTFF Time To First Fix

TUG Graz University of Technology

UC Uncombined

UPD Uncalibrated Phase Delay

UTM Universal Transverse Mercator

VMF3 Vienna Mapping Functions 3

VTEC Vertical Total Electron Content

WG Working Group

WL Wide-Lane

ZHD Zenith Hydrostatic Delay

ZTD Zenith Total Delay

ZWD Zenith Wet Delay

1. Introduction

1.1. Precise Point Positioning

Since Malys and Jensen (1990), Héroux and Kouba (1995) and Zumberge et al. (1997) have introduced the concept, Precise Point Positioning (PPP) has proven itself as a substantial GNSS positioning method. Nowadays, PPP is used for various scientific and commercial applications (Kouba et al., 2017).

The concept is quite simple: With the most accurate satellite orbits, clocks, and biases available, the user's position is calculated. Therefore, PPP can be seen as a strongly enhanced version of Single Point Positioning (SPP). In the author's view, PPP is the most elegant, direct, and instructive application of the GNSS observation equations because all relevant error sources have to be considered properly.

Typically, PPP exploits multi-frequency code and phase observations of a single GNSS receiver and precise satellite products (orbits, clocks, and biases), for example, provided from the International GNSS Service (IGS). The positioning process involves accurate observation models and sophisticated algorithms. In this way, this technique allows the calculation of a highly accurate, undifferenced, and absolute position.

Usually, a Kalman Filter is used to estimate the coordinates and additional parameters like the receiver clock error, wet tropospheric delay, and phase ambiguities. After a particular convergence time, a coordinate accuracy at the centimeter-level is achieved for the float solution. In the long term, even millimeter accuracy is possible. Furthermore, scientific research has found ways to fix undifferenced ambiguities in PPP. This reduces the convergence time considerably and is the key to the highest accuracy in PPP.

In comparison to well-established relative high precision GNSS positioning techniques methods (e.g., Real-Time Kinematik (RTK)), PPP reaches a similar position accuracy without nearby reference stations or networks. However, it has to be noted that precise satellite products are derived from global network data. The unknown user's coordinates and other attractive parameters (e.g., tropospheric delay) are estimated directly (figure 1.1). Since
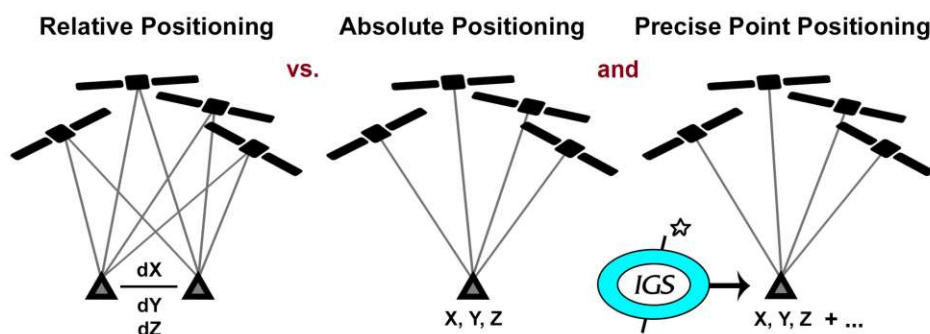
Figure 1.1: Schematic comparison of relative positioning, absolute positioning and PPP.

the used satellite orbits, clocks, and biases are globally valid, a worldwide homogeneous positioning quality is feasible. Furthermore, the same data has to be transmitted to every user without any restrictions or knowledge (e.g., approximate user position) and so data communication is required only in one direction. Therefore, PPP has advantages in terms of costs and computational efficiency.

On the other hand, PPP has a non-negligible coordinate convergence time. This is the primary concern of this technique. A typical convergence period of a conventional PPP solution using GPS observations is 20-30 minutes (Huber, 2015). After convergence, an accuracy similar to relative positioning methods is accomplished. Therefore, to make PPP more competitive against other (relative) high-precision GNSS positioning techniques, the convergence time reduction is a significant topic in scientific research and this thesis.

In general, PPP solutions have to be distinguished depending on their temporal availability. Real-time (RT) PPP requires satellite products available in real-time (e.g., real-time correction streams). On the other hand, PPP solutions in post-processing achieve the best results since they can use the highest quality satellite products available with a specific latency.

PPP is a very flexible technique that can handle multi-frequency observations of the highest-quality multi-frequency geodetic receivers as well as low-quality single-frequency observations of a smartphone. Of course, the choice of the satellite products and characteristics of the observations influence the quality and type of the PPP solution. In the context of this thesis, the focus lies on PPP solutions of the highest quality. Therefore, mainly post-processed solutions using observations from static geodetic receivers are presented.

1.2. Motivation and goal

PPP faces a promising future due to its properties and characteristics. The upcoming Galileo High-Accuracy Service (HAS) might give an additional boost to its popularity. In the future, PPP will be at least an equal alternative to the currently market-leading relative positioning methods and dense reference networks. It might even supersede these dominant relative positioning techniques at some point.

This thesis aims to show what is currently possible with PPP and the existing GNSS, frequencies, signals, and satellite products. Remember that unconsidered effects would jeopardize the PPP solution and destroy the integer property of the phase ambiguities. Therefore, a PPP software considering all relevant error sources and allowing integer ambiguity fixing has to be developed. Since the primary concern of PPP is the time until the position reaches the desired level of accuracy, various approaches and their effectiveness in reducing the convergence time and increasing the accuracy of PPP are examined. Furthermore, future topics in this regard are addressed. If instantaneous PPP convergence or a close to instantaneous convergence time is achieved, PPP is fully able to challenge the currently dominant relative positioning methods. Figure 1.2 presents an overview of the results achieved in this thesis in this regard.
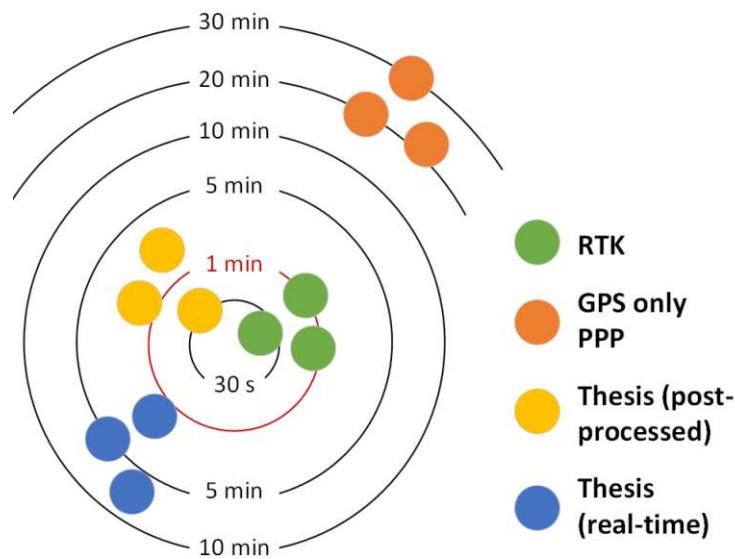
Figure 1.2: Typical convergence times to reach centimeter-level accuracy for RTK and different PPP methods

1.3. Outline

This thesis describes multi-GNSS and multi-frequency PPP approaches for static receivers. Furthermore, various methods for reducing the convergence time of PPP are introduced and examined. The described approaches, models, and algorithms are implemented in the software raPPPid developed in the course of this thesis. This flexible positioning software written in MATLAB[1] offers the user a Graphical User Interface (GUI) with various options to tune the PPP processing (e.g., thresholds, different models). Furthermore, the user can choose between various real-time and post-processed satellite products and atmosphere models. raPPPid was already used in multiple contributions and publications, most importantly Boisits et al. (2020) and Glaner and Weber (2021). It is planned to publish raPPPid as open-source software and the PPP component of the Vienna VLBI and satellite software (VieVS PPP) in the near future.

This thesis is organized as follows. After this introductory chapter, the second chapter deals with GNSS fundamentals. Chapter 3 describes different types of satellite products and examines error sources relevant to PPP. In the fourth chapter, the process of calculating a float PPP solution using a Kalman Filter and different PPP models is presented. The next chapter introduces ways of fixing undifferenced ambiguities considering the phase biases originating from the receiver and satellites. Based on the PPP results presented and studied in chapter 6, chapter 7 shows further potential and problems. Finally, chapter 8 discusses and summarizes the content of this thesis and provides a short outlook.

---

[1] MathWorks: *MATLAB Website*. https://www.mathworks.com/products/matlab.html

2. Fundamentals

2.1. Global Navigation Satellite Systems

The term Global Navigation Satellite System (GNSS) refers to a constellation of satellites and the associated infrastructure providing a worldwide positioning and navigation service independent of time, location, and weather. The main element to offer such a service and declare a GNSS fully operational is a certain number of satellites revolving around the Earth (figure 2.1). Typically, this number varies between 24 to 30 satellites and depends on the configuration of the orbits. GNSS satellites emit various signals on multiple frequencies in the L-band microwave range (Ultra-High-Frequency Band) summarized in the description of the RINEX format[2]. Everyone on the surface of the Earth or in near space can receive these signals. Subsequently, the user can calculate its position with proper models and algorithms.
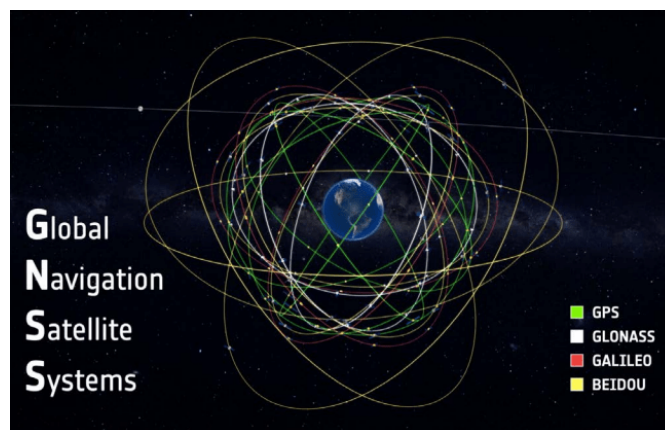
Figure 2.1: Illustration of the current GNSS constellations (Drotek, 2021)

In the 1960s, the first globally working GNSS, the US Navy Navigation Satellite System, better known as Transit, was established (Langley et al., 2017). Since that time, GNSS technology has developed rapidly. Nowadays, billions of users rely on their positioning service. GPS is the best-known and most persistent GNSS. It sets the benchmark for various GNSS from different countries and federations, which have emerged over time. Simultaneously, the overall number of GNSS satellites in space has increased massively. In present times, more than 100 GNSS satellites are in orbit, and further developments and improvements in the field of GNSS-based positioning can be expected. Examples are the use of optical Inter-Satellite Links and the addition of a small number of Low Earth Orbiting (LEO) satellites to consolidate the GNSS constellation ('Kepler system') (Günther, 2018). This would make terrestrial infrastructure mostly obsolete, and the resulting extremely precise satellite orbits, clocks, and biases would offer tremendous new possibilities, especially for PPP.

At the present day, we find four globally working GNSS: The US-American GPS, the Russian

---

[2] IGS: *The Receiver Independent Exchange Format*. https://www.igs.org/wg/rinex/#documents-formats

GLONASS, the European Galileo, and the Chinese BeiDou. Table 2.1 offers an overview of these four GNSS, and in the following, a short introduction is given. Their signals will be used for PPP in the further course of this thesis. For more details regarding GNSS in general, please refer to the literature of, for example, Hofmann-Wellenhof et al. (2008), Leick et al. (2015), and Teunissen and Montenbruck (2017).

2.1.1. GPS

The US Department of Defence operates the Global Positioning System (GPS), and its official name reads as follows: Navigational Satellite Timing and Ranging Global Positioning System (NAVSTAR GPS). The first launch of an experimental GPS satellite was on February 22, 1978, and in 1989, the first operational GPS satellite was launched. GPS reached Full Operational Capability (FOC) in summer 1995. Initially, GPS was designed to offer an accurate position, velocity, and time for military purposes only. However, during its development, civilian use was also established and is possible since the 1980s (Hofmann-Wellenhof et al., 2008). An essential step in this context was the deactivation of an intentional degradation (Selective Availability) of the GPS signals on May 2, 2000.

GPS uses Code Division Multiple Access (CDMA) to distinguish the signals of the satellites. Therefore, every signal consists of a modulated code on a carrier wave, which contains a pseudo-random code to identify the satellite and the so-called navigation message. Furthermore, the navigation message contains viable data for positioning, for example, parameters for computing the position of all satellites (Leick et al., 2015).

Initially, GPS satellites transmit signals on two frequencies (L1, L2). In the course of GPS modernization, which started in 2005 with launching the first IIR-M satellite, a new signal is transmitted for civilian users (L2C). Additionally, a third GPS frequency is established (L5) beginning with the launch of the first IIF satellite in May 2010. Since December 2018, all launched GPS satellites have been from block III/IIIF.

As a consequence, a growing number of satellites transmit signals on three frequencies (16 satellites in January 2021[3]). These three GPS frequencies are built using a fundamental frequency of $f_0 = 10.23$ Mhz, corresponding to a wavelength λ_0 of about 29.305 meters. To obtain the signal frequency f_i on the frequency i, the fundamental frequency is multiplied with the coefficients 154, 120 and, 115 for L1, L2, and L5, respectively.

$$f_i = k_i f_0 \tag{2.1}$$

Like most other GNSS satellites, GPS satellites circle around the Earth in Medium Earth Orbit (MEO). Usually, there are about 30 GPS satellites in space, although the FOC is already reached with 24 satellites. They are placed in six nearly circular orbits with an inclination of about 55°, an altitude of about 20 200 km above the Earth's surface, and a revolution period

---

[3] GPS: *New Civil Signals*. https://www.gps.gov/systems/gps/modernization/civilsignals/

GNSS	GPS	GLONASS	Galileo	BeiDou
Origin	USA	Russia	Europe	China
Operator	U.S. Space Force	Roscosmos	European Space Agency	China National Space Administration
First launch	February 22, 1978	October 12, 1982	December 28, 2005	October 30, 2000
Full operational capability	July 17, 1995	January 18, 1996	expected 2022	June 23, 2020
Nominal number of satellites	24	24	27	27, 5, 5
Orbit	MEO	MEO	MEO	MEO, IGSO, GEO
Orbit inclination	55	64.8°	56°	55°, 55°, 0°
Altitude	20 180 km	19 100 km	23 222 km	21 528 km, 35 786 km, 35 786 km
Revolution period	11h 57.96min	11h 15.73min	14h 4.75min	12h 53.4min, 1 day, 1 day
Ground track repeat period	~1 day	~8 days	~10 days	~7, 0, 0 days
Orbital planes	6	3	3	3, 3, 1
Plane separation	60°	120°	120°	120°
Ephemeris data	Kepler elements, correction coefficients	position, velocity, acceleration vectors	Kepler elements, correction coefficients	Kepler elements, correction coefficients
Coordinate frame	WGS-84	PZ-90	GTRF	CGCS 2000
Time system	GPS Time	GLONASS Time	Galileo System Time	BeiDou Time
Leap seconds	no	yes	no	no
Coding	CDMA	FDMA, CDMA	CDMA	CDMA
Frequencies [Mhz] and coefficients	L1: 1575.420 (154) L2: 1227.600 (120) L3: 1176.450 (115)	G1: 1602.000 G2: 1246.000 G3: 1204.704	E1: 1575.420 (154) E5a: 1176.450 (115) E5b: 1207.140 (118) E5: 1191.795 (116.5) E6: 1278.750 (125)	B1: 1561.098 (763) B2: 1207.140 (590) B3: 1268.520 (620)

Table 2.1: Overview of the system characteristics of GPS, GLONASS, Galileo, and BeiDou

of about 11 hours 58 minutes. This results in a ground track repeat period of one day. Due to this high resonance with the Earth's rotation, GPS satellites need orbit maneuvers every two years.

2.1.2. GLONASS

Globalnaja Nawigazionnaja Sputnikowaja Sistema (GLONASS) is the Russian (former Soviet Union) counterpart to GPS. Like GPS, GLONASS is a military system and operated by the Russian military forces. It has been developed simultaneously to GPS since the mid-1970s, and on October 12, 1982, the first GLONASS satellite was launched. In the mid of the 1990s, a fully operational constellation of 24 satellites was in orbit. But due to funding and financial problems, the number of satellites decreased dramatically, and only very few GLONASS satellites were in space at the beginning of the 21st century. With the Russian government's support, FOC was reached again by the end of 2011 (Revnivykh et al., 2017).

In general, GLONASS shows some specifics compared to other GNSS. The most important point is that GLONASS uses Frequency Division Multiple Acess (FDMA). Therefore, each satellite emits on a slightly different frequency used to identify the satellite. As FDMA is more challenging for receiver manufacturers (e.g., for low-cost receivers), this might be one reason why GPS became more dominant than GLONASS.

Originally, GLONASS satellites have transmitted signals within two frequency bands (G1, G2), and the frequency of a specific satellite is defined by its channel number l. This channel number is part of the GLONASS navigation message and with equations 2.2 and 2.3 the frequency on G1 f_{G1} and G2 f_{G2} is calculated.

$$f_{G1}(l) = 1602\,MHz + l \cdot 0.5625\,MHz \tag{2.2}$$

$$f_{G2}(l) = 1246\,MHz + l \cdot 0.437\,MHz \tag{2.3}$$

GLONASS satellites are divided into three generations: first-generation GLONASS I/II, second-generation GLONASS-M, and third generation GLONASS-K satellites. Since December 2005, all launched GLONASS satellites have been GLONASS-M and GLONASS-K1 satellites. GLONASS-K and the latest GLONASS-M satellites transmit a CDMA signal on a new frequency G3 (1202.25 Hz) in addition to the FDMA signals on G1 and G2. Currently (March 2020), a number of six three frequency GLONASS satellites is in space.

GLONASS satellites circle around the Earth in three orbital planes with an altitude of 19 100 km and a revolution period of 11 hours 15 minutes 44 seconds. Therefore, after eight days, a satellite passes the same point over Earth again. The GLONASS satellites are seperated by 120° in their orbital plane. The two antipodal GLONASS satellites in each orbital plane transmit on the same frequency because they are not visible for a terrestrial user at the same time. Compared to other GNSS satellites, GLONASS satellite orbits have a higher inclination (64.8°). This secures better visibility and improved geometry in higher latitudes

and improves the performance of GLONASS over Russian territory. In contrast to the other GNSS transmitting Kepler elements and correction coefficients (osculating orbital elements) in their broadcast message, the navigation message of GLONASS covers the satellite positions, velocities, and accelerations due to lunisolar attraction. Therefore, orbital integration is necessary to calculate the position of GLONASS satellites (Leick et al., 2015).

2.1.3. Galileo

Galileo is an European Union project and a joint initiative of the European Commission and the European Space Agency. It is the only entirely civilian GNSS, and its built-up started in the 2000s. Technical and administrative problems delayed Galileo's development several times. Especially, the number of satellites in space evolved slower than planned. The first In-Orbit Validation (IOV) satellites were launched on October 21, 2011, and two further followed on October 12, 2012. On August 22, 2014, the first two full-operational-capability satellites were launched, however into wrong orbits. These two satellites E14 and E18 have an abnormal eccentricity, and their semi-major axis deviates from the nominal values (Hadas et al., 2019). Nevertheless, both could be used regularly for positioning (Paziewski et al., 2018) until the begin of 2022. Since then, several sets of Galileo satellites have been launched, and FOC is currently expected in late 2022.

All Galileo satellites transmit signals on three frequencies using CDMA. However, the frequency of E5 is separated into an E5a and an E5b component, which can be tracked together or separately. The Galileo system offers four levels of service (Open, High Accuracy, Public Regulated, and Search and Rescue Service[4]). To build the signal frequencies E1, E5a, E5b, E5, and E6, the coefficients 154, 115, 118, 116.5, and 125 are used in conjunction with the same fundamental frequency like for GPS ($f_0 = 10.23$ Mhz and equation 2.1).

The most probable complete constellation envisages 30 satellites in space. The 24 primary and 6 spare satellites (two in each orbital plane) will revolve the Earth in about 14 hours 4 minutes 42 seconds, resulting in a ground track repeat period of 10 days or 17 orbits. The orbits are nearly circular with an altitude of about 23 260 km and an inclination of about 56°.

The Galileo constellation results from detailed studies and optimization using the experience of decades of GNSS. Research has shown that the Galileo constellation performs better than the GPS constellation in different aspects (Hadas et al., 2019). Montenbruck et al. (2018) showed that the Galileo broadcast ephemeris's accuracy is about three times better than that of GPS and provide a representative RMS value of 20 cm for the signal-in-space range error (SISRE). Furthermore, Galileo will offer a High Accuracy Service (HAS), which is specifically designed for the PPP technique and will further enhance the interoperability with other GNSS (chapter 3.1.3).

---

[4] European Union Agency for the Space Programme: https://www.euspa.europa.eu/galileo/services

2.1.4. BeiDou

The name BeiDou is Chinese for the Big Dipper asterism (in German 'Großer Wagen'). The current GNSS BeiDou-3 is the third generation of BeiDou and a further development of the regional BeiDou-2 or COMPASS system. Due to a rapid expansion and growth of this system, considerably more BeiDou than Galileo satellites are in space despite simultaneous development, and FOC has been reached in 2020. BeiDou offers two service levels: an open service and an authorized service primarily for the Chinese government and military. BeiDou satellites emit signals on three frequencies B1, B2, and B3. The signal frequencies are generated using a fundamental frequency of 2.046 MHz and the coefficients 763, 590, and 620, respectively (equation 2.1).

In contrast to other present GNSS constellations and due to its evolution, the BeiDou constellation consists of different satellite types. The BeiDou MEO satellites circle around the Earth in three orbital planes with an inclination of 55°, an altitude of 21 528 km, and a revolution period of 12 hours 53 minutes 24 seconds. This results in a ground track repeat period of 7 days. In addition to the nominal number of 27 MEO satellites, the constellation consists of five geostationary (GEO) satellites and five satellites with inclined geosynchronous orbit (IGSO). GEO satellites have a circular orbit with an inclination of 0° and a revolution period equal to the Earth rotation. Therefore, for an observer fixed on the Earth's surface, they seem stationary over the Earth equator (e.g., satellite television). Compared to GEO satellites, IGSO satellites are inclined to the equatorial plane, and their ground track in the ECEF is similar to an eight. The GEO and IGSO satellites of BeiDou cover a longitude belt from 50°E to 170°E (East Asia and Australia). Note that table 2.1 lists the characteristics of all BeiDou satellite types.

2.2. Positioning with GNSS

To determine his position, a GNSS user needs a receiver recording the signals emitted from GNSS satellites. The essential observation is the distance between the satellite and receiver. Since it is not possible to directly measure this distance, the signals' run time is measured and multiplied with the speed of light. The user's position is then estimated either in real-time or post-processing and either internally in the receiver directly or externally. Two major positioning approaches can be identified: absolute and relative positioning.

2.2.1. Absolute positioning

The concept of absolute positioning is the most straight-forward approach of GNSS-based positioning utilizing information on satellite orbits, clocks, and biases. In the simplest case, the navigation message data is applied in a so-called Single Point Positioning (SPP) achieving an accuracy of a few to tens of meters. Typical examples are positioning of low-cost receivers, smartphones, or GPS watches. Using the distances to the satellites, the coordinates of the
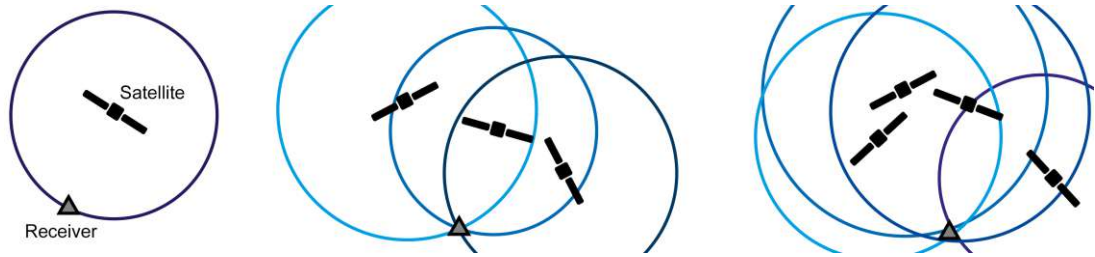
Figure 2.2: Two-dimensional sketches of absolute positioning with GNSS in theory (left and middle) and in reality (right)

receiver as well as a receiver clock bias are directly estimated. The following equation 2.4 serves as a starting point for SPP describing the distance ρ_R^S between the satellite S and the receiver R.

$$\rho_R^S = \sqrt{(X^S - x_R)^2 + (Y^S - y_R)^2 + (Z^S - z_R)^2} + c\,dt_R \tag{2.4}$$

where satellites' coordinates are denoted as X^S, Y^S, Z^S and the receiver's coordinates as x_R, y_R, z_R. In three-dimensional space a constant distance from a point corresponds to a sphere (left graphic of figure 2.2). Therefore, the geometrical interpretation of absolute positioning is the section of spheres. In theory, three range measurements or spheres are sufficient to get a unique intersection (middle graphic of figure 2.2).

Unfortunately, a tiny missynchronisation between the satellite and receiver clock leads to a massive distance error since GNSS signals travel with the speed of light c. Consequently, it is necessary to estimate a receiver clock error dt_R, and ranges to at least four satellites are needed for a GNSS-based positioning.

Furthermore, due to noise and different error sources, the spheres will not intersect at a single point. The position has to be estimated (right graphic of figure 2.2) using a suitable adjustment (e.g., Least Squares Adjustment). Fundamentally, a higher number of satellites improves the geometry and, subsequently, the parameter estimation and position's accuracy. Furthermore, many more error sources affect the measurements, leading to an improved measurement model and the GNSS observation equations presented in chapter 2.3.
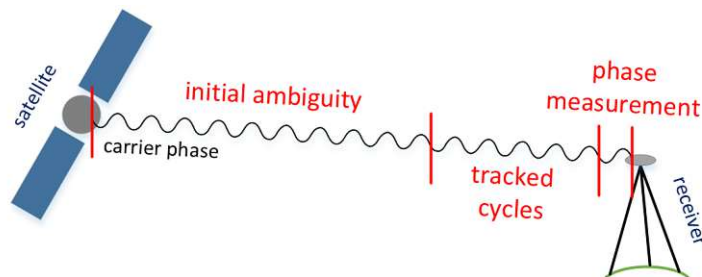
Figure 2.3: GNSS phase measurement

Contrary to SPP, PPP achieves centimeter or even millimeter accuracy in an absolute po-

sitioning process by applying very upscale satellite products and sophisticated observation models. To achieve such an accuracy level, many error sources are considered in PPP (chapter 3.2). Additionally, the precision of the so-called phase observation is exploited in a Kalman Filter (section 4.4). The phase observation is the difference between the carrier's received phase and a reference carrier generated by the receiver (figure 2.3). Unfortunately, the receiver measures only the fractional phase within one full cycle, and tracks the number of elapsed full cycles. The ambiguity, an arbitrary integer number of full wavelengths, is unknown and, usually, estimated.

2.2.2. Relative Positioning

In relative positioning, the receiver's unknown coordinates are estimated relative to a known reference point (figure 2.4). Instead of calculating the unknown coordinates directly, the vector $\boldsymbol{b}_{AB}$, also known as baseline, between the known reference point and the unknown location is determined. Through adding this vector to the known coordinates of the reference point, the unknown receiver coordinates $\boldsymbol{x}_B = \boldsymbol{x}_A + \boldsymbol{b}_{AB}$ are obtained.
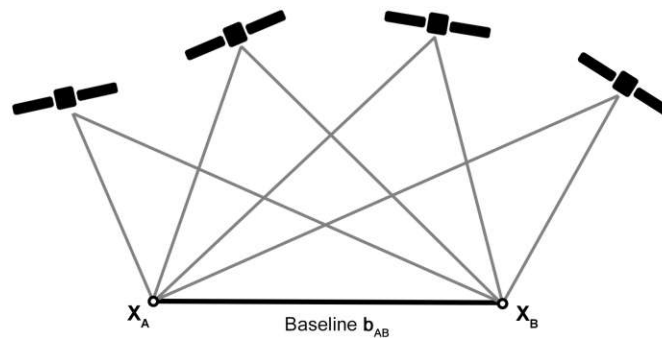
Figure 2.4: Basic concept of relative positioning with GNSS, based on (Hofmann-Wellenhof et al., 2008)

Relative position methods rely on nearby reference stations with well-known coordinates. They exploit the fact that GNSS error sources are spatially and timely correlated or, in other words, that the same error sources affect the GNSS measurements of a nearby placed receiver with similar strength. Therefore, single- and double-differences between two or more receivers are formed to reduce or eliminate error sources (Langley et al., 2017). An increasing spatial distance between A and B decreases the correlation of the error sources. Consequently, the positional accuracy of relative positioning methods depends on the length of the baseline.

The most prominent and popular relative positioning method is Real-Time Kinematic (RTK). Currently, it is extensively used in highly demanding GNSS positioning, for example, geodetic surveying. By using double-differences it is possible to fix the phase ambiguities (section 2.3) to their correct integer values, which is the primary key to obtain the highest accuracy in GNSS based positioning. In RTK mode, it typically takes a few seconds to a few min-

utes to achieve this. After that period, RTK reaches a horizontal coordinate accuracy at the centimeter-level or slightly below, and typically the height component is about a factor 1.5 to 2 worse (Hofmann-Wellenhof et al., 2008). These values can be seen as a benchmark for PPP.

Note that in contrast to PPP, RTK requires data communication in two directions. Furthermore, it is limited to a baseline length of about 50 km requiring a dense station network providing corrections. Examples of such services in Austria are Echtzeit-Positionierung-Austria (EPOSA) and Austrian Positioning Service (APOS). For more detailed information on RTK, the interested reader is referred to Odijk and Wanninger (2017), Seeber (2003), and the huge variety of available literature on this topic.

2.3. GNSS observation equations

Typically, GNSS receivers measure the distance to each satellite in two ways: code and phase measurement. Because satellite navigation uses the 'one-way concept' involving two clocks, these ranges are biased by the satellite clock error and the receiver clock error (Hofmann-Wellenhof et al., 2008). Furthermore, various error sources and biases affect these measurements, and consequently, they are denoted as pseudoranges.

The receiver determines the time difference between the signal's emission and its reception by a correlation procedure. By multiplying this time difference with the speed of light, the code observable is obtained. Additionally, the receiver measures the difference between the received phase carrier and a generated reference carrier (figure 2.3). By multiplication with the carrier's wavelength, this phase difference is converted from the unit of cycles to meters. The resulting phase observation is about 100 times more precise than the code observation. In addition, the significant discrepancy between code and phase observation is the ambiguity term of the phase observable. To fully exploit the precision of the phase measurement in the positioning process, the main challenge is to derive the ambiguity and to determine the integer number of full wavelengths in a certain way.

Index	GNSS	Acronym	1	2	3	4	5
1	GPS	G, GPS	L1	L2	L5	-	-
2	GLONASS	R, GLO	G1	G2	G3	-	-
3	Galileo	E, GAL	E1	E5a	E5b	E5	E6
4	BeiDou	C, BDS	B1	B2	B3	-	-

Table 2.2: The order of GNSS, frequencies, indices, and acronyms

The GNSS observation equations describe these two different types of observations. In this thesis, these equations are used for all GNSS in the same way, and to improve the readability no index for the GNSS is included. However, a certain order and indexing is used for the processed GNSS and frequencies presented in table 2.2 together with the used GNSS acronyms.

The GNSS observation equations represent reality in mathematical terms by including the most common error sources. They serve as a starting point to build an observation model for the positioning process. Consequentially, they are used to develop PPP models in chapter 4. Furthermore, chapter 3.2 will introduce additional error sources that have to be considered for PPP. The GNSS observation equations between a satellite S and a receiver R can be written for the code and phase observation in units of meters as the following (Hauschild, 2017):

$$P_i = \rho + c(dt_R - dt^S) + dTrop + dIon_i + B_{R,i} - B_i^S + \varepsilon \tag{2.5}$$

$$L_i = \rho + c(dt_R - dt^S) + dTrop - dIon_i + \lambda_i(N + b_{R,i} - b_i^S) + \varepsilon \tag{2.6}$$

with the code observable P_i and the phase observable L_i on frequency i. ρ denotes the geometric distance (equation 2.4) between satellite and receiver, where ^{S} and $_R$ are omitted for reasons of legibility. The geometric distance ρ contains implicitly the satellite and receiver position. ε comprises random and other (negligible) errors.

The receiver clock error dt_R and satellite clock error dt^S are the difference between the GNSS time system and the receiver and satellite clock, respectively. They are both multiplied by the speed of light c to convert them to meters.

The effects of the atmosphere on GNSS signals are divided into a tropospheric delay $dTrop$ and an ionospheric delay $dIon_i$ (sections 3.2.3 and 3.2.2, respectively). The ionospheric delay appears in the GNSS observation equation for code observations as well as phase observations, but with opposite sign. Therefore, the code is delayed through the signal's passage through the ionosphere while the phase is advanced (section 3.2.2).

Different biases occur in the GNSS observation equations. In the code observation's case, B_R and B^S denote the receiver and satellite's code hardware delays converted to range. The phase observation contains phase biases originating from hardware delays of the receiver b_R and the satellite b^S. They are lumped together with the integer term N describing the number of full wavelengths between satellite and receiver. These three terms are multiplied with the wavelength λ_i to obtain the unit of meters.

Apart from code and phase measurements, GNSS receivers usually provide the signal strength as a separate observation and they also record the Doppler shift. This shift of the signal frequency of the signal originates from the relative movement between satellite and receiver. It is especially useful for kinematic PPP or for cycle slip detection. The observation equation for the Doppler shift D on the frequency i reads:

$$D_i = \left(\frac{\boldsymbol{p}_R - \boldsymbol{p}^S}{||\boldsymbol{p}_R - \boldsymbol{p}^S||} \bullet (\boldsymbol{v}_R - \boldsymbol{v}^S) \right) \frac{1}{\lambda_i} \tag{2.7}$$

where $\boldsymbol{p}$ denotes the position and $\boldsymbol{v}$ the velocity vector of the receiver R and satellite S in an Earth-Centered Earth-fixed coordinate system (section 2.5.1), respectively. The symbol $\bullet$ describes the dot product, and λ_i is the signal's wavelength on the frequency i.

2.4. Linear combinations

The idea behind building a linear combination (LC) of the original observations is to create a combination with desirable properties. Since LCs are formed using code and phase observations of a single receiver, they are a viable option for PPP. LCs are built to reduce, eliminate, measure, or isolate specific error sources or to create an observation with a preferable wavelength (Hauschild, 2017). Examples are the elimination of the first-order ionospheric delay or LCs with a large wavelength to ease ambiguity fixing. Other advantages and reasons for the formation of LCs are the reduction of computational cost or data size. In any case, code and phase measurements are combined with proper coefficients using the GNSS observation equations 2.5 and 2.6 as a starting point.

$$L_{LC} = a_1 L_1 + a_2 L_2 + a_3 L_3 \tag{2.8}$$

The equation 2.8 shows the general form of a LC for phase observations and three frequencies in the unit of meters, where a_1, a_2, and a_3 are the coefficients of the LC (Glaner, 2017). Of course, the concept of LCs is also applied to code observations and can be extended to any number of frequencies. However, the most common LCs are built from two frequencies. Furthermore, the combination of code and phase measurements in a single LC is possible. Theoretically, it would also be possible to build a LC with the observations of different GNSS, but this seems practically impossible due to different biases, clock errors, and clock definitions. In the following, some characteristics and specifics of LCs are introduced.

$$\sigma_{LC}^2 = a_1 \sigma_{L_1}^2 + a_2 \sigma_{L_2}^2 + a_3 \sigma_{L_3}^2 \tag{2.9}$$

$$\tilde{n} = \sqrt{a_1^2 + a_2^2 + a_3^2} \tag{2.10}$$

The noise of the raw observations is increased during the creation of a LC (Richert and El-Sheimy, 2006), and the resulting LC's noise is calculated with equation 2.9 using the coefficients of the LC a_i and the observation noise of the raw observations σ_{L_i}. Under the assumption that the noise of the original observations is equal and uncorrelated, a noise amplification factor $\tilde{n}$ can be defined (equation 2.10). This parameter describes the increase of the observation noise through the LC (Cocard et al., 2008).

$$\alpha_i = a_i \frac{\lambda_i}{\lambda_{LC}} = a_i \frac{f_{LC}}{f_i} \tag{2.11}$$

$$f_{LC} = \alpha_1 f_1 + \alpha_2 f_2 + \alpha_3 f_3 \tag{2.12}$$

$$\lambda_{LC} = \frac{c}{f_{LC}} \tag{2.13}$$

Combining two or more carrier phase observations leads to a LC with a different frequency and wavelength. To calculate the frequency of a LC, the integer-phase coefficients α_1, α_2,

and α_3 (equation 2.11) are introduced (Hauschild, 2017) and are plugged in equation 2.12. Afterward, the wavelength of the LC is easily computed with the speed of light c and equation 2.13. Alternatively, Hauschild (2017) provides formulas for the frequencies and wavelengths of the most common LCs.

$$L = \alpha_1 k_1 + \alpha_2 k_2 + \alpha_3 k_3 \tag{2.14}$$

$$f_{LC} = f_0 L \tag{2.15}$$

$$\lambda_{LC} = \frac{\lambda_0}{L} \tag{2.16}$$

Following Cocard et al. (2008), the so-called Lane Number L defined in equation 2.14 is useful in this context. It is valid for all GNSS, which build their signal frequencies based on a fundamental frequency f_0 and coefficients k_i (equation 2.1). The frequency and wavelength of a LC can be expressed as a function of the Lane number (equations 2.15 and 2.16). λ_0 denotes the wavelength associated with the fundamental frequency (e.g., 29.305 m for GPS and Galileo).

$$\gamma_{ij} = \left(\frac{f_i}{f_j}\right)^2 \tag{2.17}$$

$$q_{LC} = a_1 \gamma_{11} + a_2 \gamma_{12} + a_3 \gamma_{13} \tag{2.18}$$

The factor γ_{ij} describes the ratio of the squared frequencies i and j and will be useful in various formulas. At this point, it is helpful for the description of the ionospheric amplification factor presented in equation 2.18. It describes the LC's increase or decrease of the ionospheric delay in relation to the ionospheric delay on the first frequency of this GNSS. For example, if a Galileo LC has an ionospheric amplification factor of 2, the ionospheric delay of the LC is twice as big as the ionospheric delay on the E1 frequency.

In general, a small ionospheric amplification factor is desirable as this indicates a small influence of the ionospheric delay. Furthermore, LCs with a small noise amplification factor and large wavelength are preferable. Unfortunately it is not possible for a LC to fulfill all demands at once. Therefore, systematic searches for optimal LCs using two or three fundamental frequencies have been performed resulting in interesting geometric structures and interpretations (Richert and El-Sheimy, 2006; Cocard et al., 2008; Urquhart, 2008; Glaner, 2017). In the following, the most important types of LCs will be introduced.

2.4.1. Ionosphere-free LC

The ionosphere is a dispersive medium for microwave signals and GNSS measurements (section 3.2.2). The size of the ionospheric delay depends on the frequency of the signal, which is why the subscript i occurs in the ionospheric delay $dIon$ in the GNSS observation equations (section 2.3). It is possible to exploit this fact and build the so-called ionosphere-free

linear combination (IF LC) using observations on two frequencies ($n < m$) and the following equations 2.19 and 2.20 for code and phase observations, respectively.

$$P_{IF} = \frac{f_m^2 P_m - f_n^2 P_n}{f_m^2 - f_n^2} \tag{2.19}$$

$$L_{IF} = \frac{f_n^2 L_n - f_m^2 L_m}{f_n^2 - f_m^2} \tag{2.20}$$

The IF LC eliminates the first-order ionospheric delay and, therefore, its ionospheric amplification factor is equal to zero. The remaining higher-order terms of the ionospheric delay account for approximately 0.1% of the total delay and can be neglected in most cases. The IF LC is widely used in PPP, and its use will be discussed in the further course of this dissertation (chapter 4). Note, that it is also possible to find IF LCs for three frequencies (Cocard et al., 2008; Glaner, 2017).

2.4.2. Wide-Lane LCs

A LC, which has a longer wavelength than the largest individual wavelength of its combination, belongs to the group of Wide-Lane (WL) LCs. They are especially interesting for integer ambiguity resolution since a long wavelength facilitates the fixing process and reduces the search space. Therefore, a large wavelength is desirable for a LC even if no error sources are reduced or eliminated. Taking the coefficients of the fundamental frequency k_i (table 2.1), the Lane Number, and equation 2.16 into consideration, the inequality in equation 2.21 is true for a WL LC. It gets clear that only a finite number of WL LCs exists under the condition of keeping the integer property of the phase ambiguity (Glaner, 2017).

$$0 < |L_{WL}| < min(k_i) \tag{2.21}$$

$$L_{WL} = \frac{f_i}{f_i - f_j} L_i - \frac{f_j}{f_i - f_j} L_j \tag{2.22}$$

The most common WL LCs use dual-frequency observations, and their formation is presented in equation 2.22 in the unit of meters. In former times, GPS was the only operational GNSS and emitted signals on two frequencies. Therefore, the WL LC using L1 and L2 observations is simply called WL LC until today. It has a wavelength of about 0.86 meters. Due to GPS modernization, new possibilities for the described type of WL LC have opened up, introducing the following denotations. The Extra-Wide-Lane (EW) LC is formed using the L2 and L5 frequency and has the biggest wavelength of about 5.86 m. The term Medium-Lane (ML) LC describes the WL LC with the smallest wavelength of about 0.751 meters built from the L1 and L5 frequency. These expressions can be used in a similar way for the WL LCs of other GNSS, and Hauschild (2017) provides an overview of their wavelengths.

2.4.3. Narrow-Lane LCs

Conversely to the last chapter, a LC is called Narrow-Lane (NL) LC, when it has a smaller wavelength than the shortest individual wavelength of the specific GNSS. For example, the NL LC built from GPS L1 and L2 has a wavelength of 10.7 cm. Generally, NL LCs are characterized by a low noise, which should mirror in a higher position accuracy in the optimal case. But in fact, NL LCs show no real advantage, their short wavelength makes ambiguity resolution more complicated, and the therm NL LC is mainly useful for characterizing LCs (Glaner, 2017). Note that most IF LCs are NL LCs.

$$|L_{NL}| > max(k_i) \tag{2.23}$$

$$L_{WL} = \frac{f_i}{f_i + f_j} L_i + \frac{f_j}{f_i + f_j} L_j \tag{2.24}$$

Again the Lane Number can be used in conjunction with the inequality presented in equation 2.23 to identify NL LCs. From this inequality, it gets clear that an infinite number of NL LCs exist. The type of NL LC, which occurs most in practice, is built from two frequencies in the unit of meters with equation 2.24. The fact that GNSS broadcast on more than two frequencies nowadays results in different possibilities for creating such a NL LC (similar to the EW, WL, and ML LC).

2.4.4. Geometry-free LC

The Geometry-free linear combination (GF LC) eliminates all geometric or non-dispersive parts of the GNSS observation equations: the geometric distance, tropospheric delay, satellite orbit error, satellite clock error, and receiver clock error. Consequently, only the ionospheric delay, integer ambiguity, and hardware delays of the satellite and receiver remain in the combined observation. Therefore, this LC is useful to estimate the ionospheric delay when taking receiver code biases (section 3.2.11) into consideration (Magnet, 2019). Furthermore, the GF LC can be used to detect cycle slips (chapter 3.2.7) or to determine frequency-dependent antenna variations. An interesting characteristic of GF LCs is that their frequency is zero, and their wavelength is infinite (Glaner, 2017). In its simplest way, a GF LC is built using observations on two frequencies ($n < m$) for code and phase measurements in the following way.

$$P_{GF} = P_n - P_m \tag{2.25}$$

$$L_{GF} = L_m - L_n \tag{2.26}$$

2.4.5. Hatch-Melbourne-Wübbena LC

First proposed by Hatch (1982), the Hatch-Melbourne-Wübbena (HMW) LC is a combination of code and phase measurements on two frequencies ($n < m$). It is formed in units of meters

with the following equation.

$$HMW = \frac{f_n L_n - f_m L_m}{f_n - f_m} - \frac{f_n P_n + f_m P_m}{f_n + f_m} \tag{2.27}$$

The HMW LC eliminates the first-order ionospheric delay, clock errors, and all geometric error sources. Only the ambiguity remains in the combination and, therefore, the HMW LC is suitable for cycle slip detection or ambiguity fixing. It can be described as a GF and IF LC of code and phase measurements (Glaner, 2017). Therefore, it is mainly affected by the noise of the used code measurements. Depending on the used frequencies in equation 2.27, the ambiguity of the HMW LC corresponds to the ambiguity of the WL, EW, or ML LC. Based on this fact, the HMW can be used for ambiguity fixing in PPP (chapter 5).

2.4.6. Multipath LC

Multipath (MP, section 3.2.6) is one of the major error sources in GNSS-based positioning and can lead to gross errors in the estimation of the user position. The detection of multipath is a challenging task, and LCs have been developed for this purpose, potentially useful for PPP (section 7.4). Note that phase multipath is usually small, and its effect is smaller than a quarter of the signal's wavelength.

$$MP_i = P_i - L_i + \frac{2}{1 - \gamma_{12}}(l_i - L_j) \tag{2.28}$$

$$MP_3 = \left(\lambda_3^2 - \lambda_2^2\right)P_1 + \left(\lambda_1^2 - \lambda_3^2\right)P_2 + \left(\lambda_2^2 - \lambda_1^2\right)P_3 \tag{2.29}$$

Equation 2.28 presents the most frequently used MP LC for detecting multipath in the code observation on the frequency i using dual-frequency phase observations on the frequencies i and j (Leick et al., 2015, section 6.1.1.6). The ratio γ_{12} is given in equation 2.17. Besides multipath, this GF and IF LC contains various phenomena, like signal biases, group delay variations, ambiguities,... Under the assumption that all these contributing terms are constant over time, this LC allows evaluating the temporal variation of multipath after subtracting a constant part. Similarly, the LC in equation 2.29 can be used to detect multipath in triple frequency observations. Hauschild (2017) presents details and investigations on these two MP LCs.

2.5. Reference systems

Position and navigation applications require proper spatial and temporal reference systems to describe various effects, error sources, and observations. Due to diverse requirements and demands, several types of reference systems are in use, and various coordinate and time systems have to be considered during PPP processing.

2.5.1. Coordinate systems

Typically, Cartesian coordinate systems are defined by the system's origin, three axes directions, and a scale factor. Usually, coordinate systems utilized in GNSS positioning are located in the Earth's center of mass. They are distinguished into space-fixed (celestial) and earth-fixed (terrestrial) systems. Moreover, coordinate systems for the descriptions of the various receiver- and satellite-specific errors are needed. In the following, these different coordinate systems relevant for PPP are described shortly. For the transformation of position vectors between systems, the 3D similarity transformation is frequently used. The interested user is referred to the literature, for example, Hofmann-Wellenhof et al. (2008) or Leick et al. (2015).
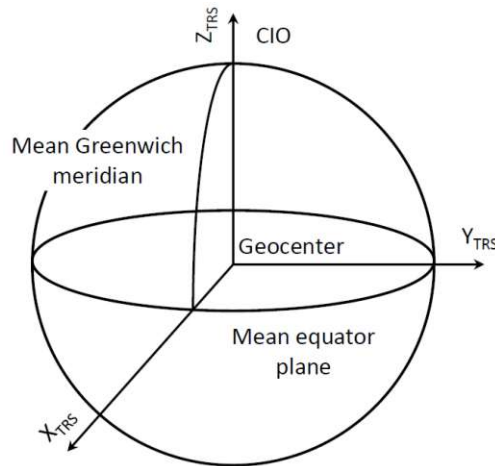
Figure 2.5: Earth-Centered Earth-Fixed coordinate system (Hinterberger, 2016)

Terrestrial reference system To describe positions on the Earth's surface or provide precise satellite orbits, it is practical to use a coordinate system considering the Earth's rotation around its axis. Therefore, Terrestrial Reference Systems (TRS), also known as Earth-Centered Earth-Fixed (ECEF), are chosen. The origin of such a system is located in the center of mass of the Earth. The Z-axis points towards the definition of a mean position of the Earth's rotation axis, the Conventional International Origin (CIO). By convention, the CIO is the average pole position from 1900 to 1905. The X-axis is pointing to Greenwich's

meridian, or more specifically, to the intersection point of the Greenwich meridian with the equatorial plane. Finally, the Y-axis completes a right-handed system (figure 2.5).

A realization of such a TRS is the International Reference Frame (ITRF), provided by the International Earth Rotation and Reference Systems Service (IERS). The ITRF is defined by a huge number of precise positions of globally distributed monitoring stations using space-geodetic techniques, like VLBI, SLR, and GNSS. In the ITRF, temporal effects are taken into account, for example, plate tectonics. The latest active realization is denoted as ITRF 2014 referring to the reference epoch 2010.0. The ITRF 2020 is currently under construction and planned to be issued in 2022. Further examples for terrestrial reference frames are the different GNSS broadcast frames (e.g., WGS84) presented in table 2.1.

Local-level system A local-level coordinate system is advantageous for the description of particular receiver specific corrections. For example, it is practical to measure the antenna height with respect to such a coordinate system (section 3.2.8). A local-level coordinate system is a topocentric system attached to the position of a GNSS receiver. The coordinate axes are defined in the following way: The z-axis is pointing to the vertical direction, the x-axis towards the north, and the y-axis to the east, completing a left-handed Cartesian coordinate system. This coordinate system is often referred to as ENU (east, north, up) system and visualized in figure 2.6.
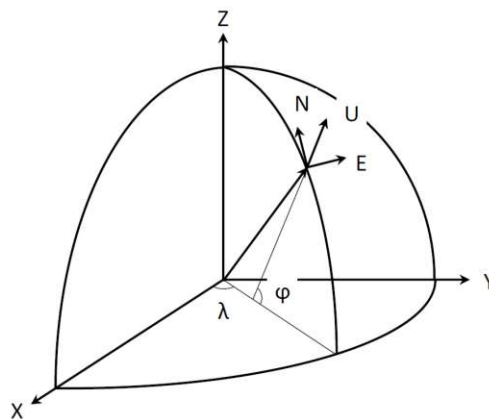
Figure 2.6: Global and local-level coordinate system (Hinterberger, 2016)

Satellite-fixed coordinate system A satellite-fixed coordinate system is useful for orbit determination and perturbation calculations. It is attached to the satellite body. Typically, the origin is placed in the satellite's center of mass (COM) S_{COM}. One option applied by the State Space Representation (SSR, section 3.1.3) is to define the axes according to the following scheme (left part of figure 2.7): The x-axis coincides with the radius vector (radial component), and the y-axis points into the direction of motion (along-track component).

Finally, the z-axis is orthogonal to the x-axis and y-axis and completes the right-handed co-ordinate system (cross-track or out-of-plane component). The presented definition is helpful to describe the satellite orbit's deviation from a reference orbit. For this reason, it is used in the standardized RTCM (Radio Technical Commission for Maritime Services) messages for the transmission of orbit corrections to the broadcast navigation message (section 3.1.3).
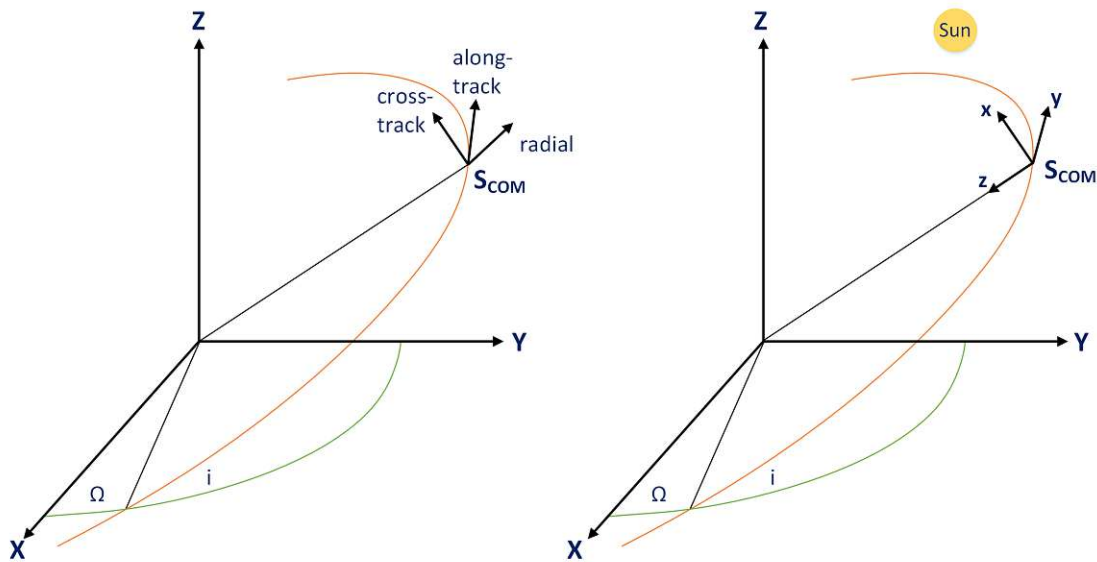
Figure 2.7: Satellite-fixed coordinate systems for describing deviations from a reference orbit (left) and the satellite's attitude (right)

Another type of a satellite-fixed coordinate system is used to describe the attitude of the GNSS satellite (right part of figure 2.7, section 3.1.4). The origin is again in the center of mass of the satellite. The z-axis coincides with the radial component but in direction to the Earth. The y-axis lays in the plane perpendicular to the Sun, and the x-axis completes a right-handed Cartesian coordinate system (Rebischung and Schmid, 2016).

2.5.2. Time systems

Various time systems applying diverse processes to measure and realize the concept of time are in use. Figure 2.8 shows an overview of the time systems relevant for PPP. Besides time systems, which are based on the Earth's rotation (solar and sidereal times) or atomic oscilla-tors (atomic times), dynamic time systems exist. For more details regarding these and time systems at all, the interested reader is referred to (Hofmann-Wellenhof et al., 2008, chapter 2.3) and Jekeli and Montenbruck (2017).

Common time systems The most obvious approach is to measure time based on the Sun's position or, more specifically, with Earth's rotation. Because the Earth rotation is not a uniform process (e.g., it slows down over time), the resulting time systems are not uniform.
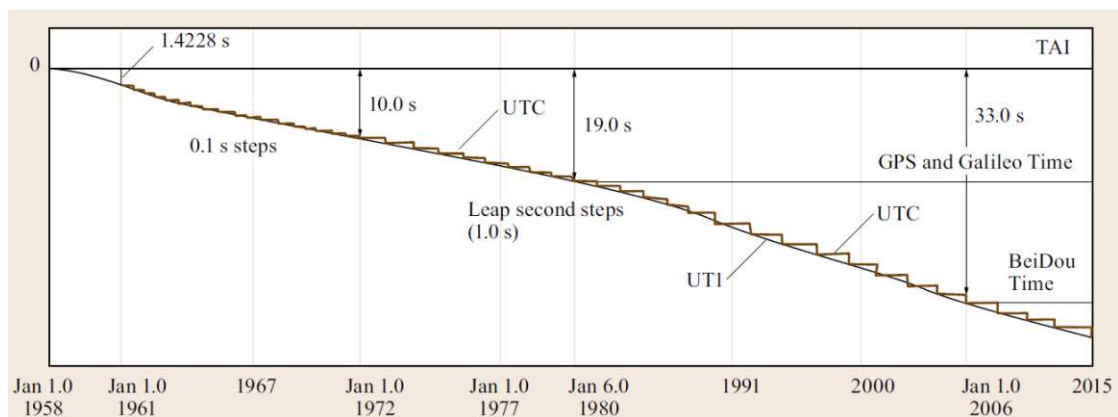
Figure 2.8: Relationships between different time systems (Jekeli and Montenbruck, 2017, Fig.2.4, slightly modified)

A measure of Earth's rotation is the angle between the meridian of a celestial reference (e.g., the vernal equinox) and an earth-fixed reference meridian (usually the Greenwich meridian). Universal Time (UT) is defined as the Greenwich hour angle of a fictive Sun uniformly orbiting in the equatorial plane augmented by 12 hours. If the UT is corrected for polar motion, UT1 is obtained.

In contrast, atomic time scales are uniform time systems. They are defined and realized by atomic oscillators. The International Atomic Time (TAI) is maintained by a set of globally distributed atomic clocks regulated by the International Bureau of Weights and Measures. One second of TAI is identical to one SI second. The epoch of TAI corresponds to the epoch of UT1 on 1 January, 1958 by definition. For some applications, a uniform time system based on atomic clocks and close to UT1 is needed. This leads to UTC (coordinated Universal Time), the main international accepted time standard. The local time used in our day-to-day life is nothing different than UTC shifted by the respective time zone. To guarantee that the difference between UTC and UT1 is always smaller than 1 second, integer leap seconds are introduced every few years. In other words, UTC is a compromise between TAI and UT1. Currently (February 2022) and since the last leap second in 2016, TAI is 37 seconds ahead of UTC.

GNSS system times GNSS-based positioning has high demands on time standards. Therefore, each GNSS maintains its own system time, and its characteristics have to be considered carefully in the positioning process. The system times of GPS, GLONASS, Galileo, and BeiDou are atomic time scales based on the SI second, but they have different offsets to TAI. When observations from multiple GNSS are recorded, they are normally referred to GPS Time (GPST).

The origin of GPST corresponds to UTC at January 6.0, 1980, and, therefore, it has a constant integer second offset of 19 seconds to TAI. However, GPST is not adjusted by leap

seconds to slow down with UT, and currently (February 2022), the integer part of the offset between GPST and UTC is 18 seconds. The Galileo System Time (GST) definitions and BeiDou Time (BDT) are pretty similar to GPST. For consistency, the origin of GST is identical to GPST. January 1.0, 2006, UTC has been chosen as the origin for BDT. Therefore, the offset from GST to TAI equals 19 and from BDT to TAI 33 integer seconds.

Contrary to the other GNSS time systems, GLONASS Time (GLST) is aligned to UTC and not continuous. For its origin, January 1.0, 1996, respecting the UTC time system of the Soviet Union, has been chosen. Besides introducing leap seconds, GLST is always three hours ahead of UTC because of Greenwich and Moscow's time zone difference.

Dates   Historically, the GPS week and day of week are frequently used for labeling GNSS-related data files. The GPS date counts the number of weeks since the beginning of GPST as a continuous number. Currently (end of February 2022), we are in GPS week 2199. A GPS week starts on Sunday at 0:00h GPST. From this point in time, the time is counted in seconds of week and days of week from 0 to 6. For example, Wednesday is always day 3 in a GPS week. Nowadays, new formats tendentiously rely on the year and the day of the year (doy). Note that Galileo and BeiDou use a similar definition for their date (weeks and seconds of week) despite different origins. The Julian Date (JD) is typically used as an intermediate step for the conversion between different dates.

3. Observation Model

Since PPP is an absolute positioning method, the quality of the solution and estimated parameters depends on the quality of the used satellite products (orbits, clocks, biases) and the modeling of the error sources. Therefore, high-precision satellite products are the essential foundation for PPP. Furthermore, already in a simple SPP with low-cost devices like smartphones or GPS watches reaching an accuracy level of around ten meters, many corrections and error sources have to be considered. Obviously, the number and complexity of error sources increase for PPP.

The following chapter describes the use of various satellite products for PPP. Furthermore, it covers the origin and characteristics of diverse error sources on GNSS measurements relevant for PPP. Their treatment in the software raPPPid capable of processing multi-GNSS and multi-frequency signals is explained. Finally, these two subjects are combined to model the code and phase observations.

3.1. Satellite products

Commonly the signal-in-space range error (SISRE) is used for the quality assessment of broadcast ephemeris. It is defined as the difference between the satellite position's and clock's true values and the broadcasted values. Neglecting other adverse influences, a user will not reach a considerable higher position accuracy than the level of the SISRE (Langley et al., 2017, chapter 1.2.4).

Montenbruck et al. (2018) present an overview of the SISRE of the broadcast ephemeris of all globally working GNSS. According to their results, GPS offers a root-mean-square SISRE stable at the 0.6 m level, GLONASS at the 2 m level, Galileo at the decimetre level (e.g., 0.2 m), and BeiDou around 1 m or slightly worse. The values for the 95th percentile are roughly two times higher. These SISRE values are clearly within the limits of the open service performance standards defined by the various providers. In accordance with these numbers, Hadas et al. (2019) showed that it is possible to achieve sub-decimeter and decimeter accuracy for the horizontal and vertical components with Galileo broadcast ephemeris after a considerable convergence time. However, besides the long convergence time, this does not hold for other GNSS and is still far away from a position accuracy at the centimeter level comparable to relative positioning methods (section 2.2.2). Therefore, satellite products (orbits, clock, and biases) of a higher quality than the broadcast ephemeris are obligatory for PPP at the present day.

The computations of high-quality satellite products requires lots of data, processing, and computational power. Therefore, they usually are provided in various versions with different latencies and increasing accuracies (section 3.1.2). Most satellite products are post-processed, but specific satellite products are available in real-time (section 3.1.3). The International GNSS Service provides both types.

3.1.1. The International GNSS Service

The first choice for obtaining GNSS related files is the International GNSS Service[5] (IGS), an organization devoted to the generation of high-precision GNSS data and products. The IGS is a service of the International Association of Geodesy (IAG), and provides an uninterrupted time service since the beginning of the 1990s (Johnston et al., 2017). Nowadays, it consists of more than 300 participating organizations in over one hundred countries. Since the type and quality of products have evolved over the years, data for other GNSS than GPS and real-time GNSS data and products are provided (Montenbruck et al., 2017). Dow et al. (2009) summarize the mission of the IGS:

> "The mission of the IGS is to provide the highest-quality GNSS data and products in support of the terrestrial reference frame, Earth rotation, Earth observation and research, positioning, navigation and timing and other applications that benefit society."

Several Analysis Centers (ACs) contribute to the IGS. Using GNSS observations, they generate high-quality products, such as precise orbits, clocks, and biases, but also tropospheric delays and ionosphere maps and station position estimates. The IGS creates combined solutions and makes all data, products, and solutions publicly available via several data centers. Examples are the FTP servers of the French Institut Geographique National (IGN) or the US-American Godard Space Flight Center (CDDIS).

Various Working Groups (WGs) provide technical guidance and expertise in specific fields to advance product generation and establish new data and processing standards. Since 2018, a WG for Precise Point Positioning with focus on ambiguity resolution exists. The PPP WG aims, for example, to generate a combined IGS satellite product allowing PPP with integer ambiguity resolution (section 5). Despite various strategies used from different ACs to create such satellite products, Banville et al. (2020) showed that the generation of a combined product is possible for GPS. Furthermore, Glaner and Weber (2021) compared various AC's satellite products enabling PPP-AR and tested their performance in a combined GPS and Galileo solution.

3.1.2. Post-processed satellite products

In post-processing, the IGS creates an orbit and clock combination for GPS in three different levels (ultra-rapid, rapid, final). For example, the final GPS orbits are the most accurate, available with a latency of 12-18 days. Furthermore, a final orbit and clock combination is computed for GLONASS. However, no combination of biases or a multi-GNSS orbit and clock combination is computed, currently.

To work on this challenging topic, the multi-GNSS WG launched the IGS Multi-GNSS Experiment (MGEX) in 2012. Montenbruck et al. (2017) summarize the achievements and

---

[5] International GNSS Service: https://www.igs.org/

progress of the MGEX over the first five years. Although substantial progress has been made, several open topics (e.g., satellite attitude) remain open. Nowadays, various ACs provide multi-GNSS satellite orbits, clocks, and biases in the course of the MGEX.

Satellite Orbits and Clocks Typically, post-processed satellite orbits are provided in the sp3c format (*.sp3) and satellite clocks in the clock RINEX format (*.clk). The respective format descriptions can be found on the IGS website[6]. Since these formats provide data in a specific time interval, it is necessary to interpolate orbits and clocks to the signal's transmission time (Kouba, 2015). The sp3 format contains the three-dimensional coordinates of each satellite with an interval of usually 15 or 5 minutes. To get the satellite position at the time of the emission of the signal, the Lagrange interpolation is recommended (Hofmann-Wellenhof et al., 2008, p.52f), and a polynomial of degree 11 has shown to be sufficient to achieve millimeter accuracy during the PPP tests. Note that the reference frame of the satellite orbits (e.g., IGS14 - the ITRS2014 realization of the IGS) defines the coordinate frame of the calculated user's coordinates.

Similarly, precise satellite clocks are provided in the clk format. For PPP high-rate clock products with a temporal resolution of 30 seconds should be used. Due to the much higher temporal resolution and the less dynamic satellite clock's behavior, a linear interpolation is sufficient for millimeter accuracy.

Product	GNSS	Comment	Reference
CNES	GRE	Enables conventional PPP-AR for GPS and Galileo with WL biases in the clock header	Katsigianni et al. (2019)
CODE	GRECJ	C01-C05 (GEO) lacking, Galileo PCO+PCV from Steigenberger et al. (2016)	Prange et al. (2020)
GFZ	GRECJ	Complete BeiDou constellation	Deng et al. (2016)
TUG	GRE	Raw observation product, repro3 product	Strasser (2022) and Strasser et al. (2018)
WUM	GRECJ	Complete BeiDou constellation	Guo et al. (2016)

Table 3.1: Overview of several final precise orbit and clock products of different analysis centers. Except for TUG, all products are part of the IGS MGEX product.

Table 3.1 shows an overview of various multi-GNSS precise orbit and clock products used in this thesis. Note that this table is not a complete listing, and more MGEX products and information can be found on the MGEX website[7]. All presented satellite products are computed with two frequencies and the IF LC in the latest version of the ITRF (currently IGS14). Since they are part of the IGS MGEX project, they are freely available on the FTP servers of the IGS. Contrary, the experimental satellite products of TUG are computed using a raw ob-

---

[6] IGS Formats and Standards: https://www.igs.org/formats-and-standards/
[7] MGEX Products: https://www.igs.org/mgex/data-products#products

servation approach (Strasser, 2022; Strasser et al., 2018). Furthermore, they are calculated using repro3 settings and, therefore, apply to a slightly different coordinate frame than the IGS MGEX products.

The satellite clock error's estimates contain biases or a combination of biases (e.g., the IF LC) between the frequencies used for computation of the satellite product. This circumstance has to be considered when processing a different observable than the reference observable used in the satellite clocks' computation. This mainly applies when a different PPP model than the IF LC is used in the processing (chapter 4).

The satellite products of CNES and CODE enable PPP-AR for two GPS and Galileo frequencies and the IF LC utilizing the so-called Integer Recovery Clock (IRC) method (Laurichesse et al., 2009). CNES provides the necessary phase biases in the clock header, while CODE provides them separately. This will be covered in detail in chapter 5. Note that CNES provides a file on their FTP server[8] indicating which satellites stayed unfixed in the IRC process on specific days.

Although currently no combined multi-GNSS orbit and clock product of the products listed in table 3.1 exists, significant efforts are made in this direction. Steigenberger and Montenbruck (2019) investigate the consistency of MGEX orbit and clock products of different ACs and provide an overview of the contributing ACs and products. They show that the consistency has significantly improved over the last years. However, further homogenization is needed for a successful combination, since except for GPS, some inconsistencies are found. Currently, initial tests for a combined multi-GNSS orbit and clock solution are performed[9].

Satellite biases   Code and phase measurements are contaminated with frequency and signal-dependent hardware delays of the satellites (Håkansson et al., 2017). If these code and phase biases are not appropriately considered, the estimated parameters absorb these imperfections degrading the performance of the PPP solution and impeding integer ambiguity resolution.

GNSS signal biases are commonly inaccessible in the absolute sense because they are highly correlated with other parameters (e.g., clock errors). Therefore, it is only possible to estimate and consider differences between biases, and, typically, satellite biases are corrected with suitable bias products when calculating the user's position. This approach is usually sufficient since other terms absorb common offsets in the positioning process (e.g., the receiver clock error) without influencing the calculated coordinates. The correct application of satellite biases depends on the PPP model and is handled in chapter 4, therefore.

Various institutions provide post-processed bias products suitable for PPP. Table 3.2 presents several products relevant for this thesis. Note that some of these products also include phase biases for ambiguity fixing and PPP-AR (chapter 5). Furthermore, table 3.3 lists separate

---

[8] CNES: *Unfixed Satellites*. ftp://ftpsedr.cls.fr/pub/igsac/GRG_ELIMSAT_all.dat
[9] IGS Analysis Center Coordinator: http://acc.igs.org/mgex_experimental.html

phase bias products allowing PPP-AR in conjunction with the IF LC and specific satellite orbits and clocks.

Bias Product	GNSS	Comment	Reference
CODE MGEX	GRECJ	Includes phase biases for GPS and Galileo conventional PPP-AR	Prange et al. (2020)
CAS Multi-GNSS DCBs	GRECJ	Daily product, latency 2-3 days	N. Wang et al. (2016)
CAS Multi-GNSS OSBs	GRECJ	Daily product, latency 2-3 days	N. Wang et al. (2020)
CNES post-processed	GREC	Code and phase biases for all frequencies, ambiguity fixing of any LC, consistent with GFZ rapid products	PPP-WIZARD (2021)
DLR Multi-GNSS DCBs	GRECJ	Weekly average, updated all 3 months	Montenbruck et al. (2014)
TUG Biases	GRE	Includes phase biases for GPS, GLONASS, and Galileo and PPP-AR (all combinations)	Strasser et al. (2018)
WUM MGEX	GRECJ	All GNSS and frequencies, corresponding to WUM orbits and clocks	Guo et al. (2016)

Table 3.2: Overview of various (code) bias products. Some products include phase biases indicated in the second-last column.

Bias Product	Type	GNSS	Comment	Reference
SGG$_{CNES}$, SGG$_{CODE}$, SGG$_{GFZ}$	WL and NL	GRECJ	Allows conventional PPP-AR for various MGEX products (e.g., CNES, CODE, or GFZ)	Hu et al. (2020)
WHU	Modified phase clock model	G	Allows conventional PPP-AR with orbits from CODE	Geng et al. (2019a)

Table 3.3: Overview of phase bias products enabling PPP-AR with the IF LC and specific orbit and clock products

In view of the diversity of GNSS frequencies and signals, a flexible new data format called SINEX BIAS has recently been developed and is used more and more frequently (Schaer, 2015). Although this format is not always easy to handle, it is an essential step towards comprehensively handling GNSS biases. Note that a complete overview of all GNSS signals can be found in the current version of the document describing the Receiver Independent

Exchange Format (RINEX) format[10]. The SINEX BIAS format allows the storage of code and phase biases specific to a particular GNSS, satellite, receiver, or satellite-receiver combination as a Differential Signal Bias (DSB), Observable-specific Signal Bias (OSB), or Ionosphere-free Signal Bias (ISB).

$$DSB_{E,C1X,C1C} = B_{E,C1X} - B_{E,C1C} \tag{3.1}$$

A DSB corresponds to the difference of two signal biases. For example, equation 3.1 shows the Differential Code Bias (DCB) between the Galileo C1X and C1C observation on the E1 frequency corresponding to the difference between the (non-accessible) absolute biases of C1X $B_{E,C1X}$ and C1C $B_{E,C1C}$. Due to the multitude of frequencies and signals, it is more practical to calculate DSBs from a specific subset instead of explicitly providing all DSBs. Furthermore, DSBs, OSBs, and ISBs can be converted into each other. The format specification of the SINEX BIAS format (Schaer, 2015) provides the formulas, therefore. For example, an ISB consists of two signal biases combined with the particular two factors used to compute the corresponding IF LC.

$$O_{G,C1C(ref)} = O_{G,C1W} - OSB_{G,C1W} \tag{3.2}$$

An OSB is a pseudo-absolute bias to the selected reference observable. Note that OSBs may be shifted by an arbitrary offset. OSBs are a very convenient representation for the user since he only has to subtract the matching OSB to the processed observation type to bias the observation to the reference observable. For the application of OSBs, a consistent satellite clock product is needed. Equation 3.2 shows an example, where a GPS C1W observation $O_{G,C1W}$ is biased to the reference observable of C1C.

3.1.3. Real-Time satellite products

Correction streams   The IGS Real-Time Service (RTS)[11] and several ACs provide correction streams as an real-time alternative to the post-processed IGS satellite products. The open standard of the Ntrip (Network Transport of RTCM via Internet Protocol) is used for dissemination among the various clients. The broadcasted streams are formatted according to the RTCM SSR standard or the recently introduced IGS State Space Representation (SSR) Format[12]. A Ntrip client, for example, the well-established BKG Ntrip Client (BNC)[13], is necessary to receive correction streams and use them in conjunction with the GNSS navigation messages for (real-time) PPP. A more detailed description of correction streams, SSR, Ntrip, and their application can be found in the BNC manual[14] and Huber (2015).

The orbit and clock corrections are linked to a specific set of broadcast ephemeris by an Is-

---

[10] IGS: *The Receiver Independent Exchange Format*. https://www.igs.org/wg/rinex/#documents-formats
[11] IGS Real-time Service: https://www.igs.org/rts
[12] IGS Formats and Standards: https://www.igs.org/formats-and-standards/
[13] BKG Ntrip Client: https://igs.bkg.bund.de/ntrip/bnc
[14] BNC: *Manual*. https://software.rtcm-ntrip.org/export/HEAD/ntrip/trunk/BNC/src/bnchelp.html

sue of Data (IOD) index. Orbit corrections are provided in a satellite-fixed coordinate system in the radial, along-track, and out-of-plane component (section 2.5.1). Similar to satellite positions computed from the broadcast message, the orbit corrections are transformed into ECEF for a correct application. The clock corrections are presented as the coefficients of a second-degree polynomial using the time difference between the observation's transmission time and the clock correction's reference epoch as parameter. The computed clock correction is added to the value issued by the broadcast message. Similarly, the code and phase biases from a correction stream are added to the raw observations by taking the latest set of biases corresponding to the processed observation type.

Furthermore, some correction streams provide information about the ionosphere in the form of spherical harmonics of the Vertical Total Electron Content (VTEC). For this purpose, the correction stream transmits the corresponding coefficients. Nie et al. (2019) introduce the formulas to calculate the VTEC from the transmitted coefficients and investigate the quality of the ionosphere message of CNES. Z. Li et al. (2020) present the first results of an IGS combined RTS ionosphere modeling. Recently, the IGS launched a new stream (IONO00IGS1) providing such a combination to the users.

Stream	Corrections	GNSS	Reference point
SSRC00CNE0	orbit (5), clock (5), code biases (5), phase biases (5), VTEC (120)	GREC	COM
SSRA00CNE0	orbit (5), clock (5), code biases (5), phase biases (5), VTEC (120)	GREC	APC

Table 3.4: The CNES correction streams. The numbers in parentheses indicate the update interval of the specific correction in seconds.

The IGS issues several streams providing multi-GNSS orbit and clock corrections. These are combined solutions of the individual streams delivered by the participating ACs (e.g., CNES). On the website of the IGS RTS[15] the users can find updated information and details on these streams. As the IGS streams currently do not provide code or phase biases, the correction streams of CNES (table 3.4) are used in this thesis.

Besides the already mentioned ionospheric information, the correction streams of CNES contain orbit, clock, code bias, and phase bias corrections for GPS, GLONASS, Galileo, and BeiDou. In this way, they enable a multi-GNSS PPP solution with integer ambiguity resolution independently of the PPP model (chapter 4) and an estimation of the user's position in the ITRF 2014. Kazmierski et al. (2018) evaluate the availability and quality of the CNES correction streams for float PPP.

Note that there is a difference between the reference point between various correction streams. Therefore, the name of the correction streams of CNES has been changed in 2020

---

[15] IGS Real-time Service: https://www.igs.org/rts

(from CLK91/CLK93 to SSR**A**00CNE0 and from CLK90/CLK92 to SSR**C**00CNE0) indicating the reference point (A for APC, C for COM) directly in the stream name. Similarly, the combined IGS streams have been renamed. More details about the CNES streams and archived daily files are available on the websites of Regina[16] and PPP-WIZARD[17].

Galileo HAS Currently still in a testing and experimental stage, the Galileo system will provide a so-called High Accuracy Service[18] (HAS). The Galileo HAS will offer PPP corrections enabling a positioning accuracy in the decimeter level with a convergence time of few minutes or less and an availability of 99 %. It will be the first free-of-charge service offering corrections for PPP via signal in space on a global scale.

The corrections of the Galileo HAS will be disseminated on the E6 frequency. In addition to that, they will also be available via the internet. The Galileo HAS will broadcast satellite orbits, clocks, code biases, and probably phase biases for GPS and Galileo in the first step (Service Level 1). In the second stage, the ESA plans to include also atmospheric corrections (Service Level 2).

The ESA currently promises an accuracy below 2 dm for the horizontal position error and below 4 dm for the vertical position error (95% quantile). Users shall reach this accuracy level within a convergence time of 300 s in the first and 100 s in the second stage. The operational start of the Galileo HAS is expected in 2022 with reduced performance and the FOC in 2024. It can be assumed that other GNSS will also offer such a service in the future.

3.1.4. Satellite attitude

The orientation of GNSS satellites and its change relative to the observer is crucial for the consistent application of the satellite orbits and consideration of error sources like Phase Wind-Up (section 3.2.5). To avoid imperfections, the PPP user has to apply the same attitude model as used during the computation of the satellite product.

In general, the desired orientation of a GNSS satellite during its orbital path around the Earth is driven by a small set of requirements (Hugentobler and Montenbruck, 2017): The boresight of the satellite antenna is directed to the center of the Earth to maintain optimal coverage and strength of the navigation signals. Furthermore, the GNSS satellite's solar panels are aligned perpendicular to the Sun's direction to maximize the projected area and received solar energy. Finally, one of the satellite faces, which is perpendicular to the antenna boresight and solar panel rotation axis, should point to the opposite side of the Sun. The atomic clocks of GNSS satellites are closely mounted to this cool panel easing their thermal stabilization.

To keep the described optimal orientation all the time, GNSS satellites have to perform a

---

[16] Regina: https://regina.cnes.fr/en/
[17] PPP-WIZARD: http://www.ppp-wizard.net/
[18] Galileo HAS: https://www.gsc-europa.eu/sites/default/files/sites/all/files/Galileo_HAS_Info_Note.pdf
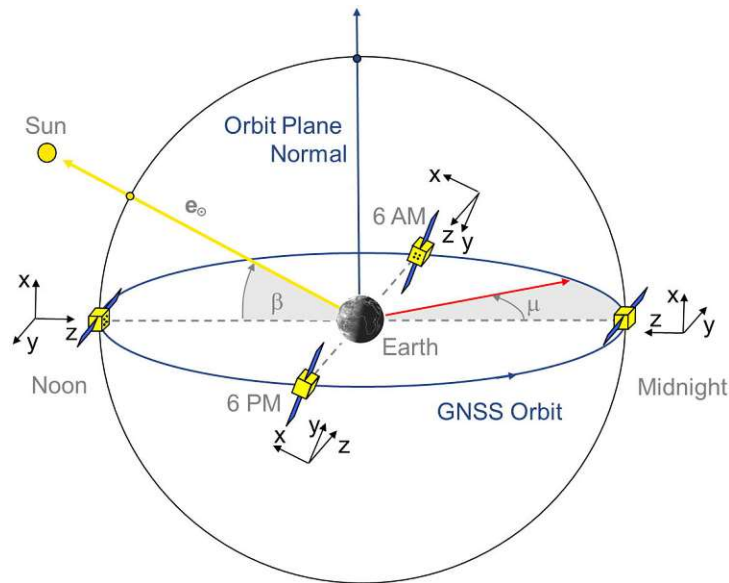
Figure 3.1: The orientation of a GNSS satellite in nominal yaw-steering mode (Montenbruck et al., 2015). The x-, y- and z-vectors indicate the axes of the corresponding satellite-fixed coordinate system.

permanent rotation during their orbital path around the Earth. The resulting attitude control mode is commonly known as the yaw-steering mode, and it is used by GPS, GLONASS, Galileo, and BeiDou (Montenbruck et al., 2015). Figure 3.1 shows the orientation of a GNSS satellite in yaw-steering mode.

Satellite eclipse The period where a GNSS satellite crosses the Earth's shadow is called an eclipse season. In this period, GNSS satellites can not rely on their Sun sensors for attitude control due to the missing solar radiation, and they perform rapid rotations. Therefore, the applied yaw-steering model might not reflect the actual satellite orientation deteriorating the observation model. Furthermore, fast re-orientations may destroy the constant property of the estimated ambiguities (Kouba, 2015).
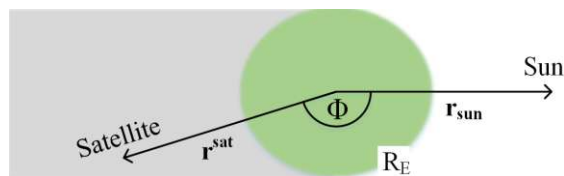
Figure 3.2: Cylindric model for the Earth's shadow

In general, GNSS satellites cross the Earth's shadow once per revolution. For example, GPS satellites transit the umbra twice a day in less than 60 minutes during an eclipse season (Leick et al., 2015). A simple option ignoring the distinction in umbra and penumbra is to detect GNSS satellites' eclipse seasons with a cylinder model (figure 3.2). The corresponding

formulas used for detection are presented below.

$$\cos \Phi = \frac{r^{sat} \bullet r_{sun}}{\|r^{sat}\|\|r_{sun}\|} \tag{3.3}$$

$$\cos \Phi < 0 \tag{3.4}$$

$$\|r^{sat}\| \sqrt{1 - \cos \Phi^2} < R_E \tag{3.5}$$

where Φ describes the angle between satellite and Sun as seen from the Earth's center. r^{sat} denotes the geocentric vector to the GNSS satellite, r_{sun} the geocentric vector to sun, and R_E the Earth´s radius, respectively. The symbol $\bullet$ denotes the dot product. If the inequalities 3.4 and 3.5 are true, the GNSS satellite passes the shadow of the Earth. The effect of eclipse seasons and the exclusion of satellites based on this cylinder model is illustrated in chapter 7.1.

IGS convention   Usually the IGS convention is used to describe the satellite's orientation in yaw-steering mode (Rebischung and Schmid, 2016). Therefore, a right-handed satellite fixed coordinate system X, Y, Z is used (section 2.5.1) requiring only the satellite's r^{sat} and the Sun's position r_{sun} in ECEF coordinates for its definition. Figure 3.1 illustrates the axes of this coordinate system. The Z-axis coincides with the antenna's boresight direction. Therefore, it points from the COM to the Earth's geocenter, and the negative Z-axis aims towards deep space. The Y-axis corresponds to the cross product of the Z-axis with the vector from the satellite to the sun corresponding to the solar panels' rotation axis. Finally, the X-axis completes the right-handed coordinate system. With the formulas 3.6-3.8 the axes are calculated as vectors in ECEF.

$$Z = \frac{-r^{sat}}{\|r^{sat}\|} \tag{3.6}$$

$$Y = Z \times \frac{r_{sun} - r^{sat}}{\|r_{sun} - r^{sat}\|} \tag{3.7}$$

$$X = Y \times Z \tag{3.8}$$

ORBEX Format   Currently, the so-called Orbit Exchange (ORBEX) format is under revision (Loyer et al., 2019). Its main philosophy is larger flexibility for the description of the satellite state than in different existing formats, which might be replaced at some point. The ORBEX format can hold many different types of records: position, clock, velocity, correlation coefficients. Moreover, it allows the inclusion of information on the satellite orientation in attitude (ATT) records. ORBEX is usable for GNSS and Low Earth Orbiting (LEO) satellites and ready for 0.1 mm precision.

```
*REC ID_           N ___q0__(scalar)_____  _____q1__x_____   _____q2__y_____   _____q3__z_____
## 2020 01 01 00 00 00.000000000000  76
 ATT G01           4 -0.0526906009210726  -0.2354221303419158    0.4049888929133578     0.8819206980997008
 ATT G02           4  0.5095202151101110   0.1753468364505604   -0.6131651631617999     0.5776427269737671
 ATT G03           4 -0.1286337650484338  -0.0130499760520848    0.3287545017575336     0.9355231318298122
 ATT G04           4 -0.1355517186582112  -0.1423544404616548    0.6242550438886595     0.7560863608274008
 ATT G05           4 -0.3955059396785496  -0.0075954618517932    0.9103271806034531    -0.1217447530401766
 ATT G06           4  0.1588336300641540   0.4297509301641739   -0.1290844296455663     0.8794448396612204
```

Figure 3.3: Excerpt of an ORBEX file of TUG showing the attitude information for the GPS
satellites G01-G06 at 00:00h on the January 1, 2020

$$
R = \begin{bmatrix} q_0^2 + q_1^2 - q_2^2 - q_3^2 & 2(q_1 q_2 - q_0 q_3) & 2(q_1 q_3 + q_0 q_2) \\ 2(q_1 q_2 + q_0 q_3) & q_0^2 - q_1^2 + q_2^2 - q_3^2 & 2(q_2 q_3 - q_0 q_1) \\ 2(q_1 q_3 - q_0 q_2) & 2(q_2 q_3 + q_0 q_1) & q_0^2 - q_1^2 - q_2^2 + q_3^2 \end{bmatrix} \tag{3.9}
$$

Figure 3.3 shows an excerpt of an ORBEX file and the attitude entries of six GPS satellites. An attitude entry for a specific satellite contains a quaternion corresponding to a quadruplet of real numbers. A quaternion can be interpreted as a four-dimensional vector, its norm equals one, and it can be used to describe rotations. The reason is that a quaternion is nothing different than another representation of a rotation matrix. To avoid quaternion operations and calculate the corresponding rotation matrix R from a quaternion (q_0, q_1, q_2, q_3), the formula 3.9 is used (Loyer et al., 2019). With the resulting rotation matrix R, local satellite body frame coordinates $\boldsymbol{X}$ can be transformed to coordinates in ECEF with $\boldsymbol{X_{ECEF}} = R\,\boldsymbol{X}$.

Consequently, the user can employ the ORBEX file's attitude entries instead of the IGS convention to calculate the satellite orientation. In this way, the user automatically applies the same satellite orientation as the satellite products' provider. This should be helpful in eclipse seasons. Furthermore, the ORBEX format and the attitude records could help to reduce existing inconsistencies in the satellite products of different IGS analysis centers (Loyer et al., 2017). The application of the ORBEX format in PPP is tested in section 7.1.

3.1.5. Applying precise orbits and clocks

Since most satellite products do not contain velocity information, the velocity is calculated as the difference between two very close satellite positions (e.g., 1 ms). Once the satellite position and velocity at the signal's emission time are identified, these ECEF coordinates have to be corrected for the Earth's rotation during the signal's run-time.

$$
\tau_R^S = \frac{r_{code} + dt^S + dt_{rel} - dt_R}{c} \tag{3.10}
$$

$$
w_\tau = \omega_E \cdot \tau_R^S \tag{3.11}
$$

$$
R_\tau = \begin{pmatrix} cos(w_\tau) & sin(w_\tau) & 0 \\ -sin(w_\tau) & cos(w_\tau) & 0 \\ 0 & 0 & 1 \end{pmatrix} \tag{3.12}
$$

The signal's run-time τ_R^S is approximately calculated with equation 3.10. Therefore, the pseudorange of the code observation r_{code} is used considering the satellite clock error dt^S, relativistic effects dt_{rel} (section 3.2.4), and the receiver clock error dt_R (all in the unit of meters). With the signal's run-time τ_R^S, the ECEF coordinates of the satellite position and velocity can be corrected for the Earth's rotation during the signal's run-time through a rotation around the z-axis (Earth's rotation axis). The rotation of the Earth during the signal's run-time w_τ is calculated with equation 3.11 and the value of the Earth's rotation rate ω_E. After building the rotation matrix R_τ (equation 3.12), the satellite position and velocity is simply multiplied with R_τ to correct for the Earth's rotation.

$$los = p^S - p_R \tag{3.13}$$

$$\rho = \|los\| \tag{3.14}$$

$$los_0 = \frac{1}{\rho} los \tag{3.15}$$

Once this correction is applied, the line-of-sight (los) vector los at the signal's reception time can be calculated as the difference between the satellite position p^S and receiver position p_R (equation 3.13). Its norm corresponds to the geometric distance ρ between receiver and satellite (equation 3.14). The los vector will be important for building the Design-Matrix (chapter 4). The corresponding unit vector los_0 is oriented from the receiver to the satellite (equation 3.15). This vector is useful, for example, to calculate the azimuth and elevation angle from the user to the satellite.
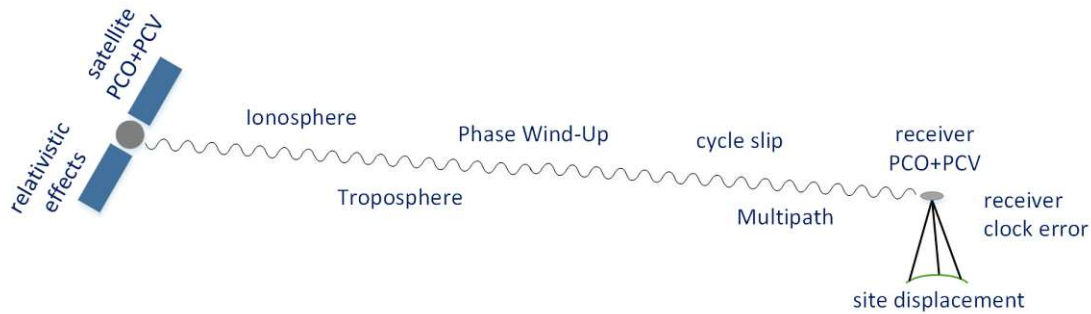
Figure 3.4: Error sources relevant for PPP

3.2. Error sources

A GNSS signal travels more than $20\,000\,\mathrm{km}$ and is affected by numerous effects until it is received by a user on the Earth's surface. Therefore, many different error sources with various origins have to be considered to achieve a position accuracy at the centimeter-level or even millimeter-level with PPP. Figure 3.4 gives an overview of these error sources, and the following sections present their theoretical background. Moreover, their consideration

and handling in the PPP model are explained. The starting point is the effect of the Earth's atmosphere on GNSS signals - a topic excellently outlined by Böhm and Schuh (2013).

3.2.1. Atmosphere

To reach a receiver on the Earth's surface, the electromagnetic signals of GNSS satellites have to cross the Earth's atmosphere. First, they pass the ionosphere before they enter the neutral atmosphere, in particular the troposphere. In both of these atmospheric layers, the electromagnetic signals are delayed and refracted.
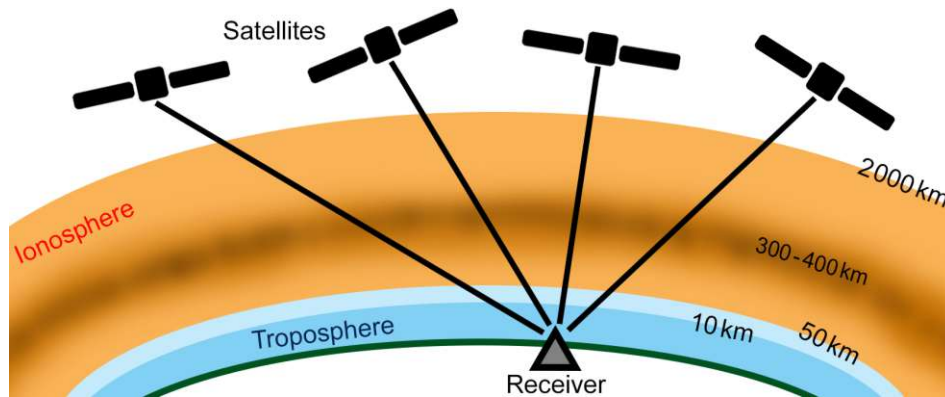
Figure 3.5: The atmosphere in context of GNSS signal refraction

In general, signals from satellites with low elevation angles are stronger affected by the atmosphere because of the longer signal path through the Earth's atmosphere (figure 3.5). The most left signal path (low elevation of, for example, 5°) is about ten times longer than for signals approaching from the zenith direction. Usually, the ionospheric delay is in the size of a few meters to 10 or 20 meters, but can reach up to 100 meters in extreme cases of ionospheric activity (Alizadeh et al., 2013). The tropospheric delay size typically varies between about 2 to 25 meters depending on the elevation angle of the satellite and the altitude of the station(Nilsson et al., 2013). Therefore, it is absolutely necessary to consider atmospheric delays, even for simple positioning models.

3.2.2. Ionosphere

Before GNSS signals cross the neutral atmosphere, they have to pass the ionosphere. The ionosphere can be characterized as the layer of the atmosphere where enough ionization happens that free electrons influence the propagation of GNSS signals. It is located from 50-2000 km above the Earth's surface, with the main concentration of free electrons between 300 km and 400 km (Alizadeh et al., 2013). The ionization and the number of free electrons is a direct consequence of solar radiation. Therefore, the number of free electrons experiences periodic changes over time (daily, seasonally, sun cycle) and depends on the geographic position. Typically, the ionosphere's effect on GNSS signals is more substantial

near the equator due to stronger solar radiation. Additionally, the number of free electrons varies with height inside the ionosphere, and the ionosphere shows irregular variations. In short, the ionospheric delay shows substantial variations and irregularities.

Most importantly, GNSS signals are delayed in the ionosphere. The resulting ionospheric delay is typically a range error of several meters to tens of meters but can reach up to 100 meters in extreme cases. All in all, the ionosphere is one of the most significant error sources on GNSS measurements, challenging to handle, and a dominant topic in GNSS positioning.

Theory A detailed description of the ionosphere and their effects on GNSS measurements can be found in Alizadeh et al. (2013), Seeber (2003), or the website of the Royal Observatory of Belgium[19]. The ionosphere is a dispersive medium in the microwave spectrum. Therefore, the ionospheric delay size depends on the signal frequency f, and the propagation speed of GNSS signals differs for the phase and group velocity in the ionosphere. While the phase velocity is relevant for the phase measurement, the group velocity is relevant for the code measurement.

$$n_p = 1 + \frac{c_2}{f^2} + \frac{c_3}{f^3} + \frac{c_4}{f^4} + ... \tag{3.16}$$

$$n_g = 1 - \frac{c_2}{f^2} - \frac{2c_3}{f^3} - \frac{3c_4}{f^4} + ... \tag{3.17}$$

In general, the propagation speed of a wave in a medium depends on the refraction index. For the ionosphere, the refraction index can be approximated with equations 3.16 and 3.17 for the phase and group velocity, respectively (Seeber, 2003, p. 54ff.). The coefficients c_n depend on the number of free electrons. When comparing equations 3.16 and 3.17 it gets clear that the influence of the ionosphere on phase and group velocity is approximately similar in size and opposite in sign.

$$n_p = 1 - \frac{40.31 N_e}{f^2} \tag{3.18}$$

$$n_g = 1 + \frac{40.31 N_e}{f^2} \tag{3.19}$$

Inserting $c_2 = -40.31 N_e$ and limiting the series expansion to the quadratic term (Seeber, 2003), a relation between the electron density N_e and the ionosphere refraction is obtained (equations 3.18 and 3.19). The influence of the ionosphere on phase and group velocity, respectively phase and code measurement, is now equal in size but different in sign.

The ionosphere's influence on the measured range is the difference between the integration of the refraction index over the measured range and true geometric distance. Because this difference is small further simplifications are possible (Alizadeh et al., 2013). Thus, the

---

[19] Royal Observatory of Belgium: *Ionosphere Tuturial*. http://gnss.be/ionosphere_tutorial

following expression for the ionospheric delay on GNSS observations can be obtained.

$$dIon = \pm \frac{40.31}{f^2} \int N_e(s)ds \qquad (3.20)$$

where $dIon$ is the slant signal delay in meters, and N_e the electron density along the signal path s. Therefore, the ionospheric delay is directly related to the integral of the electron density along the signal's path. Equation 3.20 is valid for phase measurements (minus sign) as well as code measurements (plus sign). Thus, the ionospheric delay results in an phase advance and a code delay, respectively.

$$dIon = \pm \frac{40.31}{f^2} STEC \qquad (3.21)$$

$$STEC = VTEC \cdot mf_{iono} \qquad (3.22)$$

Integration of the electron density along the signal path reveals the so-called $STEC$ (equation 3.21) representing the total amount of free electrons in a cylinder with a cross-section of $1\,\text{m}^2$ and a height of the slant signal path. The $STEC$ is measured in total electron content units (TECU) and 1 TECU accounts for 10^{16} electrons/m^2.

Usually, ionosphere maps in the IONEX format (Schaer et al., 1998) are used to provide information about the number of free electrons in a certain spatial and temporal resolution. These maps display the Vertical Total Electron Content (VTEC), which describes the integrated electron density in the zenith direction. To convert the VTEC to the STEC, a mapping function mf_{iono} is used (equation 3.22). The IONEX format description[20] provides details about the format and formulas for its application.

Ionospheric delay models   In general, the ionospheric delay can be modeled, eliminated, or estimated (Alizadeh et al., 2013). It is not easy to model the ionospheric delay precisely due to the characteristics of the ionosphere, and various physical and empirical models exist. The most famous example is the Klobuchar model (Klobuchar, 1987), and its coefficients are part of the GPS broadcast message. Similar, Galileo provides the NeQuick-Gal model (Nava et al., 2008). These models designed for the mass market and mainly used by low-cost single frequency receivers require only a few coefficients and reach a limited accuracy. More sophisticated or regional models reach a higher accuracy than the Klobuchar and NeQuick model, such as the regional Regiomontan model (Boisits et al., 2020). Ionosphere models can be provided through their coefficients series or converted to the standard IONEX format.

Using observations on multiple frequencies, the ionospheric delay can be eliminated or estimated. For elimination the most common way is the IF LC (section 2.4.1). By estimating the ionospheric delay, it is, for example, possible to create ionosphere maps. Various ACs operationally provide global ionosphere maps (GIMs) in different qualities and latencies in

---

[20] IGS Formats and Standards: https://www.igs.org/formats-and-standards/

the IONEX format (Hernández-Pajares et al., 2009; Schaer et al., 1998). Aggrey and Bisnath (2019) and Magnet (2019) provide an overview of existing GIM products.

Ionospheric delay in PPP   There are various options for considering the ionospheric delay determining the PPP model introduced in chapter 4. The feasibility and pros and cons of these PPP models are discussed there in detail.

Typically, the IF LC based on observations on two frequencies is used to eliminate the ionospheric delay in PPP (section 4.1).

Another logical option would be to model the ionospheric delay and correct the code and phase observations. Unfortunately, the ionospheric delay obtained from ionosphere models and maps usually does not reach an accuracy at the centimeter level. For example, the high-quality IGS GIMs are evaluated to provide an accuracy of 3 - 7 TECU corresponding to a range error of about 0.5 - 1 m on the GPS L1 frequency. These imperfections deteriorate the accuracy of the estimated parameters and coordinates (C. Shi et al., 2012). Therefore, it is not possible to reach centimeter-level positioning with this approach.

On the other hand, it is possible to directly estimate the ionospheric delay as an unknown parameter in the PPP processing. The so-called uncombined PPP model is covered in detail in section 4.2. Furthermore, it is possible to introduce information on the ionospheric delay in the uncombined PPP as so-called ionospheric pseudo observations leading to the 'uncombined model with ionospheric constraint'. This approach can be seen as an intermediate step between modeling and estimating and is discussed in section 4.2.1.

3.2.3. Troposphere

After passing the ionosphere, a GNSS signal needs to cross the neutral atmosphere. Since the troposphere is the main contributor in this atmospheric layer, the neutral atmosphere's effect is denoted as tropospheric delay. The troposphere contains the major part of the atmospheric mass (about 80 %). It is the lowest part of the atmosphere (up to 10 km from the surface) where all weather phenomena happen (Hobiger and Jakowski, 2017).

Troposphere and GNSS   Since the refraction index in the neutral atmosphere is close above 1 in the microwave spectrum, GNSS signals experience mainly a delay and no bending of the signal path (Nilsson et al., 2013). Therefore, a propagation delay of the signals occurs, similar to the ionosphere, and its size mainly depends on various meteorological parameters (Seeber, 2003). Contrary to the ionosphere, the neutral atmosphere is a non-dispersive medium in the microwave spectrum. Therefore, the tropospheric delay is practically frequency-independent for GNSS signals and has the same size for code and phase measurements. It is not possible to eliminate the tropospheric delay by means of GNSS observations on multiple frequencies and a multi-frequency LC (e.g., IF LC).

$$dTrop = dTrop_h^z \cdot mf_h + dTrop_w^z \cdot mf_w \tag{3.23}$$

Principally, the tropospheric delay can be split into a hydrostatic part and a wet part. Typically, the tropospheric delay in signal direction is represented as the sum of the zenith hydrostatic delay (ZHD) $dTrop_h^z$ and zenith wet delay (ZWD) $dTrop_w^z$ multiplied with the mapping functions mf_h and mf_w, respectively. This representation is shown in equation 3.23. While the hydrostatic part amounts to about 90 % of the total tropospheric delay, the wet delay amounts to only about 10 %.

The hydrostatic delay is mainly caused by the dry gases in the atmosphere. It is relatively stable and can be modeled with very high precision through pressure measurements at the site because the weight of all air layers adds up to the surface pressure. At normal meteorological conditions, the ZHD is typically about 2.3 meters at sea level (Nilsson et al., 2013).

Contrary to the hydrostatic delay, the wet delay is by far more variable due to the high spatial and temporal variability and unpredictability of the water vapor distribution (e.g., local weather). Typical values for the ZWD are between a few millimeters at the poles and about 40 cm at equatorial regions (Nilsson et al., 2013). Despite its small absolute value, it is not easy to highly accurate model the ZWD at the centimeter to the millimeter level. Therefore, the wet delay is usually estimated in space geodetic techniques. However, models can be used in this process to calculate initial values or estimate the residual wet delay.

$$mf(\epsilon, \alpha) = mf_0(\epsilon) + \delta mf(\epsilon, \alpha) \tag{3.24}$$

Using the satellites' elevation, the first term of the mapping functions converts the delay from the zenith direction into the direction of the signal (equation 3.24). Furthermore, the tropospheric delay varies depending on the horizontal direction due to specific climatic and weather phenomena. For example, at sites with northern latitudes, the path delay towards the south will be systematically bigger than the north because the height of the troposphere above the equator is larger than above the poles (Nilsson et al., 2013). Therefore, horizontal gradients $\delta mf(\epsilon, \alpha)$ are used and add an azimuthal dependency into the mapping functions. Finally, equation 3.25 takes all described phenomenons into account and shows a representation of the tropospheric delay for GNSS signals.

$$dTrop = dTrop_h^z \cdot mf_h(\epsilon, \alpha) + dTrop_w^z \cdot mf_w(\epsilon, \alpha) \tag{3.25}$$

Tropospheric delay in PPP   Since inaccurate handling of the tropospheric delay of the GNSS signals can prolong the convergence time and decrease the accuracy, troposphere models of the highest quality have to be used. Therefore, the discrete model Vienna Mapping Functions 3 (VMF3) and the empirical model Global Pressure and Temperature 3 (GPT3)

are mainly used in this thesis (Landskron and Böhm, 2018b). Furthermore, the tropospheric gradients of GRAD (=VMF3 gradients) and GPT3 are applied in consistence (Landskron and Böhm, 2018a). Note that a variety of studies reveal that the use of horizontal gradients improves the performance of PPP, as shown for example from Y. Xu et al. (2015). The mentioned troposphere delay models are created from numerical weather models. They have been developed by our research unit Higher Geodesy[21] and are available online[22]. Examples for other troposphere models are the Saastamoinen model (Saastamoinen, 1972), the Hopfield model (Hopfield, 1969), or the model from Askne and Nordius (Askne and Nordius, 1987). Further alternatives can be found in Nilsson et al. (2013) and Hobiger and Jakowski (2017).

VMF3 is a discrete model delivering zenith delays and mapping function coefficients (in continued fraction form) in a post-processed (operational) and forecast version for specific geodetic stations. To obtain VMF3 values for arbitrary sites, the user can interpolate grid-wise VMF3 data. As an alternative, GPT3 is an empirical model providing mapping functions for the hydrostatic and wet delay, meteorological parameters, and gradients. To obtain hydrostatic and wet zenith delays, these meteorological parameters are inserted, for example, in the formulas of Saastamoinen (1972) and the model of Askne and Nordius (1987).

To consider the tropospheric delay, the hydrostatic and wet delay are modeled, for example, using VMF3 or GPT3. Furthermore, a residual wet delay is estimated during the processing to account for local weather phenomena. This strategy is the standard approach for handling the tropospheric delay in PPP. Different options to handle the tropospheric delay are investigated in section 7.6.

3.2.4. Relativistic effects

Historically, GPS was one of the first practical uses of the theory of relativity's principles (Beard and Senior, 2017). Specifically, the satellite clocks are influenced by the special theory of relativity due to the satellite's velocity and the general theory of relativity due to the difference of the gravitational potential in relation to a user on the Earth's surface (Hofmann-Wellenhof et al., 2008, chapter 5.4). The sum of these effects on the satellite clock can be distinguished into a periodic term caused by the satellite orbit and a constant term.

Following the general theory of relativity, clocks placed at a different gravitational potential run at a different speed. Since the gravitational potential is smaller in the satellite's height than on the Earth's surface, the satellite clock runs faster than a clock placed on the Earth's surface. On the other hand, the satellite clock runs slower due to the satellite's movement compared to a clock placed on the Earth's surface. Since these two effects differentiate in size, they do no cancel. Their combination results for circular orbits in a constant clock drift

---

[21] Higher Geodesy, TU Wien: https://hg.geo.tuwien.ac.at/
[22] VMF Server: https://vmf.geo.tuwien.ac.at/index.html

compensated with a shift of the signal's frequency. For example, GPS satellites use a slightly modified fundamental frequency of 10.22999999543 Mhz instead of 10.23 MHz. The size of this shift results from the height of about 20 200 km above the geoid, and the velocity of about 4 km/s of GPS satellites.

$$dt_{rel} = \frac{-2}{c^2}\, p^S \cdot v^S \tag{3.26}$$

Since the orbits of GNSS satellites are not precisely circular, also a periodic term occurs, which must be corrected by the user. Equation 3.26 presents this correction in the unit of seconds using the speed of light c and the position and velocity vectors of the satellite p^S and v^S, respectively (Interface Control Document (ICD) of GPS[23]). In general, this effect is a function of the numerical eccentricity, semi-major axis, and eccentric anomaly of the satellite orbit. Since the eccentricity is limited by specification to be less than 0.02, this effect can reach 45 ns or 14 m in the range (Leick et al., 2015, p. 229).

Another relativistic effect affecting GNSS signals is a delay of the signals on their way through the Earth's gravitational field. Since its size is similar for all satellites and the maximum range error resulting from this effect is 18.6 mm (Hofmann-Wellenhof et al., 2008, p. 145), it can safely be ignored for PPP. Furthermore, the Sagnac correction is automatically applied (G. Xu, 2007, p. 66), when correcting the satellite position for the Earth's rotation before calculating the geometric distance between receiver and satellite (section 3.1.5).

3.2.5. Phase Wind-up

Navigation satellites usually emit right-handed circularly polarized radio waves. These waves are composed of two signal components created by two crossed and perpendicular dipoles. These dipoles generate a sine wave with a relative shift of 90°. The resulting field of the electromagnetic wave rotates in the plane of the dipoles.

If the receiving or transmitting antenna is rotated about its boresight (perpendicular to the dipoles), the electrical field's relative orientation is changed. This generates a shift in the measured carrier phase, and this effect is called Phase Wind-Up. In other words, the observed carrier phase depends on the relative orientation of the receiver and satellite antenna, and a rotation of either the satellite or receiver antenna has to be taken into account. For a static receiver Phase Wind-Up occurs due to the GNSS satellites' rotation along their orbital path around the Earth, as explained in section 3.1.4. A full rotation of 360° results in a shift of one wavelength (about 20 to 25 cm depending on the signal's frequency) in the measured carrier phase.

Usually, Phase Wind-Up is modeled for the phase observations using the formulas of Wu et al. (1993) requiring the satellite and receiver orientation in ECEF (section 2.5.1) and providing the Phase Wind-Up correction $\Delta\Phi$ on the frequency i in units of cycles. With the

[23] GPS: *Interface Control Document*. https://www.gps.gov/technical/icwg/
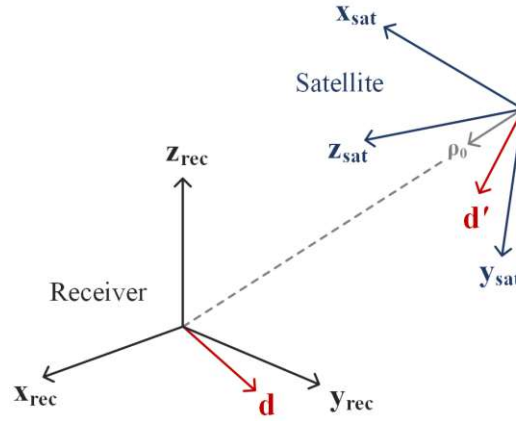
Figure 3.6: Orientation of the receiver's and satellite's antenna

corresponding wavelength, the correction is converted to units of meters.

$$\Delta\Phi_i = 2N\pi + \Delta\varphi \tag{3.27}$$

The Wind-Up correction $\Delta\Phi_i$ is composed of a integer number of full cycles N and a fractional part $\Delta\phi$ calculated with the following two equations.

$$N = \text{round}\left(\frac{\Delta\Phi_{prev} - \Delta\varphi}{2\pi}\right) \tag{3.28}$$

$$\Delta\varphi = \text{sign}\left(los_0 \cdot (d' \times d)\right) \arccos\left(\frac{d' \cdot d}{\|d'\| \, \|d\|}\right) \tag{3.29}$$

N is initialized as zero at the beginning of the processing. Afterward, the Phase Wind-Up correction from the previous epoch $\Delta\Phi_{prev}$ is used in equation 3.28. los_0 denotes the unit vector pointing from the receiver to the satellite (equation 3.15). For the calculation of $\Delta\phi$, the dipoles of the receiver d and transmitter d' are required (figure 3.6).

$$d = x_{rec} - los_0 \, (los_0 \cdot x_{rec}) + los_0 \times y_{rec} \tag{3.30}$$

$$d' = x_{sat} - los_0 \, (los_0 \cdot x_{sat}) - los_0 \times y_{sat} \tag{3.31}$$

where the unit vectors x_{rec} and y_{rec} correspond to the x- and y-axis of the receiver's coordinate system (section 2.5.1) and x_{sat} and y_{sat} to the x- and y-axis of the satellite's fixed coordinate system (section 3.1.4).

3.2.6. Multipath

The term Multipath itself is quite a good description for this error source. Multipath describes the phenomena when a GNSS signal reaches a receiver in more paths than only the direct way (figure 3.7). Usually, this results from reflections in the receiver's environment, such
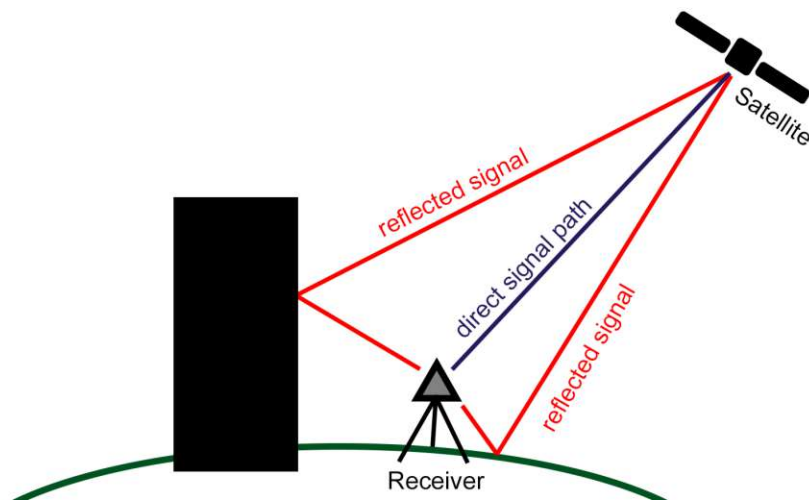
Figure 3.7: Schematic drawing of Multipath

as buildings or the ground. Typically, reflected signals have lower signal strength, and the measured range is longer. Multipath is challenging to assess because it strongly depends on the local environment of the receiver. It can lead to significant errors in the positioning process.

Multipath can be reduced with suitable antennas and cutoff angles since it occurs more likely when satellites are observed in low elevation angles. Furthermore, the receiver should not be placed at sites with many reflecting surfaces around. Unfortunately, these measures are not always realizable, and they only reduce the chance of Multipath. Therefore, section 7.4 illustrates the effect of Multipath in PPP and investigates the use of the MP LC (introduced in section 2.4.6) to reduce its impact.

3.2.7. Cycle slips

When the measured phases are plotted over time, a continuous curve should be the result (Seeber, 2003). A cycle slip is a jump or discontinuity in the carrier phase observation (figure 3.8). Hofmann-Wellenhof et al. (2008) identify three sources of cycle slips: The most frequent one is a physical obstruction that blocks the signal, for instance, a tree. Other sources are a low signal to noise ratio or a failure in the receiver software.

Cycle slips jeopardize the PPP solution and can cause significant errors in the parameters' estimation. The reason is that PPP relies on the precision of the phase observations and cycle slips destroy the assumption of constant phase ambiguities in the filter. Therefore, reliable methods to detect cycle slips presented in section 4.4.1 are an essential part of a stable PPP solution.
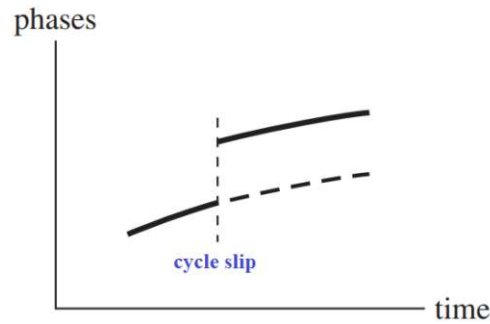
Figure 3.8: Illustration of a cycle slip (Seeber, 2003, Figure 7.41, slightly modified)

3.2.8. Antenna offsets and variations

The antenna's phase center (PC) is the location where the electromagnetic GNSS signals are emitted or received. In an ideal world, the PC would be a well-defined, measurable, and accessible point to which all GNSS signals refer. But the reality is more complicated. The PC is usually inside the antenna body and changes its location depending on the signal's frequency, elevation, and azimuth. Therefore, this effect must be modeled for the satellite and the receiver. Typically, a constant part, the phase center offset (PCO), and a variable part, the phase center variation (PCV), are used to locate the electromagnetic PC (figure 3.10). Usually, the PCO is in the size of centimeters to decimeters, and the PCV amounts from several millimeters to a few centimeters (Seeber, 2003).

The IGS provides and continuously updates a consistent set of absolute phase center corrections in the so-called Antenna Exchange (ANTEX) format (Rebischung and Schmid, 2016). An ANTEX file contains PCOs and PCVs for almost all GNSS satellites and receivers, originating from calibrations for different GNSS signals and frequencies. While the PCO is provided as a constant vector in the receiver or satellite's local coordinate system, the PCV is stored as a function of zenith-distance and azimuth in a grid with a particular resolution.

When processing a LC, the provided PCO and PCV values have to be scaled to the LC's frequency. Missing values for PCO or PCV, are usually replaced with the values of the GNSS's first frequency or the GPS values. The consideration of the receiver and satellite PCO and PCV in the observation model is essential for the accuracy of the PPP solution.

Satellite PCO and PCV The principles of orbital spacecraft dynamics used to describe GNSS satellites' motion refer to the COM and, therefore, also precise satellite coordinates distributed in the sp3 file format. However, all radio signals transmitted from GNSS satellites originate from their PC (figure 3.9). For this reason, the satellite PCO describes the difference from the COM to the PC as a constant vector in the satellite fixed coordinate system.

To calculate the range error on code and phase observations $\delta\rho^S_{PCO}$, the satellite PCO vector is transformed into an ECEF vector with equation 3.32 using the rotation matrix R describing the satellite's orientation (section 3.1.4). Together with the los-vector, the range
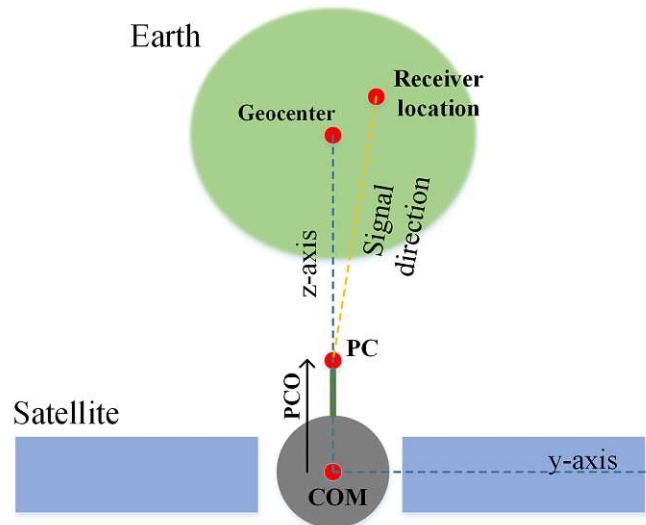
Figure 3.9: Satellite PCO and PCV from a GNSS satellites's point of view

error in the signal's direction is calculated with equation 3.33.

$$pco_{ECEF,i} = R\, pco_i \qquad (3.32)$$

$$\delta\rho^S_{PCO} = los \cdot pco_{ECEF,i} \qquad (3.33)$$

To correct for the PCV of the satellite, the signal direction's zenith-distance is calculated as the angle between the negative los-vector and the z-axis of the satellite fixed-coordinate system. The obtained range error is added to the observation model. Note that the azimuth-dependency is neglected because its magnitude ($<1\,\text{mm}$) is too small to affect the estimated PPP coordinates.

Receiver PCO and PCV The PCO of the GNSS receiver is a vector in the receiver's local-level coordinate system (North, East, Up - section 2.5.1). It represents the difference between a defined mean PC and the Antenna Reference Point (ARP). The ARP is a well-defined point typically on the bottom of the antenna useful to measure the antenna height above the ground. The antenna height is typically found in the RINEX file's header and considered analogously to the receiver PCO. Figure 3.10 shows the relations between PC, ARP, and station height. Using the zenith distance and azimuth to the specific satellite, the PCV of the receiver PC is found in the ANTEX file. Similar to the satellite PCO and PCV, the range error in the signal's direction is calculated using the receiver's orientation, the los-vector, and the signal's frequency.
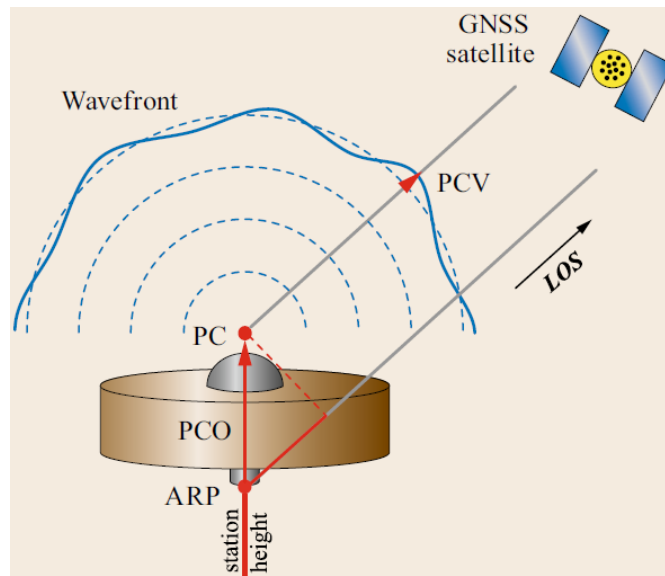
Figure 3.10: Illustration of the ARP, PC, PCO, and PCV of a GNSS receiver antenna (Maqsood et al., 2017, figure 17.38, slightly modified)

3.2.9. Site displacement effects

Different forces act on the Earth's surface, like lunar and solar gravity or various loading effects. This results in periodic deformations of the 'solid' Earth and movements of receivers placed Earth's surface. These effects are highly correlated over large areas, and it is not necessary to consider them in relative positioning with baselines up to a few hundred kilometers (Kouba et al., 2017).

Since PPP is an absolute positioning technique that delivers coordinates in a global reference frame, site displacement effects have to be considered and appropriately modeled. Unconsidered effects with notable amplitudes will deteriorate the observation model and influence the coordinates' precision. Therefore, only the dominant site displacement effects such as solid Earth tides and ocean loading are considered in raPPPid. They are discussed below in further detail. In general, their resulting displacement vector is calculated and projected to the line-of-sight. The resulting range error is added to the observation model to correct for these effects.

Of course, more tidal and non-tidal site displacement effects like ocean pole tides, polar tides, atmospheric pressure loading or surface hydrology, etc., exist. However, their amplitude is clearly under the level of accuracy reached with PPP (Kouba, 2015). Therefore they can safely be ignored.

Solid Earth tides   The same gravitational forces (mainly emerging from Sun and Moon) causing the ocean tides also deform the crust of the 'solid' Earth. The result is the largest tidal site displacement effect for GNSS positioning, which is called solid Earth tides and has

a magnitude of up to 30 cm in the radial and 5 cm in the horizontal direction (Kouba, 2015).

According to the IERS conventions, the solid Earth tides can be described by spherical harmonics of degree n and order m characterized by the Love number h_{mn} and the Shida number l_{nm} (Petit and Luzum, 2010). For an accuracy level at the millimeter level it is sufficient to calculate the displacement of the receiver in ECEF $\Delta \boldsymbol{x}_{solid}$ as the sum of the in-phase degree two and three tides neglecting other terms (e.g., frequency-dependency).

$$\Delta \boldsymbol{x}_{solid} = \Delta \boldsymbol{x}_2 + \Delta \boldsymbol{x}_3 \tag{3.34}$$

$$\Delta \boldsymbol{x}_2 = \sum_{j=2}^{3} \frac{GM_j}{GM} \frac{r^4}{R_j^3} \left[\frac{1}{2} h_2 \, \boldsymbol{r}_0 \, (3 R_{j,0}^2 - 1) + 3 l_2 R_{j,0} \big(\boldsymbol{R}_j - R_{j,0} \, \boldsymbol{r}_0 \big) \right] \tag{3.35}$$

$$\Delta \boldsymbol{x}_3 = \sum_{j=2}^{3} \frac{GM_j}{GM} \frac{r^5}{R_j^4} \left[h_3 \, \boldsymbol{r}_0 \left(\frac{5}{2} R_{j,0}^3 - \frac{3}{2} R_{j,0} \right) + l_3 \left(\frac{15}{2} R_{j,0} - \frac{3}{2} \right) (\boldsymbol{R}_j - R_{j,0} \, \boldsymbol{r}_0) \right] \tag{3.36}$$

where GM denotes the gravitational parameter of the Earth and GM_j of the Moon ($j = 2$) and Sun ($j = 3$), respectively. $\boldsymbol{r}$ is the geocentric vector to the station and $\boldsymbol{R}_j$ to the Moon and Sun. $\boldsymbol{r}_0$ and $\boldsymbol{R}_{j,0}$ are the corresponding unit vectors. Furthermore, the relation $R_{j,0} = \boldsymbol{R}_j \cdot \boldsymbol{r}_0$ is used to improve the readability of the presented equations. The IERS conventions (Petit and Luzum, 2010) provide the formulas to correct the second degree Love number h_2 and Shida number l_2 for the geocentric latitude of the station and the values for the constant third degree Love and Shida numbers (h_3 and l_3).

Ocean loading The ocean tides create a deformation of the seafloor and the adjacent land. This effect is called ocean loading and mainly affects coastal stations. It is a secondary tidal effect because ocean loading is a result of the Earth's elastic response to the varying seawater load due to ocean tides. As one can easily imagine, the site displacement is most distinct in the vertical direction and shows a predominant semidiurnal and diurnal periodicity. Its magnitude is in the order of 1 - 10 cm (Langley et al., 2017). Thus, the resulting site displacements are about an order of magnitude smaller than these caused by solid tides.

Ocean loading is much more location-specific, and it may be neglected for static positions far off the coast (e.g., over 1000 km, (Kouba et al., 2017)). Ocean loading has to be considered for PPP with an accuracy at the centimeter level along coastal regions (Kouba, 2015). Otherwise, unmodeled ocean loading effects may contaminate the estimation of the tropospheric zenith wet delay and the receiver clock, and these parameters are highly correlated with the vertical position (Dragert et al., 2000).

To correct for the effect of ocean loading, the coordinate shift Δc is calculated as a harmonic series with the following formula for all three coordinate axes of the receiver's local-

level coordinate system (Petit and Luzum, 2010).

$$\Delta c = \sum_{j=1}^{11} A_{cj} \cos(\chi_j(t) - \Phi_{cj}) \tag{3.37}$$

The terms considered in equation 3.37 correspond to one of 11 semidiurnal (M_2, S_2, N_2, K_2), diurnal (K_1, O_1, P_1, Q_1) and long-period (M_f, M_m and $S_s a$) tidal waves. The time-dependent angles χ_j are linear combinations of fundamental astronomical arguments (for example the mean longitudes of Sun and Moon) and are computed following the equations provided in Petit and Luzum (2010). The station-specific amplitudes A_{cj} and phases Φ_{cj} can be obtained from an ocean loading provider service like the one from M. S. Bos and H. - G. Scherneck[24]. To use the ocean loading correction for a specific station the amplitudes A_{cj} and phases Φ_{cj} have to be downloaded manually and copied to the data folder of raPPPid (*.blq format).

3.2.10. Receiver clock error

As mentioned earlier (section 2.2.1), it is necessary to estimate a receiver clock error. In the simplest case, the observations of a single GNSS are used to calculate the PPP solution, and the receiver clock error is estimated for this GNSS. For example, in a PPP solution calculated with Galileo observations, the Galileo receiver clock error is estimated.

$$dt_R = dt_R^{gps} + \delta t_R^g \tag{3.38}$$

When multiple GNSS are processed, things get more complicated: A receiver clock offset is added to the observation model and estimated for each processed GNSS other than the GNSS of the highest order (table 2.2). Typically, the GNSS of the highest order is GPS. Therefore, the GPS receiver clock error and, depending on the number of processed GNSS, a certain number of receiver clock offsets to the GPS receiver clock error are estimated (equation 3.38). An equivalent option would be to estimate the receiver clock error for each processed GNSS.

The receiver clock offset describes the difference between the receiver clock errors of two GNSS. Therefore, this parameter is often called Inter-System Bias (ISB) in scientific research. For example, the GLONASS ISB typically represents the difference between the GPS and the GLONASS receiver clock error. The ISB contains offsets of inter-system satellite clock datums and receiver biases. ISBs depend on the satellite datum of the used satellite products, the receiver type, the antenna type, and the environment (e.g., temperature) (Ke et al., 2020). Since the ISB is not correlated with the coordinates and ZWD, it can be assimilated into clock and ambiguity parameters without affecting the coordinate estimation (Chen et al., 2015). However, this alternative approach sophisticates the integer fixing of the phase ambiguities.

---

[24] Bos and Scherneck: *Free ocean tide loading provider*. http://holt.oso.chalmers.se/loading/index.html

Figure 3.11 shows the GPS receiver clock error for various IGS stations and receivers. The size and behavior differ considerably ruling out assumptions on its behavior in advance. The sections 4.4 and 4.4.3 look into more details on the parameter estimation and stochastic settings of the receiver clock error and offset.
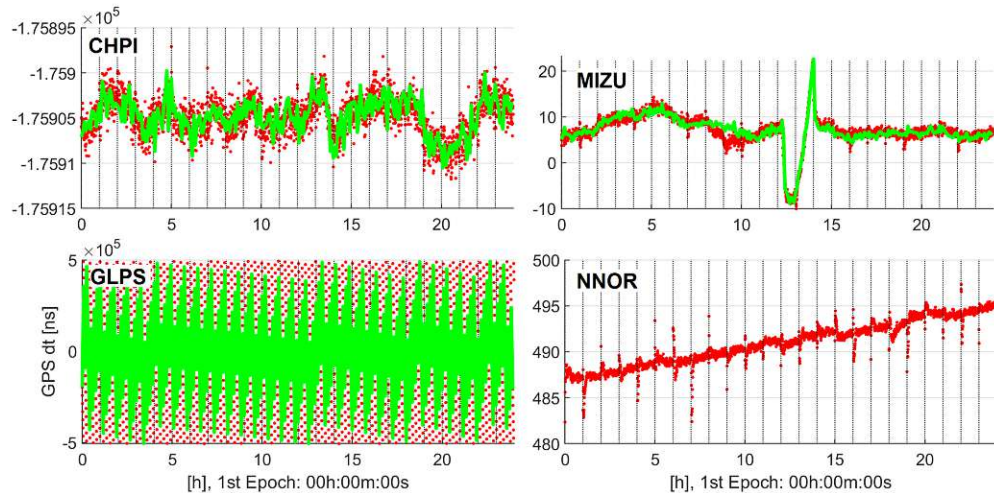
Figure 3.11: The GPS receiver clock error (red) in units of nanoseconds determined with raPPPid for various IGS stations on January 3, 2020. If available, the corresponding estimates of CODE are shown in green. A reset of the PPP solution was performed every full hour.

3.2.11. Receiver DCBs

Due to instrumental delays, code observations on different frequencies have diverging reception times, and so-called receiver code biases occur (Håkansson et al., 2017). Since GNSS signals travel with the speed of light, already tiny deviations result in significant range errors.

As biases are commonly inaccessible in the absolute sense, these differences are considered as receiver Differential Code Biases (DCBs) between the 1st and each other processed frequency. Basically, they can be estimated or corrected with known values. Furthermore, inter-frequency code biases originating from the receiver are neglected for GLONASS observations applying the FDMA technique.

When processing the IF LC, the receiver DCBs are converted in a constant offset absorbed from the receiver clock estimation. Therefore, receiver DCBs are mainly of interest in conjunction with the uncombined PPP model and their consideration will be treated in section 4.2.

3.2.12. Group Delay Variations

Group Delay Variations (GDVs) are systematic code-phase divergences depending on the signal's direction and frequency. GDVs may be caused by spacecraft internal multipath. While

this effect is not noticeable using broadcast ephemeris, precise applications employing code measurements like PPP are severely affected.

GDVs can be determined using the MP LC for two frequencies presented in section 2.4.6. In doing so, Wanninger and Beer (2015) detect pronounced GDVs originating from BeiDou-2 IGSO and MEO satellites and provide correction values. The identified GDVs reach meter-level, do not show temporal variations, and are independent of the receiver, antenna, and signal's azimuth. Note that BeiDou 3 satellites do not exhibit this effect. Section 6.6 presents PPP results focusing on the inclusion of BeiDou signals and applying the corrections from Wanninger and Beer (2015) on the code observations of BeiDou-2 IGSO and MEO satellites.

Although GDVs have been investigated for GPS, GLONASS, and Galileo, and their consideration might improve the PPP performance, they are neglected. The reason is that they are more than a magnitude smaller than for BeiDou-2 (Wanninger et al., 2017; Beer et al., 2020). Therefore, their size is at or clearly below the noise level of code observations.

3.2.13. Other error sources

There are undoubtedly more error sources affecting GNSS measurements than the mentioned error sources. Examples are atmosphere bending, ionospheric effects of a higher-order (Zus et al., 2017), atmospheric loading, or pole tides. Since their magnitude is at the millimeter-level or below, they usually are not considered and can safely be neglected for PPP.

3.3. Observation model

The theoretical values for the code and phase observation can be computed by applying the used precise satellite products and considering all presented error sources. The resulting modelled observations (equations 3.39 and 3.40) are essential for computing a PPP solution and to calculate, for example, the 'observed minus computed' vector (section 4.4).

$$
\begin{aligned}
P_i^{model} = {} & \rho - c \cdot dt^S - dt_{rel} + c(dt_R^{GPS} + \delta t^g) - DCB_{1i} \\
& + \frac{f_1^2}{f_i^2} \cdot dIono_1 + dTrop + dTrop_{residual}^{wet} \\
& - \delta\rho_{solid} - \delta\rho_{ocean\,loading} + \delta\rho_{GDV_i} \\
& - \delta\rho_R^{PCO_i,PCV_i} + \delta\rho_R^{ARP_i} + \delta\rho_{PCO_i,PCV_i}^{S}
\end{aligned}
\tag{3.39}
$$

$$
\begin{aligned}
L_i^{model} = {} & \rho - c \cdot dt^S - dt_{rel} + c(dt_R^{GPS} + \delta t^g) - DCB_{1i} \\
& - \frac{f_1^2}{f_i^2} \cdot dIono_1 + dTrop + dTrop_{residual}^{wet} \\
& - \delta\rho_{solid} - \delta\rho_{ocean\,loading} \\
& - \delta\rho_R^{PCO_i,PCV_i} + \delta\rho_R^{ARP_i} + \delta\rho_{PCO_i,PCV_i}^{S} \\
& + \delta\rho_{Wind-Up_i} + \lambda_i N_i
\end{aligned}
\tag{3.40}
$$

The equations 3.39 and 3.40 show the observation model for the code and phase measurement, respectively. The previous sections introduce all included error sources, and the respective term in the observation model represents the resulting range error. The majority of the considered effects is modeled, but some are estimated as parameters during the PPP solution (e.g., phase ambiguity).

Basically, the observation model is identical for the code and phase observation apart from the following differences: the sign of the ionospheric delays differs, equations 3.39 includes GDVs for the code observation, and equation 3.40 involves terms for Phase Wind-Up and the ambiguity of the phase measurement.

Table 3.5 details all terms noted in the equations 3.39 and 3.40. Furthermore, the table provides a rough estimate of the order of magnitude. The sign (plus or minus) in front of a specific term in the equations 3.39 and 3.40 depends on the concrete implementation.

Keep in mind that the equations 3.39 and 3.40 include all generally relevant error sources for PPP. Depending on the chosen PPP model (chapter 4), some terms might be zero. For example, the ionospheric delay and receiver DCBs must not be considered when processing the IF LC. Furthermore, the PPP user might decide to neglect or ignore specific error sources. For example, ocean loading can be neglected for stations far off the coast. Another possibility

is that the used satellite products are of lower accuracy than the error sources' magnitude. For example, PPP solutions achieving dm-level accuracy (e.g., using the Galileo HAS) can safely ignore receiver and satellite PCVs.

Two mentioned error sources are missing in equations 3.39 and 3.40. Because it is impossible to model Multipath or cycle slips, these error sources are not included in the observation model's equations. They have to be detected with proper algorithms to exclude contaminated observations from the parameter estimation. Section 4.4.1 will discuss causes to exclude observations.

Note that the satellite orbits (and also the unknown receiver coordinates) are implicitly included in the theoretical distance ρ. Furthermore, satellite code and phase biases are also not considered in the equations 3.39 and 3.40. They are appropriately corrected before computing the modeled observations. Furthermore, receiver phase biases are ignored since they are assimilated in the estimation of the float ambiguity. For the calculation of the fixed solution covered in chapter 5, a reference satellite will be used to build single differences and eliminate the receiver phase biases.

Symbol	Description	Magnitude	Section
ρ	Theoretical distance	$2 \cdot 10^7$ m	3.1.5
dt^S	Satellite clock error	μs-ns	3.1
dt_{rel}	Relativistic effects	10 ns	3.2.4
dt_R^{GPS}	Receiver clock error	ns-ms	3.2.10
δt^g	Receiver offset GNSS	ns	3.2.10
DCB_{1i}	Receiver DCB	ns	3.2.11
$dIono_1$	Ionospheric delay	1-100 m	3.2.2
$dTrop$	Tropospheric delay	1-15 m	3.2.3
$dTrop_{residual}^{wet}$	Residual wet delay	mm-dm	3.2.3
$\delta\rho_{solid}$	Solid Earth tides	cm	3.2.9
$\delta\rho_{GDV_i}$	Group Delay Variations	mm-1 m	3.2.12
$\delta\rho_{oceanloading}$	Ocean loading	mm-cm	3.2.9
$\delta\rho_{PCO_i,PCV_i}^S$	Satellite PCO and PCV	1 m, mm-cm	3.2.8
$\delta\rho_R^{PCO_i,PCV_i}$	Receiver PCO and PCV	cm-dm, mm-cm	3.2.8
$\delta\rho_R^{ARP_i}$	Receiver ARP (height)	cm-1 m	3.2.8
$\delta\rho_{Wind-Up_i}$	Phase Wind-Up	cm-dm	3.2.5
N_i	Phase Ambiguity	-	-

Table 3.5: Overview of relevant error sources for PPP including the corresponding section and magnitude. The stated terms are used in equation 3.39 and 3.40 to model the code and phase observations.

4. PPP Models

In this chapter, the procedure to establish a stable PPP float solution is outlined based on the precise satellite products and consideration of error sources presented in the last chapter. PPP models suitable for determining the user's position are developed, and the corresponding observation equations containing all unknown parameters are introduced. Furthermore, the detection of outliers and correct application of code biases are covered. Finally, Kalman Filtering used for parameter estimation during the float solution is introduced including the functional and stochastic model.

4.1. Conventional model

Historically, PPP was developed for dual-frequency GPS observations (Héroux and Kouba, 1995; Malys and Jensen, 1990; Zumberge et al., 1997). For that reason the conventional PPP model uses observations on two frequencies to build the IF LC.

$$P_{IF} = \rho + c(dt_R^{GNSS_1} + \delta t_R^g) + dTrop^{wet} + \varepsilon \tag{4.1}$$

$$L_{IF} = \rho + c(dt_R^{GNSS_1} + \delta t_R^g) + dTrop^{wet} + \lambda_{IF}(\overline{N}_{IF} + b_{R,IF} - b_{IF}^S) + \varepsilon \tag{4.2}$$

The equations 4.1 and 4.2 present the observation equations of the conventional PPP model for the code P_{IF} and phase measurement L_{IF} in units of meters. Note that the unknown user coordinates are included in the term of the geometrical distance ρ. Since precise satellite products are applied, no satellite code biases, satellite clock errors, or satellite orbit errors are included in the observation equations. The correct application of the satellite code biases will be detailed in section 4.3.

   Furthermore, various error sources covered in chapter 3 are modeled and, therefore, excluded from these equations. According to section 3.2.3, the tropospheric delay $dTrop$ is split into a hydrostatic and a wet part $dTrop^{wet}$. Since the hydrostatic part is modeled, it is omitted from the observation equations. By including a receiver clock offset δt_R^g in addition to the receiver clock error $dt_R^{GNSS_1}$ as described in section 3.2.10, the conventional PPP model is applicable for the observations of multiple GNSS.

$$N_{IF} = \overline{N}_{IF} + b_{R,IF} - b_{IF}^S \tag{4.3}$$

For the float solution, the integer ambiguity term $\overline{N}_{IF}$ is lumped together with phase hardware delays originating from the receiver $b_{R,IF}$ and satellite b_{IF}^S. The resulting float ambiguity N_{IF} (equation 4.3) is estimated as a real-valued number. Chapter 5 looks into possibilities to fix the phase ambiguities to integer values and calculate a fixed position.

   Since higher-order terms of the ionosphere, which only amount up to 0.1 % percent of the total ionospheric delay, are neglected, the IF LC conveniently eliminates the ionospheric delay from the observation model. Considering the strong variations and challenging na-

ture of the ionosphere (section 3.2.2), this is quite comfortable. Furthermore, receiver code biases (section 3.2.11) are converted to a constant offset absorbed by the receiver clock estimation. Consequently, it is not necessary to consider these two error sources at all. On the other hand, no information about the ionospheric delay can be obtained from or introduced into the observation model. Thus, the information offered by ionosphere models like global ionosphere maps cannot be entered.

Observations on two frequencies are essential for building the IF LC. Therefore, a single missing observation prevents the IF LC's formation. Moreover, it is not clear how to extend this PPP model for modern GNSS signals on three or even more frequencies. Neither a 3-frequency IF LC or the use of two 2-frequency IF LCs are sensible approaches. Furthermore the coefficients of the IF LC increase the observation noise elongating the coordinate convergence time (Lou et al., 2016; Boisits et al., 2020).

Altogether, the conventional model is a well-established and convenient approach to PPP. However, it shows some limitations in the view of the developing multi-frequency and multi-GNSS landscape and for reducing the convergence time. Therefore, the uncombined model has received more and more attention in the last few years.

4.2. Uncombined Model

The uncombined model is a more direct application of the GNSS observation equations (section 2.3). Contrary to the conventional PPP model, the raw observations are processed, and no LC is formed (An et al., 2020; Lou et al., 2016). Consequently, the original observation noise is maintained and not increased through the coefficients of a LC.

$$P_i = \rho + c(dt_R^{GNSS_1} + \delta t^g) - DCB_{1i} + dTrop^{wet} + \gamma_{1i} \cdot dIono_1 + \varepsilon \tag{4.4}$$

$$L_i = \rho + c(dt_R^{GNSS_1} + \delta t^g) - DCB_{1i} + dTrop^{wet} - \gamma_{1i} \cdot dIono_1 + \lambda_i N_i + \varepsilon \tag{4.5}$$

The equations 4.4 and 4.5 present the observation equations of the uncombined model for the code P_i and phase measurement L_i on the frequency i in unit of meters. Some parameters (e.g., tropospheric delay, receiver clock error and offsets) are handled similarly to the conventional PPP model.

$$N_i = \overline{N}_i + b_{R,i} - b_i^S \tag{4.6}$$

Again the ambiguity term $\overline{N}_i$ is lumped together with phase hardware delays originating from the receiver $b_{R,i}$ and satellite b_i^S. The resulting float ambiguity N_i (equation 4.6) is estimated as a real-valued number. Chapter 5 looks into the integer fixing of the phase ambiguities in the uncombined model (section 5.3).

In contrast to the conventional PPP model, the ionospheric delay $dIono_1$ must be considered and is part of the uncombined model's observation equations. The ionospheric delay is estimated on the first frequency for each satellite of the corresponding GNSS (e.g., GPS L1 or Galileo E1 ($\gamma_{1i} = 1$)). The ratio of the squared frequencies γ_{1i} (equation 2.17) is

used for the conversion to other frequencies. Alternatively, it is possible to estimate a zenith ionospheric delay above the user's position, similar to the handling of the tropospheric delay (C. Shi et al., 2012; Lou et al., 2016).

Contrary to the conventional model, the uncombined model can be easily extended to any number of frequencies. It is suitable for processing three or even more frequencies and can be applied on single-frequency data (Ning et al., 2019). A further advantage is its flexibility, especially in view of the current development of GNSS constellations and additional frequencies. Missing observations (e.g., GPS L5 or GLONASS G3) are easily considered and excluded from the parameter estimation process without preventing the formation of the IF LC. Note that the uncombined model can even process a different number of frequencies for each GNSS.

Another difference to the conventional model is that receiver code biases have to be taken into account. Since it is impossible to access them in the absolute sense, the observation equations contain the receiver differential code bias from the first to the particular frequency DCB_{1i}. Usually, they are estimated during the PPP solution, but it is also possible to correct them with known values (Zhang et al., 2013).

Due to the estimation of the ionospheric delays and receiver DCBs, the number of unknowns is considerably higher in the uncombined model compared to the conventional approach. Also, the number of observations is higher, as shown at the end of the section 4.4.2 in detail. Consequently, the computational effort with the uncombined model is considerably higher than with the conventional model.

Note that a rank-deficiency between the ionospheric delay and the receiver DCBs exists. Therefore, it is impossible to separate the ionospheric delay from the receiver DCBs meaningfully, and the estimated values of the ionospheric delay and receiver DCBs are contaminated by each other, resulting in non-sensible values and an elongated convergence time (Zhang et al., 2013). For example, the estimated ionospheric delay may be negative. A possibility to remove this rank-deficiency is to use an ionospheric constraint presented in the next section.

4.2.1. Ionospheric constraint

$$dIono_{pseudo} = dIono_1 + \varepsilon \tag{4.7}$$

The uncombined model offers the possibility to introduce ionospheric delays from external ionosphere models (De Bakker, 2016), and constraining the ionosphere with so-called ionospheric pseudo-observations has proven as the most promising approach (Ning et al., 2019). Therefore, the modeled ionospheric delay on the first frequency is added as additional pseudo-observation for each satellite (equation 4.7) in addition to the code and phase observations. In this way, the uncombined model with ionospheric constraint emerges. By including ionospheric pseudo-observations, the rank-deficiency between the ionospheric delay and receiver DCBs is removed, and the ionospheric delay and receiver DCBs can be separated

meaningfully during the parameter estimation process.

Typically, the ionospheric delay from ionosphere models is less precise than the slant ionospheric delay estimated within a PPP solution. Due to the presented approach, the inevitable imperfections of the ionosphere model and consequently the ionospheric pseudo-observations are compensated in the filter process by the estimation of the ionospheric delay. Therefore, the additional pseudo-observations potentially add valuable information to the PPP solution, strengthen the estimation of the parameters, and shorten the convergence time. However, a high-quality ionosphere model and reasonable weighting of the ionospheric pseudo-observations (section 4.4.3) are necessary to fully exploit the potential of the ionospheric constraint.

Since the noisy code observations are the limiting factor, the ionospheric constraint is especially helpful in the first minutes of PPP processing. Consequently, coordinate differences between PPP solutions calculated with varying ionosphere models and identical constraint show up. This differences mainly concern the first minutes of the processing and decrease over time. The results of Aggrey and Bisnath (2019) and Boisits et al. (2020) show that the improvement associated with the constraint vanishes with increasing processing time.

4.3. Code bias application

The careful consideration of various types of delays is essential in a multi-GNSS and multi-frequency PPP solution. In this regard, the correct application of biases compensating signal delays originating from the satellite is crucial and depends on the employed PPP model and satellite products. Note that phase biases are ignored at this stage since they are absorbed from the float ambiguities. However, their consideration is covered in chapter 5 to enable integer ambiguity fixing.

Due to a linear dependency, the satellite clock product contains signal delays of the observation types used during its computation, the satellite clock offset. Usually, satellite products are computed with observations on two frequencies and the IF LC (IGS convention). Therefore, the satellite clock offset is a combination of the signal delays of the reference observables (e.g., GPS C1W and C2W) used to build the IF LC. Keep in mind that the RINEX format description[25] gives an overview of all GNSS signals and their denotation. In the simplest case, when processing the same observation types as adopted in the clock product's computation with the conventional PPP model, the satellite clock offset is directly eliminated for obvious reasons.

However, suppose observation types differing from the reference observables (e.g., GPS C1C and C2C instead of C1W and C2W) are processed with the conventional model or another PPP model (e.g., uncombined model) is used. In that case, the observations have to be shifted according to the reference observables of the satellite clock product. Therefore, the user can apply suitable satellite code biases typically expressed as OSBs or DSBs introduced

---

[25] IGS: *The Receiver Independent Exchange Format*. https://www.igs.org/wg/rinex/#documents-formats

in section 3.1.2. Usually, they are provided in the unit of seconds (e.g., nanoseconds) but can be converted to meters by multiplication with the speed of light. Then these OSBs and DSBs can be used as range corrections.

$$O_{ref} = O_{type} - OSB_{type} \tag{4.8}$$

$$O_{ref} = O_{type} - DSB_{type, ref_1} - \frac{f_{ref_2}^2}{f_{ref_1}^2 - f_{ref_2}^2} DSB_{ref_1, ref_2} \tag{4.9}$$

Satellite biases in OSB representation must be used together with the corresponding satellite clock product for full consistency. Then, the matching OSB has only to be subtracted from the processed observation type as shown in equation 4.8.

On the other hand, when the satellite code biases are represented as DSBs, the following two-step approach adapted from Lou et al. (2016) is used (equation 4.9). First, the observations are accommodated to the first reference observable of the IF LC. Second, they are shifted to the IF LC of the reference observables using the IF LC's coefficient and the corresponding DSB. For example, a GPS C1C observation is first accommodated to C1W with the DSB between C1C and C1W, and then shifted to the IF LC with the coefficient 1.5457 and the DSB between C1W and C2W.

4.4. Kalman filter

Kalman filtering is a well-known algorithm for estimating time-dependent and varying parameters. It is named after R. E. Kalman, one of the developers of the underlying theory (Kalman, 1960) and widely used in various fields today. Kalman filtering is typically used in PPP for the parameter estimation due to several convenient characteristics and advantages.

A Kalman filter is suitable for real-time processing and computationally much more efficient than, for example, batch processing in post-processing (Kouba et al., 2017). Contrary to an epoch-wise Least Squares Adjustment, the Kalman Filter takes information about the estimated parameters and their covariance into the next epoch. The stochastic behavior of the parameters over time can be modeled as additional constraints (e.g., ZWD or ionospheric delay). Due to the non-linearity between the parameters in the PPP observation equations an iterative Extended Kalman Filter is used. Detailed information about Kalman Filtering can be found in, for example, Verhagen and Teunissen (2017, chapter 22.5) or Hofmann-Wellenhof et al. (2008, chapter 7.3).

For the Kalman Filter, the observation data (code and phase) are entered into the observation vector l, and the unknown parameters show up in the parameter vector x. The corresponding covariance matrices Q_l and Q_x contain the uncertainties of the observations and parameters, respectively, with the variances in the main diagonal and the covariances outside the main diagonal. In this thesis adjusted variables are denoted with a circumflex (ˆ) and predicted variables with a tilde (˜).

To start the filtering, a priori values for the parameters and the corresponding variances and covariances have to be defined. They are used to establish the parameter vector $\boldsymbol{x_0}$ and its covariance matrix $Q_{x,0}$ in the first epoch of the processing. The process of linearized Kalman filtering can then be divided into three steps performed in each epoch of the processing:

$$G = \tilde{Q}_x \, A^T \, (Q_l + A\tilde{Q}_x A^T)^{-1} \tag{4.10}$$

First, the so-called gain matrix G is computed with equation 4.10 using the covariance matrix of the parameters $Q_{\hat{x}}$, the covariance matrix of the observations Q_l, and the design matrix A containing the functional model (section 4.4.2). The gain matrix describes the gain obtained from the new measurements compared to the prediction of the parameters derived in the previous epochs of the processing.

$$\hat{\boldsymbol{x}} = \tilde{\boldsymbol{x}} + G\,(l - A\tilde{\boldsymbol{x}}) \tag{4.11}$$

$$\hat{Q}_x = (I - GA)\,\tilde{Q}_x \tag{4.12}$$

Second, the adjusted parameters $\hat{\boldsymbol{x}}$ and associated covariance matrix $Q_{\hat{x}}$ are calculated. Therefore, the gain matrix, the predicted parameter vector $\tilde{\boldsymbol{x}}$, and the observation vector l are used in the equations 4.11 and 4.12 .

$$\tilde{\boldsymbol{x}}_{q+1} = T\,\hat{\boldsymbol{x}} \tag{4.13}$$

$$\tilde{Q}_{x,q+1} = T\,\hat{Q}_x\,T^T + N \tag{4.14}$$

In the third and last step, the parameters and their covariance matrix are predicted for the next epoch using the transition matrix T and the system noise matrix N in the equations 4.13 and 4.14. The transition matrix describes the linearized dynamic model of the parameters from one epoch to the next. The system noise matrix N describes the process noise of the dynamic model.

4.4.1. Exclusion of observations

The PPP solution is quite sensitive to outliers and imperfections of the observation model. Therefore, specific observations have to be excluded from the Kalman Filter for various reasons to avoid imperfections and discontinuities in the estimated parameters. Table 4.1 summarizes the applied checks of the observations performed in each epoch of the processing. Apart from these reasons for exclusions, methods for detecting multipath can be considered (section 7.4).

Generally, signals of satellites close to the horizon are more vulnerable to all kinds of error sources (e.g., atmosphere, multipath) and show a more significant variation from the observation model. Therefore, a cutoff angle (e.g., 5°) eliminating satellites extremely close to the horizon is usually introduced in addition to an elevation-based weighting (section

4.4.3).

Furthermore, observations without precise orbit or clock information are eliminated. The same is true for satellites with missing code biases. Note that satellites lacking phase biases need to be excluded only from the ambiguity fixing process. Usually, data gaps or invalid data are seen more often for real-time correction streams than for post-processed satellite products.

Additionally, observations with a low signal-to-noise ratio are eliminated. Since the RINEX format contains a digit to indicate the raw signal strength[26], this value can be used in conjunction with a threshold (e.g., 3). Another option is to use the observation's SNR, typically provided in the RINEX file.

Reason	Detection
Cutoff	Satellite's elevation below, for example, 5°
Missing data	Missing satellite orbits, clocks, or biases
Low SNR	Digit of the raw signal strength in RINEX file under, for example, 3
Cycle slip	Equations 4.15 - 4.17 or RINEX LLI bit is set
Outlier	Check of observed minus computed range (equations 4.18 - 4.20)

Table 4.1: Reasons to exclude observations

Cycle slip detection Undetected cycle slips destroy the assumption of constant phase ambiguities and jeopardize the PPP solution. Therefore, the detection of cycle slips and effective methods for this purpose are essential for a stable PPP solution.

According to the RINEX specifications, the digit after an observation in the RINEX file is reserved for marking a loss of lock of the receiver. This Loss of Lock Indicator (LLI) bit indicates a cycle slip and marked phase measurements are excluded. Furthermore, the difference between subsequent GF LC observations (section 2.4.4) is used for the detection of cycle slips caused by other reasons.

$$dL_i = L_i(q) - L_i(q-1) \tag{4.15}$$

where dL_i denotes the difference between the raw phase measurement of the current epoch $L_i(q)$ and last epoch $L_i(q-1)$ on the frequency i in units of meters. Equation 4.15 is used twice to calculate the GF LC dL_i and dL_j of the phase observations on frequency i and a second frequency j, respectively.

$$dL_{i,j} = |dL_i - dL_j| \tag{4.16}$$

$$dL_{i,j} > \varepsilon_{dL} \tag{4.17}$$

The difference between dL_i and dL_j corresponds to the temporal difference of the GF LC

---

[26] IGS: *The Receiver Independent Exchange Format*. https://www.igs.org/wg/rinex/#documents-formats

and is calculated with equation 4.16. This difference $dL_{i,j}$ is compared with an user-defined threshold ε_{dL} (equation 4.17). If this threshold is exceeded, a cycle slip is flagged. For example, when using the conventional PPP model with GPS, L_i might be the phase observation on the L1 frequency and L_j the phase observation on the L2 frequency.

If a cycle slip is detected, the specific phase observation is eliminated, and the estimated phase ambiguity in the parameter vector is reset. The corresponding code observation is used anyway. Since high-quality geodetic receivers usually offer enough reliable observations and contain only a small amount of cycle slips, no cycle slip repairing is performed in the course of this thesis.

To extend this method to three frequencies, equation 4.15 is used three times to calculate the difference between the first and second frequency $dL_{1,2}$, between the first and third frequency $dL_{1,3}$, and between the second and third frequency $dL_{2,3}$. The inequality 4.17 is used three times to detect the phase measurement with a cycle slip. For example if no cycle slip is detected for $dL_{1,2}$, but for $dL_{1,3}$ and $dL_{2,3}$, a cycle slip is flagged only for the phase observation on the third frequency. Of course, this approach can be extended to any number of frequencies.

This cycle slip detection method requires observations on at least two frequencies, usually the case in PPP. Since this approach relies only on subtractions, it is easy to calculate. Furthermore, this method can be applied already from the second epoch of processing onwards, and a tight threshold (e.g., 5 cm) can be used.

Overall, this method has proven to be very efficient and reliable. Therefore, it should be the preferred way to detect cycle slips during the PPP processing. Alternatives are the difference between phase and code observation and approaches based on Doppler measurements. Both are viable options for SF observations and low-cost receivers' data.

Check of observed minus computed   To detect outliers (e.g., multipath), raPPPid offers the possibility to detect observations significantly deviating from the observation model. This approach increases especially the stability of long-term PPP solutions (e.g., a few hours).

For this purpose, the observed minus computed vector (omc) is calculated for code observations omc_P and phase observations omc_L as the difference between the actual and modeled observations (equations 3.39 and 3.40). Furthermore, the median is subtracted to remove a possible drift of the receiver clock and enable the detection of outliers.

$$\overline{omc}_P = |P_i - P_i^{model}| \tag{4.18}$$

$$omc_P = \overline{omc}_P - median(\overline{omc}_P) \tag{4.19}$$

Since the calculation is the same for code and phase, the equations 4.18 and 4.19 show this process exemplary for the omc values of the code observation omc_P. If one value of omc_P or omc_L exceeds a specific corresponding threshold, the related observation is eliminated. By

default, the used limits are fixed user-defined values.

$$thl_{var} = f_{omc} \cdot \text{std}(omc_n) \tag{4.20}$$

Additionally, it is possible to apply variable thresholds thl_{var} based on the idea that the algorithm adapts the thresholds' size to the observations' quality. Equation 4.20 shows the calculation exemplary. The user has to define a factor f_{omc} and a certain number of epochs n. The variable thresholds are calculated as the standard deviation of all omc values of the last n epochs (omc_n). The resulting value is multiplied by the user-defined factor. The variable limits are computed if already n epochs have been processed and applied only if their value is smaller than the fixed thresholds.

Experience showed that sensible choices for the fixed thresholds are 25 meters and 2 meters for code and phase, respectively. Usually, the algorithm can detect almost all outliers with these values. Too tight limits might randomly eliminate observations.

Furthermore, a factor of 6 and the epochs of the last few minutes are reasonable for the variable thresholds from experience. However, variable thresholds are double-edged since their values get very small for high-quality observations, and suddenly completely unsuspicious observations are eliminated. Therefore, variable thresholds should be used only for observation data containing a noticeable amount of outliers.

Extensive tests have shown that the observed minus computed check is crucial to obtain a stable PPP solution for extended time periods of several hours and to avoid outliers or jumps in the estimated parameters (e.g., coordinates) leading to a new convergence period. On the other hand, its effect on the convergence performance is insignificant because the filter is more flexible at this stage, compensating for outliers. Furthermore, the likelihood of suspicious observations is not that high in this short period.

4.4.2. Functional model

An essential issue for Kalman filtering and, generally, any parameter estimation method is to establish a functional model by means of the design matrix A. A describes the linearized relation between the observation equations and the parameters. The functional model of the conventional and uncombined PPP model is specified in this section for n satellites and any number of GNSS ($GNSS_1$, $GNSS_2$,...). In the following, the subscript indicates the frequency and the superscript the satellite or GNSS. The uncombined model is developed for three frequencies, but the provided equations can be extended to any number of frequencies.

$$
x_{IF} = \begin{bmatrix} x \\ y \\ z \\ zwd \\ dt_R^{GNSS_1} \\ \delta t_R^{GNSS_2} \\ \vdots \\ N_1^1 \\ N_2^1 \\ \vdots \\ N_3^n \end{bmatrix}
\qquad
x_{UC} = \begin{bmatrix} x \\ y \\ z \\ zwd \\ dt_R^{GNSS_1} \\ DCB_{12}^{GNSS_1} \\ DCB_{13}^{GNSS_1} \\ \delta t_R^{GNSS_2} \\ DCB_{12}^{GNSS_2} \\ DCB_{13}^{GNSS_2} \\ \vdots \\ N_1^1 \\ N_2^1 \\ \vdots \\ N_3^n \\ dIon^1 \\ dIon^2 \\ \vdots \\ dIon^n \end{bmatrix}
\qquad (4.21)
$$

The parameter vectors of the conventional model x_{IF} and the uncombined model x_{UC} are presented in equation 4.21. They contain the estimated parameters: The receiver's coordinates x, y, and z, the (residual) zenith wet tropospheric delay zwd, the receiver clock error dt_R, the receiver clock offset(s) δt_R (in the case of multiple processed GNSS), and the phase ambiguities N. Furthermore, the parameter vector of the uncombined model contains the

slant ionospheric delay on the first frequency $dIon$ for each satellite and the receiver DCBs between the first and each other processed frequency for each processed GNSS. If a specific parameter is modeled instead of estimated (e.g., receiver DCBs) it can be removed from the parameter vector.

$$l = \begin{bmatrix} P_1^1 & L_1^1 & P_1^2 & L_1^2 & \dots & L_1^n & P_2^1 & L_2^1 & \dots & L_3^n \end{bmatrix}^T \tag{4.22}$$

The code and phase observations alternate and are ordered by frequency and satellite in the observation vector. Equation 4.22 presents the observation vector for code and phase observations on three frequencies. For the conventional model, this vector simplifies to just the observations of the IF LC. In the following, several blocks of the design matrix are introduced to eventually build the complete design matrix.

$$A_{xyz,trop} = \begin{bmatrix} \frac{\partial P_1^1}{\partial x} & \frac{\partial P_1^1}{\partial y} & \frac{\partial P_1^1}{\partial z} & \frac{\partial P_1^1}{\partial tropo} \\ \frac{\partial L_1^1}{\partial x} & \frac{\partial L_1^1}{\partial y} & \frac{\partial L_1^1}{\partial z} & \frac{\partial L_1^1}{\partial tropo} \\ \vdots & \vdots & \vdots & \vdots \\ \frac{\partial L_3^n}{\partial x} & \frac{\partial L_3^n}{\partial y} & \frac{\partial L_3^n}{\partial z} & \frac{\partial L_3^n}{\partial tropo} \end{bmatrix} = \begin{bmatrix} \frac{x-X_1}{\rho} & \frac{y-Y_1}{\rho} & \frac{x-Z_1}{\rho} & wmf_1 \\ \frac{x-X_1}{\rho} & \frac{y-Y_1}{\rho} & \frac{z-Z_1}{\rho} & wmf_1 \\ \vdots & \vdots & \vdots & \vdots \\ \frac{z-Z_n}{\rho} & \frac{y-Y_n}{\rho} & \frac{z-Z_n}{\rho} & wmf_n \end{bmatrix} \tag{4.23}$$

$$A_{dt}^{GNSS_1} = \begin{bmatrix} \frac{\partial P_1^1}{\partial dt_R^{GNSS_1}} \\ \frac{\partial L_1^1}{\partial dt_R^{GNSS_1}} \\ \vdots \\ \frac{\partial L_3^n}{\partial dt_R^{GNSS_1}} \end{bmatrix} = I_{n,1} \quad \text{and} \quad A_{\delta t}^{GNSS} = \begin{bmatrix} \frac{\partial P_1^1}{\partial \delta t_R^{GNSS}} \\ \frac{\partial L_1^1}{\partial \delta t_R^{GNSS}} \\ \vdots \\ \frac{\partial L_3^n}{\partial \delta t_R^{GNSS}} \end{bmatrix} = \begin{bmatrix} 0 \\ 0 \\ \vdots \\ 1 \\ 1 \\ \vdots \end{bmatrix} \tag{4.24}$$

$$A_{DCB}^{GNSS} = \begin{bmatrix} \frac{\partial P_1^1}{\partial DCB_{12}^{GNSS}} & \frac{\partial P_1^1}{\partial DCB_{13}^{GNSS}} \\ \frac{\partial L_1^1}{\partial DCB_{12}^{GNSS}} & \frac{\partial L_1^1}{\partial DCB_{13}^{GNSS}} \\ \vdots & \vdots \\ \frac{\partial L_3^n}{\partial DCB_{12}^{GNSS}} & \frac{\partial L_3^n}{\partial DCB_{13}^{GNSS}} \end{bmatrix} = \begin{bmatrix} \vdots & \vdots \\ -1 & 0 \\ -1 & 0 \\ \vdots & \vdots \\ 0 & -1 \\ 0 & -1 \\ \vdots & \vdots \end{bmatrix} \tag{4.25}$$

$$
A_N = \begin{bmatrix}
\frac{\partial P_1^1}{\partial N_1^1} & \frac{\partial P_1^1}{\partial N_1^2} & \frac{\partial P_1^1}{\partial N_1^3} & \cdots & \frac{\partial P_1^1}{\partial N_3^n} \\[2mm]
\frac{\partial L_1^1}{\partial N_1^1} & \frac{\partial L_1^1}{\partial N_1^2} & \frac{\partial L_1^1}{\partial N_1^3} & \cdots & \frac{\partial L_1^1}{\partial N_3^n} \\[2mm]
\vdots & \vdots & \vdots & \ddots & \vdots \\[2mm]
\frac{\partial P_3^n}{\partial N_1^1} & \frac{\partial P_3^n}{\partial N_1^2} & \frac{\partial P_3^n}{\partial N_1^3} & \cdots & \frac{\partial P_3^n}{\partial N_3^n} \\[2mm]
\frac{\partial L_3^n}{\partial N_1^1} & \frac{\partial L_3^n}{\partial N_1^2} & \frac{\partial L_3^n}{\partial N_1^3} & \cdots & \frac{\partial L_3^n}{\partial N_3^n}
\end{bmatrix}
= \begin{bmatrix}
0 & 0 & 0 & \cdots & 0 \\
1 & 0 & 0 & \cdots & 0 \\
\vdots & \vdots & \vdots & \ddots & \vdots \\
0 & 0 & 0 & \cdots & 0 \\
0 & 0 & 0 & \cdots & 1
\end{bmatrix}
\tag{4.26}
$$

$$
A_{iono} = \begin{bmatrix}
\frac{\partial P_1^1}{\partial dIon^1} & \frac{\partial P_1^1}{\partial dIon^2} & \frac{\partial P_1^1}{\partial dIon^3} & \cdots & \frac{\partial P_1^1}{\partial dIon^n} \\[2mm]
\frac{\partial L_1^1}{\partial dIon^1} & \frac{\partial L_1^1}{\partial dIon^2} & \frac{\partial L_1^1}{\partial dIon^3} & \cdots & \frac{\partial L_1^1}{\partial dIon^n} \\[2mm]
\vdots & \vdots & \vdots & \ddots & \vdots \\[2mm]
\frac{\partial P_3^n}{\partial dIon^1} & \frac{\partial P_3^n}{\partial dIon^2} & \frac{\partial P_3^n}{\partial dIon^3} & \cdots & \frac{\partial P_3^n}{\partial dIon^n} \\[2mm]
\frac{\partial L_3^n}{\partial dIon^1} & \frac{\partial L_3^n}{\partial dIon^2} & \frac{\partial L_3^n}{\partial dIon^3} & \cdots & \frac{\partial L_3^n}{\partial dIon^n}
\end{bmatrix}
= \begin{bmatrix}
1 & 0 & 0 & \cdots & 0 \\
-1 & 0 & 0 & \cdots & 0 \\
\vdots & \vdots & \vdots & \ddots & \vdots \\
0 & 0 & 0 & \cdots & \gamma_{13} \\
0 & 0 & 0 & \cdots & -\gamma_{13}
\end{bmatrix}
\tag{4.27}
$$

Equation 4.23 describes the part of the design matrix covering the user's position and the estimation of the wet part of the tropospheric delay. For the partial derivatives in the first three columns the satellites' coordinates X, Y, and Z are used. Furthermore, wmf denotes the wet mapping function of the tropospheric delay (equation 3.25).

Keep in mind that the receiver clock error is estimated for the first processed GNSS (typically GPS, the order is presented in table 2.2). The corresponding block of the design matrix is shown in the left part of equation 4.24 and corresponds to an all-ones column vector with n rows. This is because all observations contains the estimated receiver clock error.

Additionally, a receiver clock offset is estimated for each additional processed GNSS and the right part of equation 4.24 shows the corresponding block of the design matrix. Thereby, the position of rows containing -1 depends on the number of satellites for each GNSS in the current epoch. The same applies to equation 4.25.

Due to the dispersivity of the ionosphere, the ratio of the squared frequencies (equation 2.17) occurs in the corresponding part of the design matrix (equation 4.27).

$$
A_{IF} = \begin{bmatrix} A_{xyz,trop} & A_{dt}^{GNSS_1} & A_{\delta t}^{GNSS_2} & \ldots & A_N \end{bmatrix}
\tag{4.28}
$$

$$
A_{UC} = \begin{bmatrix} A_{xyz,trop} & A_{dt}^{GNSS_1} & A_{DCB}^{GNSS_1} & A_{\delta t}^{GNSS_2} & A_{DCB}^{GNSS_2} & \ldots & A_N & A_{iono} \end{bmatrix}
\tag{4.29}
$$

By combining diverse blocks, the complete design matrix is built for the conventional and

uncombined model with equations 4.28 and 4.29, respectively.

$$A_{pseudo} = \begin{bmatrix} 0_{n,\,m+3n} & I_{n,n} \end{bmatrix} \tag{4.30}$$

$$A_{UC,constraint} = \begin{bmatrix} A_{UC} \\ A_{pseudo} \end{bmatrix} \tag{4.31}$$

To obtain the uncombined model with ionospheric constraint, the modeled ionospheric delays for each satellite are appended as ionospheric pseudo-observations to the observation vector presented in equation 4.22. Furthermore, the design matrix is extended with a block for the ionospheric pseudo-observations A_{pseudo} to create the complete design matrix of the uncombined model with ionospheric constraint $A_{UC,constraint}$ (equations 4.30 and 4.31).

In equation 4.30, a zero matrix with n rows (one ionospheric pseudo-observation for each satellite) and $m + 3n$ columns is utilized. m denotes the number of estimated parameters and equals, for example, 16 when processing all 4 GNSS (3 coordinates, ZWD, receiver clock error, 3 receiver clock offsets, 8 DCBs). $3n$ is the number of estimated ambiguities when processing three frequencies because one ambiguity is estimated for all satellites on each frequency.

Redundancy   Each parameter estimated during the calculation of the PPP solution results in a specific number of unknowns shown in table 4.2. This number can be either a fixed value (e.g., three in the case of the receiver coordinates) or a function of the number of satellites n, GNSS g, and frequencies f. Note that the number of estimated float ambiguities only depends on the number of satellites using the conventional model. In contrast, it also hinges on the number of frequencies in the uncombined model. Furthermore, receiver DCBs and ionospheric delays are only estimated in the uncombined model.

Parameter	Unknowns	Model
Receiver coordinates	3	IF, UC
Zenith Wet Delay	1	IF, UC
Receiver clock error and offsets	g	IF, UC
Float ambiguities	n	IF
Float ambiguities	nf	UC
Receiver DCBs	$(f-1)g$	UC
Ionospheric delays	n	UC

Table 4.2: The number of unknowns for each estimated parameter using the conventional (IF) or uncombined (UC) model

Subsequently, table 4.3 shows the number of observations, number of parameters, and the resulting redundancy for the conventional and uncombined model (with ionospheric constraint). It is evident from table 4.3 that the uncombined model has a higher number of parameters, taking, for example, two frequencies. This is compensated with an even

higher number of observations, especially in the case of the uncombined model with ionospheric constraint. Obviously, this leads to a higher computational effort. While the redundancy of the conventional and uncombined model is similar, the uncombined model with ionospheric constraint has a considerably higher redundancy thanks to the introduced ionospheric pseudo-observations.

PPP model	**Conventional Model**	**Uncombined Model**	**...with ionospheric constraint**
Observations	$2n$	$2nf$	$2nf + n$
Parameters	$4 + g + n$	$4 + fg + fn + n$	
Redundancy	$n - 4 - g$	$nf - 4 - fg - n$	$nf - 4 - fg$

Table 4.3: The number of observations, number of parameters, and resulting redundancy for the conventional and uncombined model (with ionospheric constraint)

Since the difference in redundancy between the conventional and the uncombined model with ionospheric constraint increases with a growing number of satellites, one can argue that the uncombined model with ionospheric constraints benefits much more from additional satellites. Therefore, this approach seems to be the best choice in the evolving multi-GNSS and multi-frequency landscape in this regard.

4.4.3. Stochastic model

To achieve optimal results with Kalman filtering reasonable values for the precision of the observations are required to build the covariance matrix of the observations Q_l. Furthermore, the parameter's stochastic settings have to be adapted to the case of a specific application considering, for example, the receiver-clock characteristic and atmospheric activity. In the following a reasonable stochastic model for multi-frequency PPP with static receivers is presented.

Code and phase observations   In the case of geodetic receivers, sensible values for the standard deviation of the raw measurements are a few decimeters for the code (e.g., 30 cm) and few millimeters (e.g., 2 mm) for the phase. These values are used in the same way for all GNSS and it is assumed that the raw measurements are uncorrelated. So, no weighting for observation's GNSS or frequency is applied. If a LC is built (e.g., conventional model), the standard deviation of the raw observations is increased through the coefficients of the LC. This is considered according to the formulas provided in L. Pan et al. (2019) improving the results in particular for multi-GNSS processing due to different coefficients of IF LCs from varying GNSS.

Usually, an elevation based weighting scheme is applied in raPPPid. Therefore, the function $sin^2(elevation)$ is used to scale the aforementioned values. Satellites close to the horizon are weighted less than satellites near the zenith, and the observations' standard devia-
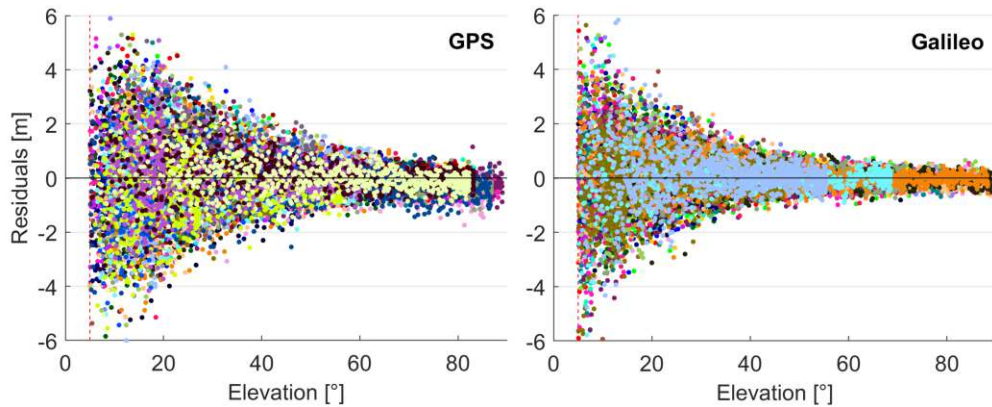
Figure 4.1: Code residuals over elevation for GPS (left) and Galileo (right) of the IGS station ULAB on January 12, 2020. The residuals are color-coded according to the satellite.

tion is manipulated accordingly. This is based on the fact that the observations' residuals of geodetic receivers are typically correlated with the elevation angle (figure 4.1). Alternatives are a weighting scheme based on the MP LC as proposed by Seepersad and Bisnath (2015) or the SNR leading usually to better results, for example, for low-cost receivers.

Ionospheric pseudo-observations   A crucial point when using ionospheric pseudo-observations is their weighting in the Kalman filter which directly influences the coordinate convergence time (Aggrey and Bisnath, 2019). Weighted too high, the ionospheric pseudo-observations will drag the estimated ionospheric delay too much to the ionosphere model's imperfection ('over constraining'). Also, too low weights ('under constraining') will degrade convergence. Therefore, the standard deviation of the ionospheric pseudo-observations has to be chosen according to the ionospheric model's quality.
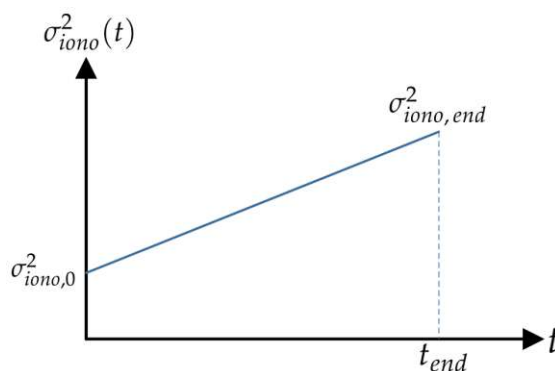
Figure 4.2: The linear approach increasing the variance of the ionospheric pseudo-observations over time

Using ionospheric pseudo-observations with a constant standard deviation in all epochs as described in Zhou et al. (2018) has not proven to be optimal due to the propagation of time-

correlated errors (Aggrey and Bisnath, 2019). Following Cai et al. (2017) and the results of Ning et al. (2019), where a time-varying weighting scheme has proven its advantage over other approaches, a linear approach is used to decrease the ionospheric constraint's strength over time (figure 4.2). Additionally, no ionospheric pseudo-observations are used after a specific processing time t_{end}. The variance of the ionospheric pseudo-observations σ^2_{iono} increases over time according to the following linear function:

$$\sigma^2_{iono}(t) = \sigma^2_{iono,0} + \frac{\sigma^2_{iono,end} - \sigma^2_{iono,0}}{t_{end}} \cdot t \quad (4.32)$$

where t is the time since the start of the solution. At the initial epoch of the solution the variance $\sigma^2_{iono,0}$ is used for the ionospheric pseudo-observations, which is altered towards the variance $\sigma^2_{iono,end}$ at t_{end}. Therefore, the parameters $\sigma^2_{iono,0}$, t_{end}, and $\sigma^2_{iono,end}$ define the strength of the ionospheric constraint and how fast it is released. Alternatively, T. Liu et al. (2018) adapts the variances of the ionospheric constraint according to the residuals.

Experience has shown that a standard deviation in the size of a few decimeters (e.g., 15-30 cm) is a sensible choice for ionospheric pseudo-observations of highly accurate ionosphere models, which is about code measurement's precision. This initial standard deviation should be raised, for example, to a few meters (e.g., 3-5 m) after 10 minutes when processing observations with an interval of 30 s. For high-rate observations with an observation interval of 1 second, the period of using an ionospheric constraint can be reduced to under a minute (e.g., a few tens of seconds). Note that the elevation-based weighting is also applied on the variance of the ionospheric pseudo-observations resulting from equation 4.32 to ensure consistency with the code and phase observations. Therefore, the given values for the standard deviation of the ionospheric pseudo-observations correspond to the zenith direction.

Parameters   Table 4.4 presents suitable values for the initial standard deviation and system noise of the parameters for static PPP. These values are used for building the initial covariance matrix of the parameters $Q_{x,0}$ and the system noise matrix N. Since usually all estimated parameters directly serve as a prediction for the next epoch in the static case of PPP, the transition matrix T simplifies to the identity matrix.

Generally, to keep the carrier phase ambiguity constant over time and exploit the phase measurement precision, the ambiguity's process noise is set to zero in PPP. In the case of static positioning, also the coordinate's process noise is zero. The value given for the coordinates' initial standard deviation in table 4.4 assumes that no or only very rough apriori coordinates are known. Otherwise, a smaller value can be used.

Since the behavior of the receiver clock error and offsets is usually unknown and unpredictable (figure 3.11), no constraint is set up for these parameters. The same is true for the receiver DCBs.

According to Kouba (2015) the tropospheric zenith path delay will vary in time by a rel-

Parameter	Initial Standard Deviation $[m]$	System Noise $[\frac{m}{\sqrt{hour}}]$
Coordinates	10 000	0
Residual ZWD	0.10	0.002 - 0.005
Receiver Clock Error	30 000	300
Receiver Clock Offset	30	5
Receiver DCBs	10	0
Float Ambiguities	2	0
Ionospheric Delay	1 - 2	0.5 - 2

Table 4.4: Sensible stochastic settings for the Kalman Filter in case of static PPP

atively small amount, in the order of a few cm/hour. Therefore, the ZWD can be estimated as a random walk process that varies only slowly with time, and usually, a system noise of 2-5 $\frac{mm}{\sqrt{hour}}$ is applied. Since the residual ZWD is estimated and high-quality troposphere models are usually applied for PPP, an initial standard deviation of 10 cm is a reasonable choice.

For the estimation of the ionospheric delay, an initial standard deviation of 1-2 m and a system noise of 0.5-2 $\frac{m}{\sqrt{hour}}$ have proven as sensible values during testing.

5. PPP with integer ambiguity resolution

Integer ambiguity resolution is the key to reduce the convergence time significantly and achieve the highest accuracy with PPP. Unfortunately, it is not straightforward to fix the ambiguities to their correct integer value in PPP. Undifferenced ambiguities absorb hardware phase biases originating from the receiver and satellite, destroying their integer nature (Håkansson et al., 2017; J. Shi and Gao, 2014).

However, based on the float solution, there are methods to fix the undifferenced phase ambiguities to their correct integer values and calculate a fixed coordinate solution. In addition, the user must consistently apply suitable satellite phase biases to correct satellite hardware delays. Apart from that, receiver hardware delays are eliminated with a reference satellite. In that way, PPP with integer ambiguity resolution (PPP-AR) has proven itself an effective way to improve the performance of PPP, especially in the east coordinate component (Ge et al., 2008; Kouba et al., 2017).

Over the years, the performance of PPP-AR has improved considerably, reducing the convergence time from 20 - 30 minutes for a GPS-only solution (Huber, 2015) down to a few minutes or less. Generally, multi-GNSS solutions outperform, for example, GPS-only solutions. Despite new approaches (Teunissen and Khodabandeh, 2019), fixing GLONASS ambiguities in PPP is still considered problematic. The reason for this are frequency and receiver type-specific inter-frequency biases in the GLONASS observations caused by the FDMA technique employed from the GLONASS signals (Reussner and Wanninger, 2011). Furthermore, fixing BeiDou ambiguities is challenging due to specific error sources (e.g., GDVs in case of BeiDou-2). However, GLONASS and BeiDou observations can be used at least in the float solution to fasten the float ambiguities' convergence and strengthen the fixing of GPS and Galileo ambiguities.

The float solution requires an extended convergence period to achieve its final accuracy and estimate the unknown parameters reliably. This convergence period can be described as the time the solution transitions from a pseudorange to a float ambiguity carrier phase solution (Choy et al., 2017). Similarly, some epochs with a valid float solution are required for the float ambiguities to converge and ensure correct integer fixing. Therefore, the fixing process usually does not start in the first epoch to increase the chance of fixing the ambiguities to their correct integer value.

The top part of figure 5.1 shows the float (left side) and fixed (right side) coordinates of the IGS station KIRU in Kiruna (Sweden) on January 1st, 2020, 19:00 h using the conventional PPP model and two GPS and Galileo frequencies in the processing. The fixing process starts after 30 seconds. Due to the rapid convergence of the float ambiguities (middle part of figure 5.1), the ambiguity fixing is instantaneously successful after the start of the fixing procedure. This is shown in the bottom part of the figure. Thereby, blue sections represent periods of satellites with fixed ambiguity, light yellow sections illustrate periods where the satellite is not visible, and grey sections depict periods where a satellite is under the cutoff angle of 5°.
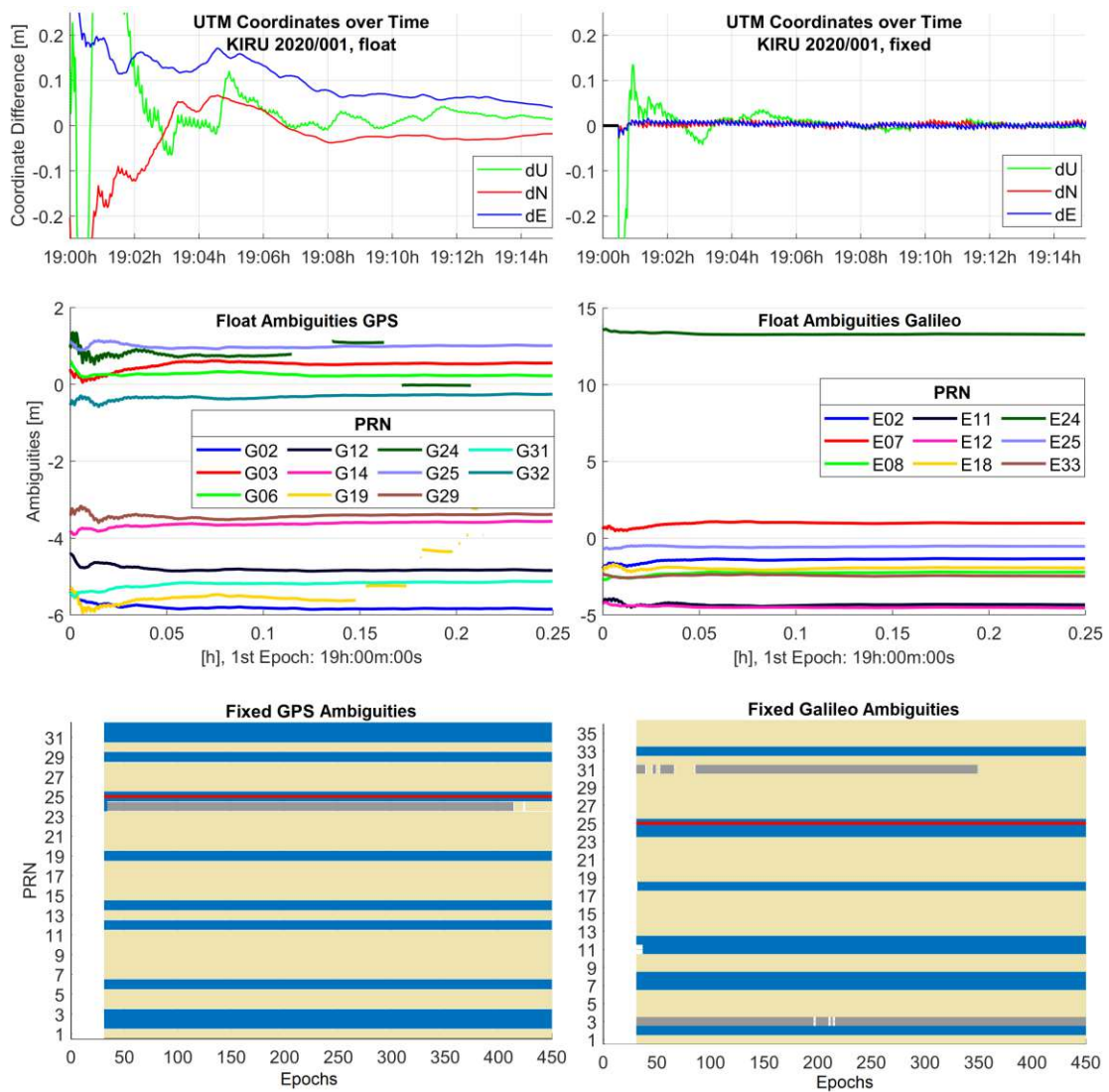
Figure 5.1: The float coordinates (top left), fixed coordinates (top right), estimated float ambiguities for GPS (middle left) and Galileo (middle right), and fixed ambiguities for GPS (bottom left) and Galileo (bottom right) of the IGS station KIRU (observation interval 1 s) on 1st January 2020, 19:00-19:15 h using CODE MGEX products.

Furthermore, a red line indicates the chosen reference satellites. This rapid and successful fixing results in much faster convergence and higher accuracy of the fixed coordinates in the shown time period. This example shows that it is possible to reduce the convergence time with PPP-AR based on the fact that the float ambiguities usually converge much faster than the float coordinates.

The following sections describe the fixing procedure for the conventional and uncombined model.

5.1. Reference satellite

The float ambiguity contains phase hardware delays originating from the receiver and satellite (equations 4.3 and 4.6). A reference satellite is used and selected for each GNSS to eliminate the receiver hardware delays in the undifferenced ambiguities. Due to inter-system biases, choosing a single reference satellite in a multi-GNSS solution is not possible.

The reference satellite is used to build satellite single differences by subtracting the observations from the reference satellite's observations. Equation 5.1 shows, for example, the calculation of the single-differenced (SD) ambiguity for an arbitrary satellite using the reference satellite's ambiguity N^{refsat}.

$$N_{SD}^{sat} = N^{refsat} - N^{sat} \tag{5.1}$$

The resulting SD observations or ambiguities inevitably contain propagated imperfections of the reference satellite. Consequently, it is essential to find reliable reference satellites, and various selection criteria have been tested.

Eventually, satellites close to the zenith have proven as a safe choice. Therefore, the satellite with the minimum zenith distance is selected for each GNSS as the reference satellite at the beginning of the fixing process. Furthermore, when processing three frequencies in the uncombined model (section 5.3), 3-frequency GPS satellites are preferred to simplify the fixing process and to build SD on the L5 frequency.

The chosen reference satellite is kept until its elevation angle drops under a specific value (e.g., 20°) or an irregularity occurs (e.g., cycle slip). In that case, again, the satellite with the maximum elevation angle is chosen as the new reference satellite. During this study, alternatives based on more sophisticated selection criteria (e.g., the standard deviation of the MW LC) have been tested but did not prove to enhance the fixed solution's performance.

5.2. Conventional PPP-AR

Usually, the ambiguity of the IF LC is decomposed into the ambiguities of the WL and a NL LC. These are fixed consecutively to rebuild the IF LC's ambiguity and to calculate a fixed coordinate solution. Figure 5.2 illustrates this process. Principally, two strategies differentiating how the satellite hardware delays are isolated from the integer ambiguities build
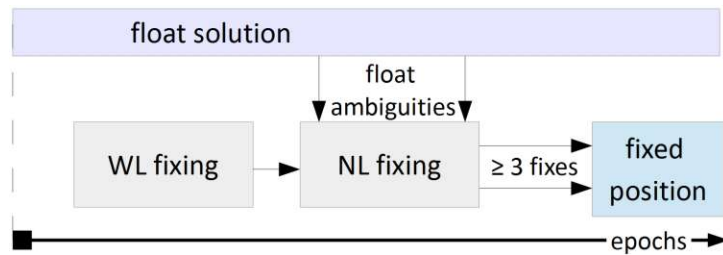
Figure 5.2: Procedure of calculating a fixed position with the conventional model

the basis for PPP-AR with the conventional model. The PPP user has to apply the resulting satellite biases provided from the network side consistently.

First, Ge et al. (2008) developed a method to determine uncalibrated phase delays (UPDs) for the WL and NL ambiguity by averaging the fractional parts of the float WL and NL estimates in a network solution. Nowadays, UPDs are more likely called fractional cycle biases (FCBs). Forwarded to the user, the WL and NL FCBs allow fixing the between satellites SD ambiguities.

Second, it is possible to estimate so-called integer clocks termed the integer recovery clock (IRC) method. Contrary to Ge et al. (2008), this strategy assimilates the NL FCBs into the satellite clock estimates. For this reason, the NL ambiguities have to be fixed to integers before estimating the satellite clocks in the network solution. Laurichesse et al. (2009) also used the decomposition into WL and NL, but the undifferenced ambiguities are directly fixed to an integer. The PPP user has then only to consider the WL FCBs in the fixing procedure. Similarly, Collins et al. (2010) developed the decoupled clock model where the pseudorange clocks differ from the carrier-phase clocks.

Geng et al. (2010) and J. Shi and Gao (2014) compared these two methods and stated their equivalence for the ambiguity-fixed position. Teunissen and Khodabandeh (2015) looked into more detail, reviewed in total six strategies enabling PPP-AR, and discussed their network and user component. They show how these are connected and provide transformations in between them.

Nowadays, various institutions and ACs provide satellite products (section 3.1.2) enabling conventional PPP-AR using the two presented approaches (Glaner and Weber, 2021). The MGEX orbit and clock product of CNES applies the Integer Recovery Clock (IRC) method allowing PPP-AR for GPS and Galileo. The WL biases are provided in the header of the clock file. Note that CNES does not manage to fix all satellites every day indicated by a file on their server[27]. Furthermore, the MGEX product of CODE enables PPP-AR for GPS and Galileo based on the IRC method providing OSBs in a separate file. Also, the satellite products of TUG include OSBs allowing PPP-AR. Contrary to other institutions, SGG does not compute satellite orbits or clocks but provides GPS, Galileo, BeiDou, and even QZSS FCBs for several

---

[27] CNES: *Unfixed Satellites*. ftp://ftpsedr.cls.fr/pub/igsac/GRG_ELIMSAT_all.dat

AC's orbit and clock products (e.g., CNES, CODE, and GFZ). Based on the decoupled clock model, the Wuhan University provides clock files and biases for the final orbits of CODE, enabling PPP-AR for GPS (Geng et al., 2019b). PPP-AR in real-time is, for example, possible with the correction streams of CNES. An archive of these correction streams is available on the PPP-WIZARD website[28].

Up to the present day, no IGS product enabling PPP-AR and combining the satellite products of various ACs exists. Seepersad and Bisnath (2017) assessed the interoperability of various satellite products enabling PPP-AR with different approaches and highlighted some challenges (e.g., satellite antenna convention). Banville et al. (2020) showed that for GPS a combination of multiple PPP-AR satellite products and the production of a combined IGS product is possible. Undoubtedly, it is only a question of time until the IGS produces a combined satellite product enabling PPP-AR for multiple GNSS on a regular basis.

5.2.1. WL fixing

The fixing procedure of the conventional PPP model starts with fixing the WL ambiguity. This process is based on the HMW LC (section 2.4.5) built with equation 2.27.

$$HMW^{sat} = (\overline{WL} + b_{WL,R} - b_{WL}^S) \tag{5.2}$$

The HMW LC eliminates all terms except the WL LC's integer ambiguity $\overline{WL}$ and hardware delays originating from the receiver $b_{WL,R}$ and satellite b_{WL}^S (equation 5.2).

$$HMW_{SD} = HMW^{refsat} - HMW^{sat} \tag{5.3}$$

$$\overline{WL}_{SD} = \langle HMW_{SD} + b_{WL,SD}^S \rangle_n \tag{5.4}$$

To eliminate the receiver's hardware delays, the SD HMW LC is calculated with equation 5.3 using the HMW observation of the reference satellite HMW_{sat}^{ref}. Furthermore, satellite hardware delays have to be corrected with the SD WL FCBs $b_{WL,SD}^S$ in equation 5.4.

In that way, the phase hardware delays originating from the receiver and the satellite are eliminated. Therefore, the SD WL ambiguity can be fixed by averaging the SD HMW over the last n epochs (e.g., the last five minutes) and rounding to the nearest integer value denoted as $\langle \ \rangle_n$ in equation 5.4.

Figure 5.3 presents a snippet of the SD HMW observation for the EPOSA station GROA on January 12, 2018. Although the HMW LC is driven by the noise of the code measurement, nearly all values lie inside the threshold of 0.25 cycles used to approve an integer fix. Therefore, the WL ambiguity can usually be fixed reliably by averaging a small number of observation epochs due to the large wavelength (Huber, 2015).

---

[28] PPP-WIZARD: http://www.ppp-wizard.net/
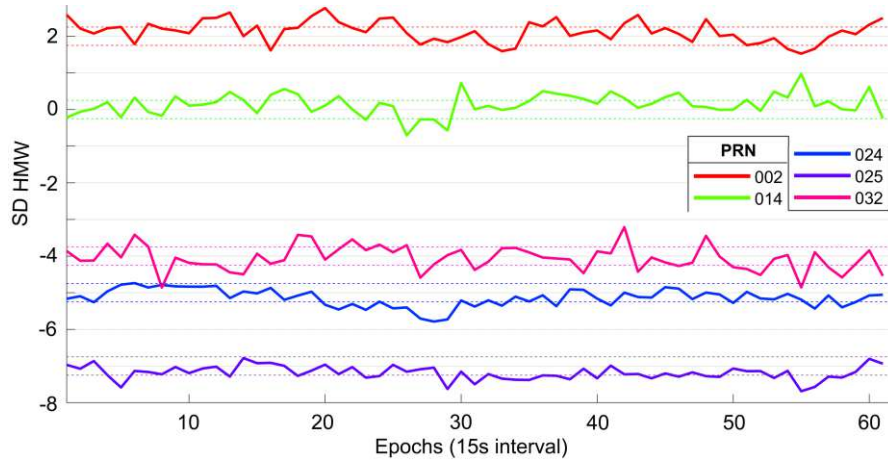
Figure 5.3: Example of the SD HMW observation of the EPOSA station GROA for 5 GPS satel-
lites on January 12, 2018. The dashed lines represent the threshold of 0.25 cycles
used for approving an integer fix.

5.2.2. NL fixing

After the WL ambiguity is fixed successfully, the NL fixing is performed.

$$N_{SD} = N^{refsat} - N \tag{5.5}$$

$$NL_{SD} = N_{SD} \frac{f_1 + f_2}{\lambda_1 f_1} - \overline{WL}_{SD} \frac{f_2}{f_1 - f_2} + b_{NL,SD}^S \tag{5.6}$$

$$\overline{NL}_{SD} = \text{LAMBDA}(NL_{SD}, Q_{NL,SD}) \tag{5.7}$$

First, the float ambiguity is single differenced using the reference satellite's float ambiguity
N_{sat}^{ref} (equation 5.5). Then the SD float NL ambiguity NL_{SD} is calculated with equation 5.6
applying the SD NL FCBs $b_{NL,SD}^S$. Finally, the SD NL ambiguities are fixed for all satellites col-
lectively using the LAMBDA algorithm and partial ambiguity resolution (Teunissen, 1995).
For this purpose, the covariance matrix $Q_{NL,SD}$ of NL_{SD} calculated from the float solution's
covariance matrix using error propagation is applied.

5.2.3. Fixed position

If the SD WL and NL ambiguities are fixed for a specific satellite, equation 5.8 allows to
calculate the fixed SD ambiguity of the IF LC $\overline{N}_{IF,SD}$. As soon as three or more ambiguities
can be constructed in this way, the fixed coordinates are estimated in a separate Least Squares
Adjustment.

$$\overline{N}_{IF,SD}\, \lambda_{IF} = \lambda_1 \frac{f_1 f_2}{f_1^2 - f_2^2} \overline{WL}_{SD} + \lambda_1 \frac{f_1}{f_1 + f_2} (\overline{NL}_{SD} - b_{NL,SD}^S) \tag{5.8}$$

These calculated fixed ambiguities $\overline{N}_{IF,SD}$ are introduced as pseudo-observations with very high weights (e.g., factor 1000) by extending the design matrix of the float solution. Since the float solution relies on undifferenced ambiguities whereas the fixed ambiguities are SD, adding the fixed ambiguities in the form of pseudo-observations avoids more complex modifications of the design matrix. However, the design matrix is reduced to remove the receiver clock error, receiver clock offset(s), and residual zenith wet delay from the adjustment. The float estimates of these parameters are used to correct the undifferenced observations.

Discussion Recapitulating the conventional PPP model's fixing procedure, it gets clear that the WL fixing is independent of the float solution. Similarly, the fixed solution does not influence the float solution at all. On the other hand, the float ambiguities directly contribute to the NL fixing. The Least Squares Adjustment used for the calculation of the fixed position is completely independent from the Kalman Filter of the float solution. Therefore, the coordinates can jump to the correct values as soon as enough ambiguities are fixed.

Note that the WL FCBs are only used for resolving the WL ambiguities. The NL FCBs, on the other hand, directly contribute to the ambiguity-fixed PPP solution in the rebuilding process of the IF LC's ambiguity (equation 5.8). Therefore, the quality of the NL FCBs has a significant effect on the PPP-AR solution (Z. Pan et al., 2017). For satellite products relying on the IRC approach, no NL FCBs have to be applied since these biases are assimilated in the satellite clock product. In this case, the quality of the clock estimation affects the PPP-AR solution.

5.3. Uncombined PPP-AR

As with conventional PPP-AR, suitable satellite products are required for fixing the ambiguities in the uncombined model. Currently, only two institutions (CNES and TUG) compute satellite products recovering the integer property of the raw ambiguities on the satellite side (section 3.1). These satellite products allow fixing the ambiguities of the raw observations and, consequently, any LC. CNES provides RT correction streams applied on the broadcast message and post-processed biases used together with the rapid orbits and clocks of GFZ. The satellite products from TUG are available as a repro3 product and calculated with a raw observation approach (Strasser, 2022; Strasser et al., 2018).

Most of the currently available satellite products are computed with two frequencies and the IF LC. Therefore, the satellite clocks contain a combination of the IF LC's biases used for computation, and no biases for the third frequency are provided. Furthermore, satellite clocks differ when computed with different IF LCs (e.g., GPS L1/L2 or L1/L5) due to the contained combination of the signal's biases. The so-called inter-frequency clock bias (IFCB) is the difference between the satellite clock products computed with, for example, the IF LC built from GPS L1/L2 and L1/L5. The IFCB can reach up to 1-2 decimetres and shows periodic behavior with thermal origin (Montenbruck et al., 2012). P. Li et al. (2020) investigate

the IFCB of GPS, Galileo, and BeiDou. They show that the IFCB is most pronounced for GPS with the following peak to peak amplitudes: GPS up to 1-2 dm, BeiDou 2-3 cm, and Galileo less than 1 cm with over 99 percent smaller than 2 mm. Therefore, Galileo observations are almost not impacted by the IFCB.

Generally, the IFCB severely affects triple-frequency PPP-AR. Usually, biases (e.g., FCBs for EWL, WL, and NL) are estimated in addition to the satellite products based on the IF LC to enable PPP-AR with three frequencies (Gu et al., 2015; X. Li et al., 2021). Alternatively, P. Li et al. (2020) estimate the IFCBs directly.

In the following, an approach for fixing the ambiguities in the uncombined model is introduced for the processing of two and three frequencies. The presented method relies on satellite products recovering the integer property of the raw ambiguities on the satellite side, like those from CNES and TUG. The procedure can be divided into the subsequent steps: WL fixing, N_1 fixing, (re)calculation of the raw ambiguities, and Least Squares Adjustment.

5.3.1. Fixing the WLs

Similar to PPP-AR with the conventional model, the fixing process starts with the WL fixing. Contrary to the 2-frequency-case, 3+ frequencies offer a variety of possibilities for WL LCs. In the case of processing three frequencies, three different WL LCs can be built. Under the assumption that the satellite phase delays are corrected, the three WL ambiguities are fixed by simply averaging the corresponding HMW LC over the last n epochs (e.g., the last 5 minutes) denoted as $\langle\ \rangle_n$ in the equations 5.9-5.11. Beforehand, a reference satellite is used for SD the HMW LCs and for eliminating the hardware delays of the receiver (equation 5.3).

$$\overline{WL}_{12,SD} = \langle HMW_{12,SD} \rangle_n \tag{5.9}$$

$$\overline{WL}_{13,SD} = \langle HMW_{13,SD} \rangle_n \tag{5.10}$$

$$\overline{WL}_{23,SD} = \langle HMW_{23,SD} \rangle_n \tag{5.11}$$

where $\overline{WL}_{12}$ denotes the fixed SD ambiguity of the WL LC between the first and second frequency, $\overline{WL}_{13}$ the WL LC between the first and third frequency, and $\overline{WL}_{23}$ between the second and third frequency (all in units of cycles). In the case of GPS, these WL LCs correspond to the WL, ML, and EWL LC, respectively, considering the order of frequencies used in this thesis (section 2.4.2). Table 5.1 lists the wavelengths of the Galileo WL LCs resulting from the five Galileo frequencies.

$$\overline{WL}_{12} - \overline{WL}_{13} + \overline{WL}_{23} = 0 \tag{5.12}$$

Frequency	E5a	E5b	E5	E6
E1	0.751	0.814	0.782	1.011
E5a	-	9.768	19.537	2.931
E5b	9.768	-	19.537	4.186

Table 5.1: Wavelengths of Galileo WL LCs in the unit of meters

Note that the ambiguities of these three WL LCs are linear dependent. Therefore, only two of the fixed WL ambiguities are used in the remaining fixing process. However, the third WL LC is utilized to check the consistency of the fixed WL ambiguities, presented in equation 5.12 in the unit of cycles. Suppose the WL ambiguities of a specific satellite do not fulfill this equation. In that case, this satellite is not used in the process of the fixed position's calculation.

5.3.2. N_1 fixing

$$N_{1,SD} = N_1^{refsat} - N_1 \tag{5.13}$$

$$\overline{NL}_{1,SD} = \text{LAMBDA}(NL_{1,SD}, Q_{N_1,SD}) \tag{5.14}$$

The float ambiguities on the first frequency N_1 are SD with the reference satellite's float ambiguity on the first frequency N_1^{refsat} (equation 5.13). The corresponding covariance matrix $Q_{N_1,SD}$ is calculated from the float solution's covariance matrix using error propagation. The SD ambiguities and the covariance matrix are fed into the LAMBDA algorithm (Teunissen, 1995) resulting in the SD fixed ambiguities on the first processed frequency $\overline{NL}_{1,SD}$ (equation 5.14).

$$\begin{bmatrix} \overline{WL}_{13,SD} \\ \overline{WL}_{23,SD} \\ \overline{N}_{1,SD} \end{bmatrix} = \begin{bmatrix} 1 & 0 & -1 \\ 0 & 1 & -1 \\ 1 & 0 & 0 \end{bmatrix} \begin{bmatrix} \overline{N}_{1,SD} \\ \overline{N}_{2,SD} \\ \overline{N}_{3,SD} \end{bmatrix} \tag{5.15}$$

Generally, the connection presented in equation 5.15 exists between the WL ambiguities ($WL_{13,SD}$, $WL_{23,SD}$, and $N_{1,SD}$) and the fixed raw ambiguities on the three processed frequencies ($\overline{N}_{1,SD}$, $\overline{N}_{2,SD}$, and $\overline{N}_{3,SD}$).

$$\begin{bmatrix} \overline{N}_{1,SD} \\ \overline{N}_{2,SD} \\ \overline{N}_{3,SD} \end{bmatrix} = \begin{bmatrix} 0 & 0 & 1 \\ -1 & 1 & 1 \\ -1 & 0 & 1 \end{bmatrix} \begin{bmatrix} \overline{WL}_{13,SD} \\ \overline{WL}_{23,SD} \\ \overline{N}_{1,SD} \end{bmatrix} \tag{5.16}$$

The relation in equation 5.15 is rearranged to achieve the transformation provided in equation 5.16. This transformation is used to calculate the fixed SD ambiguities $\overline{N}_{1,SD}$, $\overline{N}_{2,SD}$, and $\overline{N}_{3,SD}$ of the three processed frequencies from the fixed $\overline{WL}_{13,SD}$, $\overline{WL}_{23,SD}$, and $\overline{N}_{1,SD}$ ambiguities. The resulting fixed ambiguities of the three processed frequencies are then utilized

to calculate the fixed position.

5.3.3. Fixing two frequencies

The presented approach can be adapted for the processing of two frequencies with the un-combined model. This adaption is essential for processing the current GPS constellation since only a limited number of satellites emit signals on the third GPS frequency. For this purpose, the ambiguities of 3-frequency GPS satellites are fixed as described earlier, while the ambiguities of 2-frequency GPS satellites are fixed with the approach presented in this section. Currently (January 2022), a user typically tracks only four to six GPS satellites emitting 3-frequency signals since 16 of the 30 operational GPS satellites provide signals on L5.

In the case of 2-frequency observations, the SD ambiguity of the only WL LC is fixed in the same way as in conventional PPP-AR (section 5.2.1). Of course, it is not possible to perform the consistency check (equation 5.12) for obvious reasons.

Analogously to the fixing of three frequencies, the SD float ambiguities on the first pro-cessed frequency are fixed with LAMBDA (section 5.3.2, equation 5.13 and 5.7). However, in the 2-frequency case the following transformation is used to calculate the raw fixed am-biguities ($\overline{N}_{1,SD}$ and $\overline{N}_{2,SD}$) from the already fixed ambiguities ($\overline{WL}_{12,SD}$ and $\overline{N}_{1,SD}$).

$$\begin{bmatrix} \overline{N}_{1,SD} \\ \overline{N}_{2,SD} \end{bmatrix} = \begin{bmatrix} 0 & 1 \\ -1 & 1 \end{bmatrix} \begin{bmatrix} \overline{WL}_{12,SD} \\ \\ \overline{N}_{1,SD} \end{bmatrix} \tag{5.17}$$

5.3.4. Fixed position

After calculating the fixed ambiguities of the processed frequencies, the fixed coordinates, and ionospheric delays are estimated in a separate LSQ adjustment. Thereby, all fixed SD ambiguities $\overline{N}_{1,SD}$, $\overline{N}_{2,SD}$, and $\overline{N}_{3,SD}$ are introduced as pseudo-observations with very high weights (e.g., factor 1000) similar to the calculation of the fixed solution in conventional PPP-AR.

Using pseudo-observations for the fixed ambiguities in the adjustment avoids complex modifications of the float solution's design matrix because the float solution relies on undif-ferenced ambiguities, whereas the fixed ambiguities are SD. Besides extending the design matrix for the pseudo-observations of the fixed ambiguities, the columns of the receiver clock error, receiver clock offset(s), and residual zenith wet delay are removed because these pa-rameters are not estimated in the fixed adjustment. The float estimates of these parameters are used to correct the undifferenced observations.

On the other hand, the ionospheric delay is estimated in the Least Squares Adjustment of the fixed solution. In this way, potential imperfections of the ionospheric delay's float

estimation do not deteriorate the precision of the fixed coordinates. Furthermore, a precise estimation of the ionospheric slant delay is obtained for each satellite.

Discussion   The presented method for fixing ambiguities is straightforward and resolves ambiguities on two or three frequencies in the UC model. The procedure might be extended to any number of frequencies in a comparable way. Usually, adding the third frequency to the ambiguity fixing process has a positive impact on the convergence time (section 6). However, the number of frequencies has no effect on the position accuracy after the ambiguities and position are correctly fixed.

The presented approach works independently if an ionospheric constraint is used or not. However, without applying an ionospheric constraint in the PPP solution, the values of the ionospheric delay estimated in the fixed solution are contaminated due to the rank-deficiency between the receiver DCBs and the ionospheric delay. For example, the ionospheric delay may be negative. Furthermore, the TTFF is typically elongated.

Since the LAMBDA algorithm is used to solve N_1 instead of NL ambiguities, the fixing should be more successful. Of course, it would also be possible to fix the SD ambiguities on the second or third frequency in a similar approach. Selecting the first frequency is straight-forward because the ionospheric delay and the receiver DCBs are estimated in relation to this frequency in the float solution.

In the presented approach, the N_1 fixing is the most critical step and, usually, more problematic than the WL fixing. Note that each ambiguity fixing is independent from the others. For example, the HMW is used twice independently to fix WL ambiguities. This could be improved by using the already resolved ambiguities as a constraint in the later fixing process (e.g., EWL for WL) leading to better results and a higher fixing rate.

Alternatively, it would also be possible to directly fix the SD float ambiguities of all (three) frequencies with LAMBDA at once or use LAMBDA three times to fix each frequency's SD float ambiguities separately. Both options were tested and validated with simulated and real data. These alternatives perform worse, elongating the TTFF significantly because the LAMBDA algorithm has to decorrelate many ambiguities. Contrary to the presented approach, the LAMBDA algorithm has to be used more often or for considerably more ambiguities at once.

Note that fixing entirely undifferenced ambiguities (no reference satellite is used for SD and the provided receiver biases from, for example, TUG are applied) did not satisfy the coordinates' quality requirements. The height component absorbs residual error sources (e.g., from the ionospheric delay or biases), leading to an offset in the height component of 1-2 decimeters. Therefore, SD ambiguities should be fixed in any case and independent of the availability of receiver biases due to the reduction of error sources when differencing the observations.

6. Results

This chapter presents the results of the PPP procedures introduced earlier in the thesis using the described PPP models, fixing procedures, and observation models. Various satellite products (section 3.1) available in post-processing will be employed. Furthermore, some real-time results will be presented.

After an introduction to the quality criteria for PPP solutions, the results of the conventional and uncombined models' float and fixed solutions are presented together. Keep in mind that table A.1 in the appendix extensively explains all provided statistics. In addition to the coordinate results, the tropospheric and ionospheric delay estimates are examined since they might also be of interest to the PPP user. On the other hand, the receiver clock error and offsets, phase ambiguities, and receiver DCBs are ignored or only briefly covered. Usually, they are only by-products and eventually absorb unmodeled errors (e.g., biases).

In the following, shortcuts indicate the GNSS used in the calculation of the corresponding PPP solution. For this purpose the one letter acronyms presented in table 2.2 are used. Furthermore, if ambiguity fixing is performed for specific GNSS, lower and upper case characters are used to indicate the GNSS incorporated in the fixing process. Lowercase letters symbolize that the observations of this GNSS are used for the float solution only, and uppercase characters mean that ambiguity fixing is performed. For example, a GEc solution uses GPS, Galileo, and BeiDou in the float solution, and ambiguity fixing is performed for GPS and Galileo.

6.1. Quality criteria

Within the initial phase of a PPP solution, the estimated parameters start converging to their true values. After the convergence is achieved, the accuracy of the parameters shall be evaluated. Generally, the quality of the estimated parameters can be assessed by comparison with precise reference values, for example, originating from a network solution. Since the user is mainly interested in the position, the focus will be assessing the coordinates' quality.

Mainly observation data of reference stations is processed in this thesis since network operators usually provide these precise reference values required for an evaluation of the PPP solution. For example, the organizations within the IGS operate a global station network providing an enormous amount of observation data, daily estimates of the reference coordinates in the SINEX format[29], and five-minute estimates of tropospheric delay[30] for over 350 GNSS stations among other items. Furthermore, the ionospheric delay estimation can be contrasted with high-quality global ionospheric maps. Additionally, some satellite products cover values for the receiver clock error and receiver DCBs from the network solution for a comparison.

---

[29] IGS Formats and Standards: https://www.igs.org/formats-and-standards/
[30] IGS Troposphere Products: https://www.igs.org/products/#tropospheric_products

6.1.1. Convergence

The convergence time of a PPP solution can be described as the period until the coordinates reach a specific accuracy level and do not exceed this level afterwards. This definition of convergence has two factors: The anticipated level of accuracy and the condition on how long the coordinates should keep this accuracy level.

First, the desired level of accuracy varies with the type of the PPP solution. For example, the expected accuracy is higher for a multi-frequency PPP solution than for a single frequency solution. Second, one might be satisfied with stating convergence if the coordinates keep the specified level of accuracy only for a short period. At the extreme, this might be just a single epoch. More reasonable might be, for example, an adequate period of a few minutes.
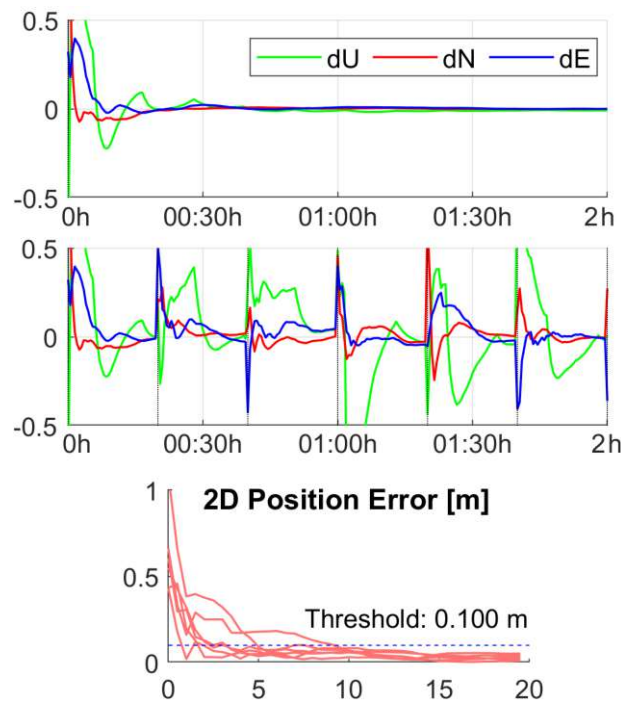
Figure 6.1: PPP solution without resets (top), with resets every 20 minutes (middle), and the 2D position difference of the resulting convergence periods (bottom)

This thesis applies the following definition for convergence: A PPP solution has reached convergence when the 2D coordinate difference is under a specific threshold and does not exceed this limit for the remaining convergence period. For the float solution, the 2D position difference with respect to the reference coordinates has to be under the threshold of 10 cm (figure 6.2) to state convergence. For the fixed solution, convergence is defined as the time to first fix (TTFF). The TTFF is achieved when the 2D position difference of the fixed coordinates stays under the threshold of 5 cm.

To assess the convergence behavior resets of the PPP solution are used corresponding to a complete restart of the calculation illustrated in figure 6.1. In this way, it is possible to

investigate the convergence periods between two resets and give a well-grounded statement on the convergence behavior. For instance, a 24 h observation file might be processed with a reset each hour, resulting in 24 convergence periods.
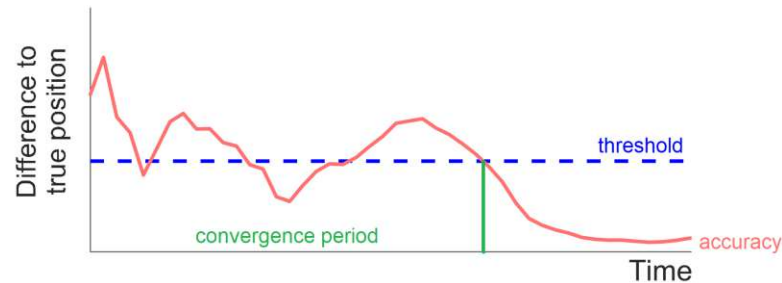
Figure 6.2: Convergence period and accuracy

This definition of convergence is quite strict, applying thresholds adapted for highly accurate positioning. Furthermore, the position difference hast to stay under the defined threshold for a considerable amount of time. Only a few epochs (or even just one!) exceeding the threshold are enough to influence the registered convergence time (figure 6.2). For example, an undetected cycle slip might shift the convergence time from a few minutes to tens of minutes. Of course, the 3D coordinate difference might be used instead of the 2D position difference to define convergence. But the user is typically more interested in the horizontal location. Furthermore, the height component is generally more problematic in GNSS-based positioning and considered separately.

6.1.2. Accuracy

In the course of this thesis, accuracy describes the deviation of an estimated parameter from its true value after the convergence has finished. This understanding of accuracy differs from the mathematical or statistical characterization. For example, the accuracy of the estimated coordinates can be assessed after the coordinates have reached convergence (figure 6.2). A reasonable indicator of the coordinate's accuracy is the 2D or 3D position difference at the end of the convergence period. Alternatively, the median or average of all coordinate estimations can be used. The convergence period only slightly influences these values, assuming that the convergence period is long enough.

Similarly, the accuracy of the other estimated parameters (e.g., ZWD) can be evaluated. Generally, effects diminishing the accuracy of the estimated parameters are limitations of the satellite products and imperfections in the observation model due to wrongly modeled or neglected error sources.

6.1.3. Residuals

The differences after parameter estimation between the observation model and the actual observations are called residuals. They are a quantity indicating how well the observation model describes reality. Imperfections or outliers (e.g., undetected cycle slips) increase the size of the residuals. Furthermore, satellite products with higher accuracy should reduce the size of the residuals. Generally, a PPP solution with small residuals is preferable to a PPP solution with large residuals because the mathematical model fits better to the actual measurements. Residuals can be calculated for code and phase observations but also for ionospheric-pseudo observations.

6.2. Test case

The IGS operates a global network with a tremendous amount of GNSS observation data and produces various products suitable for validating and assessing PPP results (e.g., daily IGS coordinate estimation for all days). Therefore, 25 stations from the IGS network covering the entire globe are randomly selected (figure 6.3) to evaluate the performance of the presented PPP processing schemes. Note that only stations providing observations with an interval of 1 second for all four globally working GNSS came into consideration. Table A.2 in the appendix lists the stations with their approximate position.
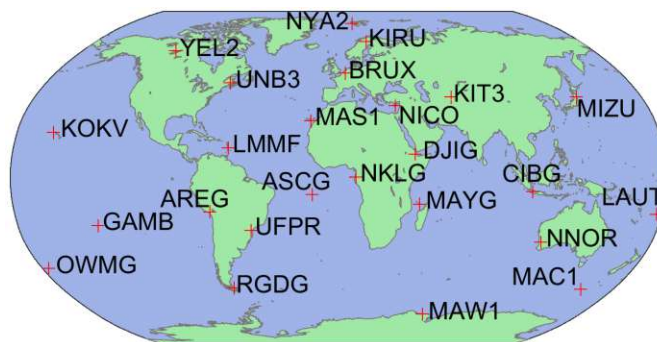
Figure 6.3: Distribution of the 25 IGS MGEX stations used in the test case

In the following tests, the satellite products from TU Graz (TUG) are used primarily. They enable PPP in the conventional and uncombined model with ambiguity fixing and allow a comparison between these two different models. For this purpose, the observations from GPS, GLONASS, and Galileo are processed because the use of multiple GNSS improves the solution and TUG products (currently) do not include BeiDou. Furthermore, BeiDou proved to provide the most challenging GNSS and, therefore, section 6.6 investigates the inclusion of BeiDou into the PPP solution.

The last two days in 2020 (December 30 and 31, 2020) are chosen as test-period. Figure 6.4 presents exemplary the average number of visible GPS satellites on December 31, 2020,

Station	Receiver type	GPS			GLONASS			Galileo			BeiDou		
AREG	SEPT POLARX5	C1W	C2W	C5Q	C1P	C2P		C1C	C5X	C7X	C2I	C7I	C6I
ASCG	TRIMBLE NETR9	C1C	C2W	(C5X)	C1P	C2P		C1X	C5X	C7X	C2I	C7I	C6I
BRUX	SEPT POLARX5TR	C1W	C2W	C5Q	C1P	C2P		C1C	C5Q	C7Q	C2I	C7I	C6I
CIBG	TRIMBLE NETR9	C1C	C2W	(C5X)	C1P	C2P		C1X	C5X	C7X	C2I	C7I	C6I
DJIG	SEPT POLARX5	C1W	C2W	C5Q	C1P	C2P		C1C	C5Q	C7Q	C2I	C7I	C6I
GAMB	TRIMBLE NETR9	C1C	C2W	(C5X)	C1P	C2P		C1X	C5X	C7X	C2I	C7I	C6I
KIRU	SEPT POLARX5	C1W	C2W	C5Q	C1P	C2P		C1C	C5Q	C7Q	C2I	C7I	C6I
KIT3	SEPT ASTERX4	C1W	C2W	C5Q	C1C	C2P		C1C	C5Q	C7Q	C2I	C7I	C6I
KOKV	JAVAD TRE_G3TH DELTA	C1W	C2W	(C5X)	C1P	C2P	(C3X)	C1X	C5X	C7X	C2I	C7I	C6I
LAUT	SEPT POLARX5	C1C	C2W	(C5X)	C1P	C2P	(C3Q)	C1C	C5Q	C7Q	C2I	C7I	C6I
LMMF	TRIMBLE ALLOY	C1C	C2W	(C5X)	C1P	C2P		C1X	C5X	C7X	C2I	C7I	C6I
MAC1	SEPT POLARX5	C1C	C2W	(C5X)	C1P	C2P		C1C	C5Q	C7Q	C2I	C7I	C6I
MAS1	SEPT POLARX5	C1W	C2W	C5Q	C1P	C2P	(C3Q)	C1C	C5Q	C7Q	C2I	C7I	C6I
MAW1	SEPT POLARX5	C1C	C2W	(C5X)	C1P	C2P		C1C	C5Q	C7Q	C2I	C7I	C6I
MAYG	TRIMBLE ALLOY	C1C	C2W	(C5X)	C1P	C2P		C1X	C5X	C7X	C2I	C7I	C6I
MIZU	SEPT ASTERX4	C1W	C2W	C5Q	C1C	C2P	(C3Q)	C1C	C5X	C7X	C2I	C7I	C6I
NICO	LEICA GR50	C1C	C2W	C5Q	C1C	C2P		C1C	C5Q	C7Q	C2I	C7I	
NKLG	SEPT POLARX5	C1W	C2W	C5Q	C1C	C2P		C1C	C5Q	C7Q	C2I	C7I	C6I
NNOR	SEPT POLARX5TR	C1W	C2W	C5Q	C1C	C2P	(C3Q)	C1C	C5Q	C7Q	C2I	C7I	C6I
NYA2	SEPT POLARX5	C1W	C2W	C5Q	C1P	C2P	(C3Q)	C1C	C5Q	C7Q	C2I	C7I	C6I
OWMG	TRIMBLE ALLOY	C1C	C2W	(C5X)	C1P	C2P		C1X	C5X	C7X	C2I	C7I	C6I
RGDG	TRIMBLE ALLOY	C1C	C2W	(C5X)	C1P	C2P		C1X	C5X	C7X	C2I	C7I	C6I
UFPR	TRIMBLE NETR9	C1C	C2W	(C5X)	C1P	C2P		C1X	C5X	C7X	C2I	C6I	
UNB3	TRIMBLE ALLOY	C1C	C2W	(C5X)	C1P	C2P		C1X	C5X	C7X	C2I	C7I	C6I
YEL2	SEPT POLARX5TR	C1W	C2W	C5Q	C1P	C2P		C1C	C5Q	C7Q	C2I	C7I	C6I

Table 6.1: Stations, receiver types, and processed signals

which ranges from 9 to 13 satellites. Similar plots for GLONASS and Galileo show a comparable global coverage. However, the mean number of visible satellites ranges from 7 to 11 for Galileo and 5 to 8 for GLONASS. So, these three GNSS provide global coverage with differing numbers of visible satellites (GPS > Galileo > GLONASS) and their signals are used in a multi-GNSS PPP solution.
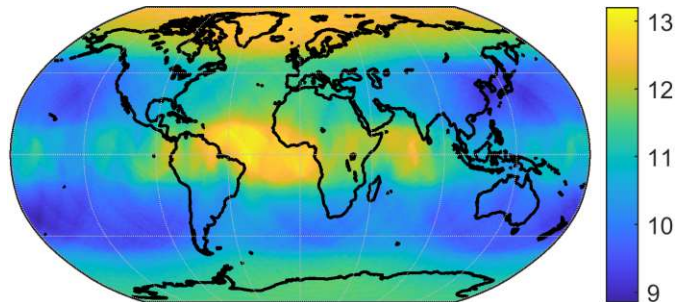
Figure 6.4: Mean number of visible GPS satellites on December 31, 2020 (calculated with TUG products)

Table 6.1 lists the selected 25 stations with their receiver type and observations used in the PPP processing. Note that for a station providing multiple observation types on a specific frequency, the observation ranking of the processing, which is included in table 6.2, decides the processed observation. For example, GPS C1W is preferred over C1C. For obvious reasons, only the first two columns (respectively frequencies) of each GNSS are relevant for the conventional model. The third column is only of interest if three frequencies are processed in the uncombined model.

However, processing three GNSS frequencies shows some limitations. In the first place, not all stations provide three frequency observations for GLONASS (and BeiDou). Anyway, TUG products do not provide biases for the third GLONASS frequency. Furthermore, some stations (ASCG, CIBG, GAMB, KOKV, LAUT, LMMF, MAC1, MAW1, MAYG, OWMG, RGDG, UFPR, UNB3) provide only C5X observations for the third GPS frequency. Unfortunately, TUG products do not provide biases for GPS C5X and L5X.

Therefore, in the uncombined model, only two GLONASS frequencies can be utilized in the processing in general and only two GPS frequencies for the mentioned stations. This circumstance is indicated with parentheses in table 6.1 which also includes BeiDou observations although only covered in section 6.3.

Table 6.2 shows an overview of the processing settings, including references to the corresponding sections in this thesis. Note that segments of table 6.2 which are only valid for the uncombined model are written in italic (e.g., ionosphere model). The included observation ranking decides which signal is processed if a receiver records multiple signals on a frequency of a specific GNSS. For example, in case C1C and C1W are tracked on the GPS L1 frequency, the C1W (P-code) measurements are processed.

Furthermore, table 6.3 shows the stochastic settings of the Kalman Filter. Section 4.4.3

Software	raPPPid (VieVS PPP)
Stations	25 globally distributed IGS stations
Period	December 30 and 31, 2020 (day 3 and 4 of GPS week 2138)
Observation interval	1 sec, reset of the solution every 15 min
Observation ranking	GPS: WC, GLONASS: PC, Galileo: CQX, and BeiDou: IX
Raw observation noise	Code 30 cm, phase 2 mm
Observation weighting	Elevation based weighting, $\sin(elev^2)$
Troposphere model	VMF3 + GRAD (Landskron and Böhm, 2018a; Landskron and Böhm, 2018b), residual zenith wet delay is estimated
Ionosphere model	*IGS final, ionospheric pseudo-observations for 30 s, initial standard deviation of 15 cm is increased to 3 m (section 4.4.3)*
Correction models	Relativistic effects, Phase Wind-Up, receiver antenna height, phase center offsets and variations, solid Earth tides, ocean loading, GDV (all models described in section 3)
Adjustment Parameters	Kalman Filter (stochastic settings: table 6.3) receiver coordinates, receiver clock error, receiver clock offsets, ZWD, float ambiguities, *ionospheric delays, receiver DCBs*
Cycle-slip detection Outlier detection	$dL_i - dL_j$ (section 4.4.1) Check of observed minus computed (section 4.4.1)
PPP-AR	Fixing cutoff: 10°, fixing starts after 30 s, the highest satellite is selected as reference satellite (section 5.1)

Table 6.2: General processing settings. Settings written in italic are only valid for the uncombined model.

Parameter	Initial std $[m]$	System Noise $[m/\sqrt{h}]$
Coordinates	10000	0
ZWD	0.1	0.005
Receiver clock error	300000	300000
Receiver clock offsets	300000	300000
Receiver DCBs	3	0
Float ambiguities	20	0
Ionospheric Delay	1	1

Table 6.3: The Kalman Filter's stochastic settings used in the processing. Section 4.4.3 explains these values in detail. The parameters written in italic are only estimated when applying the uncombined model.

provides an explanation to these values. Along with the previous content, the tables 6.2 and 6.3 describe the framework of the test case. The following sections present the results.

6.3. Coordinates

The coordinates' results investigation is divided into float and fixed coordinates. Thereby, the performance of the conventional and uncombined model using two frequencies in the processing are compared. Furthermore, the effect of adding observations on a third frequency in the uncombined model is illustrated.

6.3.1. Float coordinates
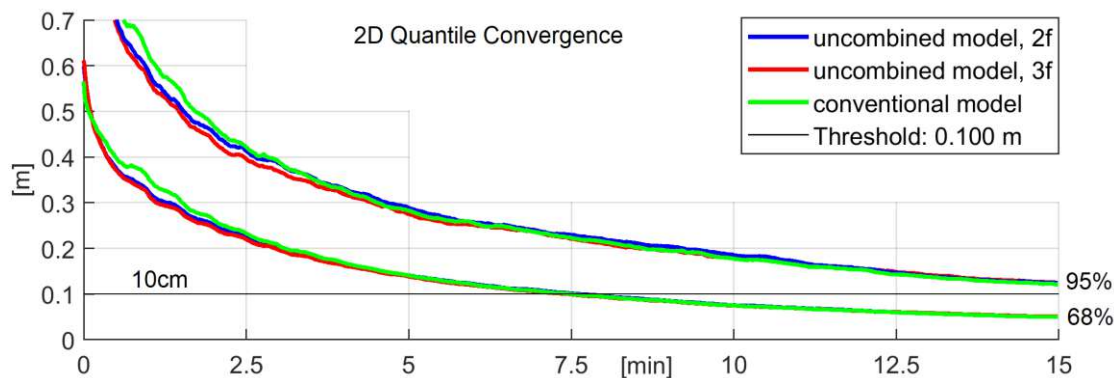
Figure 6.5: The float coordinates' 68% and 95% quantile of the 2D position difference of all stations using the conventional or uncombined model (2 or 3 frequencies)

Figure 6.5 shows the 68% and 95% quantile of the 2D position difference of all stations for the conventional and uncombined model using two or three frequencies. The uncombined model performs better than the conventional model in the first few minutes because the observation noise is increased when building the IF LC. Thanks to the high observation rate (1 sec), this effect vanishes relatively fast, and after about four minutes, no difference is perceptible in figure 6.5. Note that the difference is more significant (e.g., for a more extended period) when using observation with lower observation rate (e.g., 30 sec).

	IF	UC 2	UC 3
Average convergence time [min]	6.85	6.84	6.73
Median convergence time [min]	6.33	6.34	6.20
Median 3D position difference of all epochs [cm]	12.61	12.33	12.17
Average 3D position difference after 15.00 minutes [cm]	6.80	7.01	7.33

Table 6.4: The float solution's convergence time and accuracy

Table 6.4 shows the performance of the float solution regarding convergence time and accuracy. Note that the improvement of the mean and median convergence time is small (IF → UC2 → UC3), although the visible improvement in figure 6.5. The reason is that this difference usually vanishes until the solution reaches sub-decimeter accuracy. The mean and median convergence time would reflect this improvement when using observations with a lower observation rate (e.g., 30 sec). Furthermore, the conventional and uncombined model achieve a similar coordinate accuracy. Only slight differences are identifiable in figure 6.5 and table 6.4.

In table 6.4 the uncombined model using three frequencies outperforms the uncombined model using two frequencies in nearly all regards, demonstrating the positive effect of a third frequency in the processing. The worse mean 3D position difference after 15 minutes when using three frequencies can be explained by the missing receiver PCOs and PCVs of the third frequency. The first frequency's values used as a replacement are less accurate than calibration values.
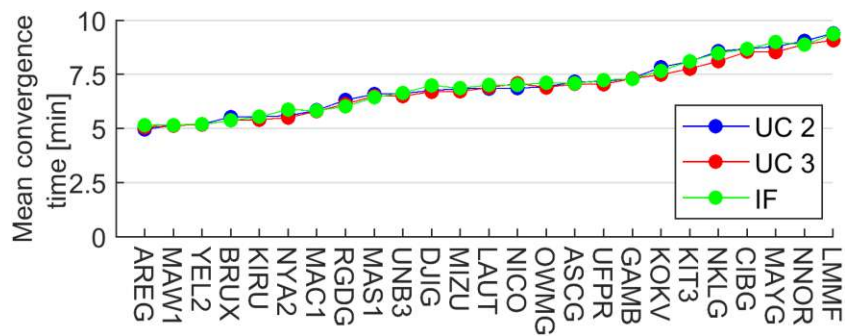
Figure 6.6: Average float convergence time (2D < 10cm) for each station

Figure 6.6 shows the average float convergence time for each station. There are good and bad stations with a short and long convergence time, respectively. Most stations converge within five to seven minutes to a horizontal position difference below ten centimeters. Only a few stations require some minutes more for convergence.

The conventional and uncombined model using two frequencies perform similarly over the stations. A perceptible improvement is seen in figure 6.6 when adding the third frequency in the uncombined model for most stations (e.g. KIRU, NNOR). No station converges slower with three frequencies and usually faster as with the conventional model. Note that good stations perform well independent from the PPP model. Experience shows that also the satellite product does not have an impact.

In table A.3 in the appendix, the stations sorted by their mean convergence time and the corresponding receiver type and signals used in the processing are listed. Septentrio receivers (e.g., SEPT POLARX5) tend to perform better than other receiver types. For example, the seven fastest converging stations are all equipped with a Septentrio receiver. Section 7.7 takes a detailed look at this circumstance.

Table A.4 shows the median coordinate convergence time and 68% quantile of the ZTD difference with respect to the IGS troposphere product for each station. Furthermore, the table lists the median 3D position difference after 15 minutes. This value is independent of the convergence period and a good indicator for the accuracy achieved at each station. Fast converging stations tend to reach a higher position accuracy. Again, this can be explained with the receiver type as shown in section 7.7.
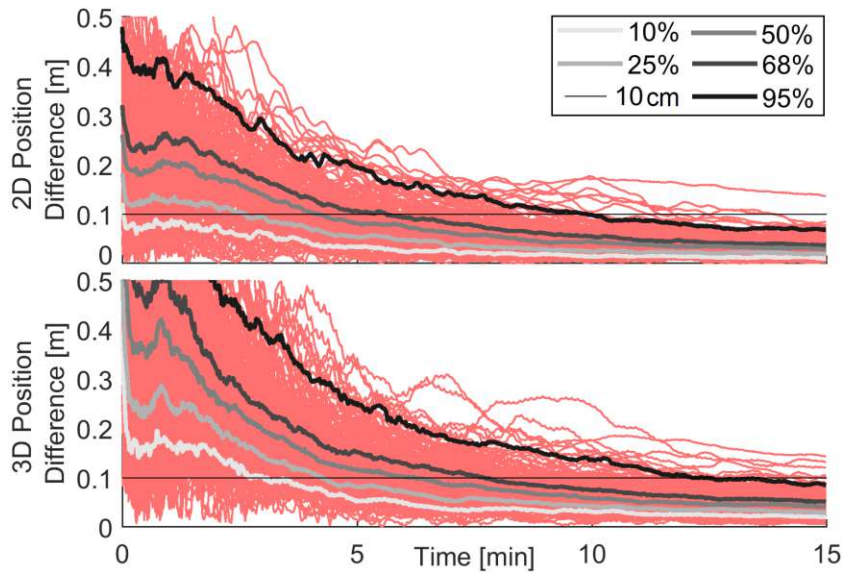
Figure 6.7: 2D (top) and 3D (bottom) position difference of the station KIRU (Kiruna, Sweden) on December 30 and 31, 2020, using three frequencies in the uncombined model. Differently shaded grey lines represent various quantiles explained in the legend.

Figure 6.7 shows the 2D and 3D position difference of all convergence periods using the uncombined model with three frequencies and observations from the station KIRU (Kiruna, Sweden) on December 30 and 31, 2020. Additionally, the corresponding 10%, 25%, 50%, 68%, and 95% quantiles are plotted in different shades of grey. This illustration gives an idea of the convergence and accuracy for one of the best-performing stations.

Nearly 25% of the solutions achieve an instantaneous convergence with a 2D position difference below ten centimeters immediately at the start (top part of figure 6.7). After 5 minutes, about 68% convergence periods have converged considering the trend of the corresponding 2D position difference's 68 % quantile. Furthermore, centimeter-level accuracy is achieved even for the 3D position difference within 10 minutes for most convergence periods (between 68% and 95%, lower part of figure 6.7).

While the 2D position difference curves behave relatively smooth, the 3D position difference curves are slightly noisier. This may be induced from the height component and the simultaneous ionospheric delay estimation in the uncombined model since the conventional model does not show such an effect. Due to correlation, this behavior is also noticeable in

the estimation of the ZWD (section 6.4).

Note that in the processing, the third GLONASS frequency (G3) and GPS C5X and L5X observations, which are observed from about half the stations (ASCG, CIBG, GAMB, KOKV, LAUT, LMMF, MAC1, MAW1, MAYG, OWMG, RGDG, UFPR, UNB3) were not used because TUG products do not contain biases for these signals. Anyway, only very few stations would provide observations on G3. Therefore, only Galileo observations on E5b are added to the uncombined model for half of the stations. Despite these limitations, three frequencies outperform two frequencies in the uncombined model.

6.3.2. Fixed coordinates

As soon as a sufficient number of ambiguities is fixed, the fixed coordinates are calculated in a separate LSQ as explained in chapter 5. Remember that the TTFF is achieved when the 2D difference of the fixed coordinates is below five centimeters for the remaining convergence period. In the following, the performance of these fixed coordinates is examined, first applying the conventional and then the uncombined model.
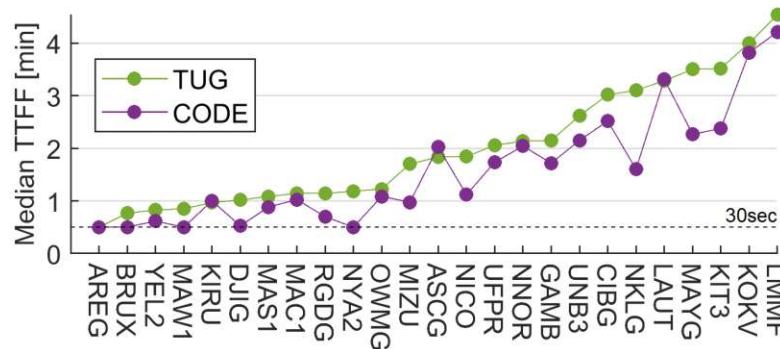
Figure 6.8: Median TTFF for each station using the conventional model and the satellite products from TUG (green) or CODE (purple)

Figure 6.8 shows the median TTFF for each station applying the **conventional model** and TUG products (green) or CODE products (purple). Furthermore, table A.5 in the appendix presents station-wise the median TTFF, percentage of convergence periods without correct fix, and median 3D position difference after 15 minutes. In figure 6.8 as well as table A.5 the stations are sorted by their median TTFF using TUG products. Table 6.5 shows the overall statistics of the conventional model's fixed solution.

Using CODE instead of TUG products undoubtedly improves the convergence for nearly every station and leads to the shortest TTFF amongst all satellite products (Glaner and Weber, 2021). Since the float solution differences are negligible, this originates most likely from a varying quality in the satellite phase biases. Independently of the satellite products, the position accuracy is identical when the ambiguities are correctly fixed.

The black dotted line in figure 6.8 indicates the start of the fixing after 30 seconds. About

	CODE	TUG
Average time to correct fix [min]	2.86	3.27
Median time to correct fix [min]	1.33	1.77
Percentage of cases without correct fix [%]	16.88	20.99
Median 3D position error after 15.00 minutes [cm]	3.24	3.49
Average 3D position error after 15.00 minutes [cm]	9.84	10.51

Table 6.5: Statistics of the conventional model's fixed solution

half of the stations have a median TTFF around one minute or below using CODE products. Furthermore, at some stations (AREG, BRUX, MAW1, DJIG, NYA2) the median TTFF coincides with the start of the fixing. In other words, in at least 50% of the cases, these stations accomplish a horizontal position difference under 5 centimeters instantaneously after the fixing starts. Note that all these five stations are equipped with a Septentrio PolaRx5 receiver. Furthermore, nine out of the ten best-performing stations in table A.5 operate a Sepentrio receiver. Section 7.7 deals with an explanation of this performance.
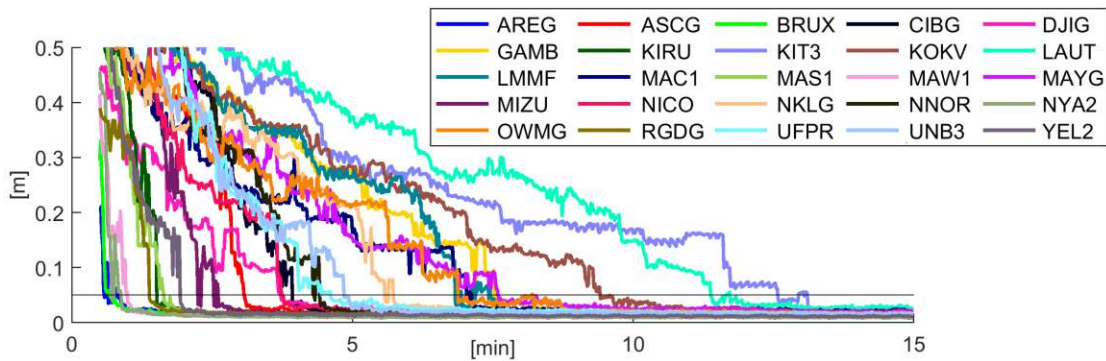
Figure 6.9: 68% quantile of the 2D fixed position difference for each station using the conventional model and CODE products

Figure 6.9 shows the 68% quantile of the fixed horizontal position difference for each station using the conventional model and CODE products. Similar to the float solution, we can identify good stations with a fast converging 68% quantile in figure 6.9 and small median TTFF in figure 6.8. On the other hand, bad stations have a slowly converging 68% quantile in figure 6.9 and and a large median TTFF in figure 6.8. For example, the median TTFF ranges from 30 seconds for good stations to a little bit more than four minutes for bad stations.

The classification of good and bad stations does not change significantly compared to the float solution. Based on the float solution's results, only the stations LAUT and KOKV perform

worse than anticipated. LAUT performs as expected most of the time, but no correct fix is accomplished during a few hours of the day, indicating some receiver-related (e.g. signal tracking) anomaly. In the case of the station KOKV, the missing PCO and PCV corrections for all Galileo frequencies are replaced with the GPS values.

Usually, the float solution's performance is not affected by imperfections of the PCOs and PCVs because the estimation of float ambiguities mainly absorbs them. Therefore, exact receiver phase center offsets and variations are crucial for the ambiguity fixing process explaining the weakened fixed solution of KOKV. Furthermore, the corresponding ANTEX file (igsR3_2077.atx) lacks calibrations for the third frequencies of GPS and GLONASS relevant for the uncombined model. These missing corrections are replaced with the values of the corresponding first frequency.

In the following, the results of the **uncombined model**'s fixing approach (section 5.3) are presented. It turned out that the fixing is not successful for GPS observations when applying TUG products together with the uncombined model. Especially, specific GPS satellites (e.g., G04) or satellite types seem to be troublesome. Under the assumption that the satellite products are correct for GPS, this is most likely due to a different model during the calculation of the satellite products and the PPP solution.

Nevertheless, the uncombined model's fixing approach succeeds with Galileo observations when applying TUG products. Consequently, the results of a grE solution in the uncombined model are presented below. Thereby, the PPP solution relies only on fixed ambiguities of Galileo satellites and additionally uses GPS and GLONASS observations in the float solution.

Of course, this leads to only a few satellites possible to fix because typically 7-11 Galileo satellites are visible. Therefore, the fixed solution of the uncombined model has to perform worse compared to the conventional model, which successfully resolves GPS and Galileo ambiguities. Consequently, a comparison of the results is not straightforward. However, an assessment and validation of the functionality of the fixing approach in the uncombined model can be given.

Average time to correct fix [min]	9.63
Median time to correct fix [min]	9.83
Percentage of cases without correct fix [%]	35.50
Median 3D position error after 15.00 minutes [cm]	5.98
Average 3D position error after 15.00 minutes [cm]	10.59

Table 6.6: Statistics of the uncombined model's fixed solution (grE)

Table 6.6 presents the overall statistic of the uncombined model's fixed solution. An average and median convergence time under 10 minutes is achieved for all stations, although only Galileo satellites are fixed. This also explains the much higher percentage of convergence periods without a correct fix compared to the conventional model. Table A.6 in the appendix presents station-wise the median TTFF, percentage of convergence periods without

correct fix, and median 3D position difference after 15 minutes. The median TTFF ranges between 6 and 8 minutes for the best stations. A correctly fixed position within 5 minutes is regularly achieved for these stations.

Figure 6.10 presents a typical example of the fixed coordinate solution in the uncombined model showing the convergence period of the station AREG (Arequipa, Peru) on December 31, 2020, starting at 2:45h. Remember that the TTFF is achieved when the 2D position difference of the fixed coordinates stays under the threshold of 5 cm. Therefore, although a correct fix takes place already after one minute, the TTFF is achieved not before seven minutes because wrong fixes repeatedly disrupt a stable fixing process.
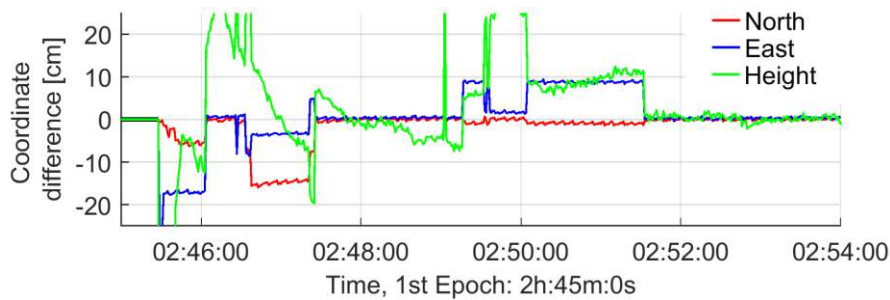
Figure 6.10: Fixed coordinates of the station AREG (Arequipa, Peru) using the uncombined model and TUG products on December 31, 2020

Generally, the fixed solution of the uncombined model proved to be less stable than the conventional model. Regularly wrong fixes elongate the TTFF or prevent convergence within 15 minutes. This fundamental problem in PPP-AR is more pronounced in the uncombined model. Since only Galileo satellites are fixed, the rate of wrong fixes should be lower with a higher number of fixable satellites. But also residual ionospheric effects and imperfections in the PCOs and PCVs due to missing antenna calibrations might map into the ambiguities impeding the fixing process.

The presented example and statistics validate the introduced fixing method in the uncombined model. Fixing the ambiguities of a second GNSS would improve the performance, and the fixing approach in the uncombined model could then be comparable to the conventional model. Nevertheless, there are some open issues regarding available satellite products, antenna calibrations, and the current GNSS constellation, which might be solved in the future. For example, more GPS satellites will provide L5 signals, and more satellites products will enable PPP-AR in the uncombined model even for the Galileo E6 frequency. Using E6 instead of E5b as the third frequency in the processing could be promising because processing the E5a as well as the close E5b frequency can be avoided.

The fixed coordinates show an intriguing behavior: regular small jumps can be identified (figure 6.10). They look like shark teeth and are also clearly visible in figure 5.1. The length of such a shark tooth is typically 6 or 7 seconds and its size is under 1 cm, usually a few millimeters. Sometimes they are more distinct in the East component.

These fluctuations occur in both PPP models (figure 5.1: conventional model and figure 6.10: uncombined model), but usually they are more pronounced in the uncombined model. This might be due to the preservation of the raw observations' noise in the uncombined model. The fluctuations may result from different interpolations used in the calculation of the PPP solution (e.g., satellite orbits and clocks) and the resulting residual errors map in the coordinates.

Similar behavior with identical length is found in the float coordinates (figure 5.1) and mainly the height component. However, the size of these fluctuations is clearly smaller due to the float solution's lower accuracy and decreases over time because the filter gets stronger, preventing such small oscillations.
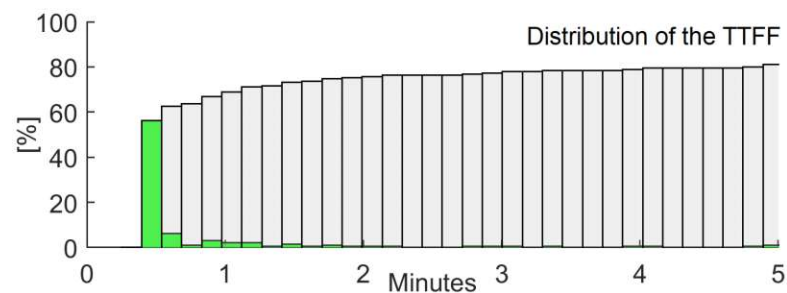
Figure 6.11: Distribution of the TTFF for the station BRUX on December 30 and 31, 2020, applying CODE products

To illustrate which fixing performance is possible at the very top, figure 6.11 shows the TTFF's distribution of the station BRUX (Bruxelles, Belgium) for December 30 and 31, 2020, applying the conventional PPP model and the satellite products from CODE. Green bars indicate the rate of convergence periods achieving a correct fix at a specific point in time. Grey bars show the percentage of convergence periods already correctly fixed until this time. Therefore, the height of a grey bar equals the size of green bars simultaneous or previous in time. Note that the station BRUX is one of the best-performing stations operating a SEPT POLARX5TR receiver with an JAVRINGANT_DM NONE antenna.

Nearly 60% of the convergence periods are fixed instantaneously when the fixing starts after 30 seconds. Afterward, a few correct fixes occur in the first 2 minutes. Only sporadic green bars and TTFFs happen in the remaining period shown in figure 6.11. Therefore, the grey bars increase only slightly over time, and in 81% of cases, the position is correctly fixed after five minutes. This slight linear trend continues, and the percentage of correctly fixed solutions increases to 91% until minute 15. The great majority of TTFFs occur right after the fixing start or within the first minute of the processing.

Motivated by the presented performance of the station BRUX, the observation data of the five best-performing stations (AREG, BRUX, MAW1, DJIG, NYA2) is reprocessed with the same settings (e.g., CODE products and the conventional model). However, the fixing now already starts after 10 seconds. Note that all these five stations operate a Septentrio PolaRx5

receiver (section 7.7).
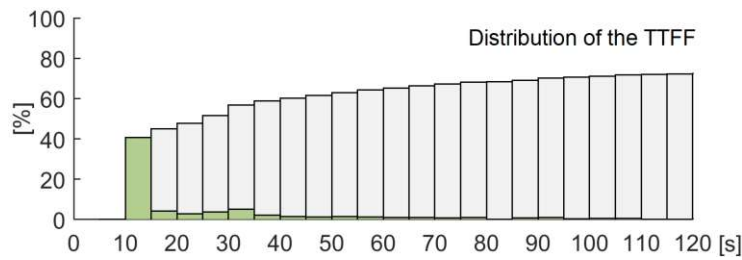
Figure 6.12: Distribution of the TTFF for the five best-performing stations AREG, BRUX, MAW1, DJIG, and NYA2 on December 30 and 31, 2020, applying CODE products

Similarly to figure 6.11, figure 6.12 shows the resulting TTFF's distribution in the first two minutes for these five stations. A instantaneous correct fix is achieved in 41% of the cases. Furthermore, after 1, 2, 5, and 10 minutes, respectively, about 64, 72, 78, and 83 % of the convergence periods are correctly fixed. About 12% of the convergence periods do not converge within 15 minutes. Since the definition of a correct fix requires the 2D position difference staying under the threshold of 5 centimeters the remaining convergence period, this example demonstrates that a stable nearly-instantaneous coordinate convergence is possible with PPP.

6.4. Tropospheric delay

The PPP solution allows for an estimation of the ZWD. By adding this estimated ZWD to the ZHD modeled during the processing with a troposphere model (e.g., VMF), it is possible to calculate the ZTD useful, for example, for tropospheric tomography (Adavi et al., 2022). In the following, the PPP solution's ZTD values are compared with the troposphere product of the IGS[31], which is produced with a latency of up to four weeks and provides the tropospheric delay in zenith direction with an accuracy of a few millimeters. This reference has a temporal resolution of 300 s, and a linear interpolation is used to calculate the ZTD difference for epochs in-between.

Figure 6.13 shows the 68% and 95% quantile of the ZTD difference for all convergence periods of the test case. The conventional PPP model performs slightly better than the uncombined model in the first three to four minutes. However, this difference vanishes over time and is less significant when using three frequencies in the uncombined model. The convergence time shows a length similar to the convergence period of the coordinates. Afterward, the conventional and uncombined model perform nearly identical, and the ZTD estimation has an accuracy of one to two centimeters or even at the millimeter level.

The standard deviation of the uncombined ZTD's difference is smaller (3.91 or 4.02 cm using two or three frequencies, respectively) than for the conventional model (5.50 cm),

---

[31] IGS Troposphere Products: https://www.igs.org/products/#tropospheric_products
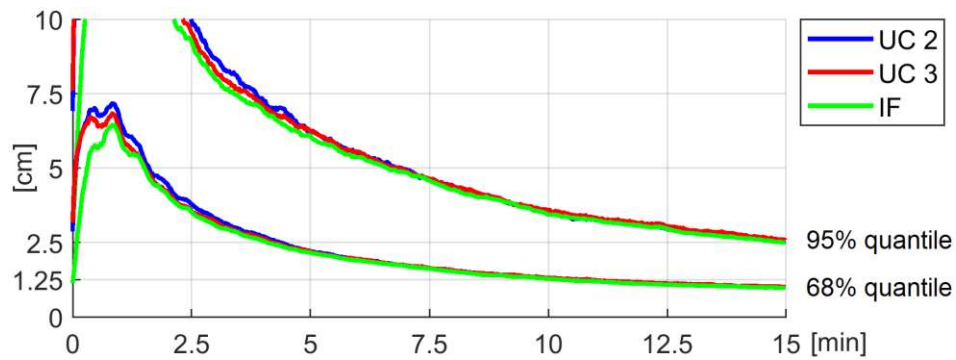
Figure 6.13: Quantiles of the ZTD difference with respect to the IGS troposphere product for the conventional and uncombined model with two or three frequencies

indicating that the conventional model's ZWD estimation contains more outliers. For both PPP models, the biases of the ZTD difference are negligible and in the size of one millimeter or even below.
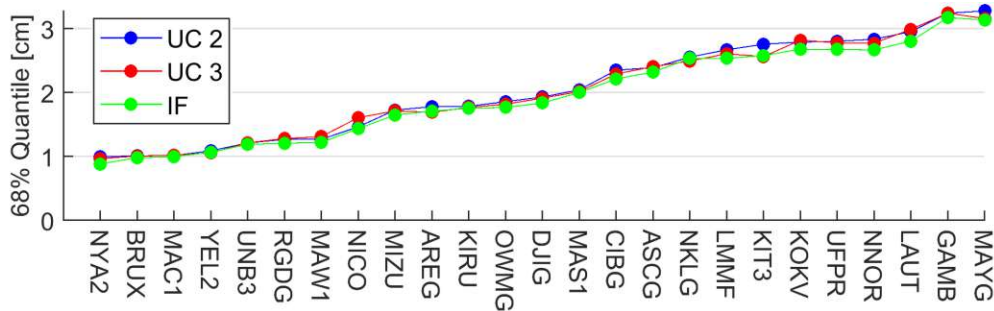
Figure 6.14: The 68% quantile of the ZTD difference with respect to the IGS troposphere product for each station

Figure 6.14 shows the 68% quantile of the ZTD difference for each station. About two-thirds of all epochs have a smaller ZTD difference than the value presented in the graph. Therefore, figure 6.14 presents a representative value showing the accuracy of the ZTD estimation for each station, excluding inaccurate values during the convergence period and outliers. Like the coordinates, some stations perform better than others, but 2-3 centimeter accuracy or below is achieved for most stations.

Table A.4 in the appendix contains the values of the ZTD difference's 68% quantile for the conventional and uncombined model using two and three frequencies. In this table, the stations are ordered based on their coordinate convergence time. Stations converging faster tend to provide more accurate ZTD values.

However, some stations provide less accurate values for the ZTD than stations with similar convergence performance (e.g., AREG, LAUT, GAMB, MAYG). These stations located close to the equator (figure 6.3) tend to perform worse than stations with similar convergence performance in higher latitudes. More diffuse environments for estimating the ZWD (e.g.,

wet air or sudden heavy rainfalls) could explain this behavior. The PPP's ZWD estimation might not reflect such small changes due to the constraint in the Kalman Filter. Tuning the stochastic settings could improve the estimation of the ZWD for these stations.
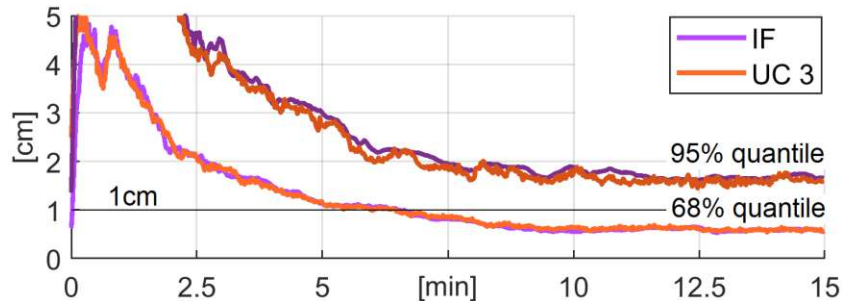
Figure 6.15: The ZTD difference's 68% and 95% quantile for the station YEL2 on December 30 and 31, 2020, using the conventional model (IF) and the uncombined model with 3 frequencies (UC 3)

Figure 6.15 shows the ZTD difference's 68% and 95% quantile of the station YEL2 (Yellowknife, Canada) on December 30 and 31, 2020. YEL2 is one of the best-performing stations regarding the coordinates' and ZTD's performance. After a convergence time of about 6 minutes, the ZTD's difference is accurate at the centimeter to millimeter level. Furthermore, figure 6.15 indicates that the ZTD estimation with the uncombined model is less smooth. This may be explained that the ionospheric delay is being estimated simultaneously. However, the conventional and uncombined model perform quite similar for this station.

6.5. Ionospheric delay

The IF LC almost completely removes the ionospheric delay from the mathematical model in the conventional model. Therefore, no information about the ionosphere can be obtained. On the other hand, each satellite's slant ionospheric delay is estimated on the first processed frequency (e.g., GPS L1, GLONASS G1, Galileo E1) when using the uncombined model. This PPP estimation of the ionospheric delay is compared with modeled values from the final IGS GIM. Note that the ionospheric pseudo-observations calculated from this model and used to constrain the ionospheric delay's estimation are only introduced in the first 30 seconds of the convergence period.

The resulting differences of the ionospheric delay on the first frequency between the GIM and the PPP estimation are examined below. Keep in mind that 1 TECU approximately corresponds to a delay of 16 cm on the GPS L1, GLONASS G1, or Galileo E1 frequency. Table 6.7 shows the standard deviation and bias in the uncombined model using three frequencies on December 30 and 31, 2020. The stations are sorted by their mean convergence time. Furthermore, the approximate stations' locations are listed.

The standard deviation of the ionospheric delay's difference is under 1 m for all stations and typically ranges from 30 cm to 50 cm. Stations near the equator (e.g., with a latitude

Station	December 30		December 31		Latitude	Longitude	Height
	std	bias	std	bias			
AREG	0.688	-0.306	0.592	-0.266	-16.465	-71.493	2489.742
MAW1	0.338	-0.013	0.361	-0.028	-67.605	62.871	59.633
YEL2	0.287	0.016	0.228	0.016	62.481	-114.481	181.452
BRUX	0.279	-0.038	0.253	-0.047	50.798	4.359	158.694
KIRU	0.300	0.040	0.276	0.030	67.857	20.968	391.348
NYA2	0.392	-0.021	0.347	0.009	78.930	11.859	81.914
MAC1	0.383	-0.039	0.351	-0.020	-54.500	158.936	-6.259
RGDG	0.914	-0.086	0.954	-0.051	-53.786	-67.752	32.800
MAS1	0.909	0.000	0.641	-0.027	27.764	-15.633	197.570
UNB3	0.290	0.031	0.286	0.034	45.950	-66.642	23.32
DJIG	0.735	-0.278	0.841	-0.263	11.526	42.847	711.812
MIZU	0.393	-0.108	0.345	-0.105	39.135	141.133	117.427
LAUT	0.913	0.006	0.695	-0.162	-17.609	177.447	90.074
NICO	0.438	-0.185	0.451	-0.215	35.141	33.396	192.145
OWMG	0.397	-0.064	0.353	-0.111	-44.024	-176.369	22.027
ASCG	0.641	-0.157	0.618	-0.166	-7.916	-14.333	38.354
UFPR	0.581	-0.090	0.586	-0.103	-25.448	-49.231	926.179
GAMB	0.710	-0.165	0.647	-0.120	-23.130	-134.965	81.068
KOKV	0.567	-0.063	0.544	-0.096	22.126	-159.665	1167.930
KIT3	0.496	-0.116	0.484	-0.140	39.135	66.885	623.0250
NKLG	0.666	-0.209	0.580	-0.228	0.354	9.672	31.890
CIBG	0.724	-0.263	0.718	-0.227	-6.490	106.849	169.534
MAYG	0.462	-0.093	0.606	-0.078	-12.782	45.258	-15.947
NNOR	0.395	-0.031	0.348	-0.017	-31.049	116.193	235.248
LMMF	0.825	-0.186	0.913	-0.096	14.595	-60.996	-26.566

Table 6.7: The standard-deviation and bias of the ionospheric delays' difference between IGS final GIM and the PPP estimation on December 30 and 31, 2020, for the uncombined model using three frequencies. The stations are sorted by their mean convergence time (figure 6.6). All values are in the unit of meters or degrees, respectively.

of $\pm 30°$) tend to have a higher standard deviation (e.g., DJIG, LAUT, or NKLG). This may be due to larger and less precise TEC values of the GIM around the equator. Note that the standard deviation for a specific station shows quite similar values on both days.

Also, the bias usually does not vary significantly from one day to another. Furthermore, it is at the size of a few centimeters up to one decimeter for most stations and negligible. However, for some stations located near the equator, the ionospheric delay's bias amounts a few decimeters (e.g., DJIG, GAMB, or CIBG). On both days, the station AREG (Arequipa, Peru) experiences the most significant bias (about 30 cm), which might be explained by the altitude of the station (about 2500 m above sea-level).
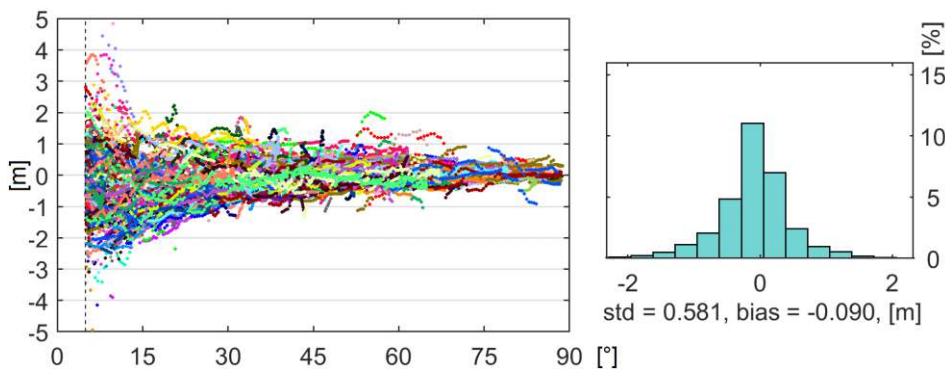
Figure 6.16: The ionospheric delays' difference for the station UFPR (Curitiba, Brazil) on December 30, 2020. The left plot shows the ionospheric delays' difference over elevation, the right plot the corresponding histogram.

Figure 6.16 shows the ionospheric delay's difference over elevation for all satellites (left plot) and the corresponding histogram (right plot) for UFPR (Curitiba, Brazil) on December 30, 2020. For creating the left graph, every 60th epoch was used to make the plot clearer. The ionospheric delays' difference ranges up to a few meters for low elevations, and it is at the sub-meter level for high elevations. Obviously, there is an elevation-based trend of the ionospheric delays' difference between the IGS GIM and the PPP estimation justifying the weighting of the ionospheric pseudo-observations (section 4.4.3). An explanation for this behavior might be imperfections in the ionospheric mapping function used to convert the VTEC values in the signal direction for low elevation angles.

The PPP solution is successfully validated with the IGS final GIM. However, it is difficult to give an assessment on the precision of the ionospheric delays' estimation. Usually, the final IGS GIM has an accuracy of 2-8 TECU corresponding to a delay error of 0.3-1.3 m on the L1 frequency. The presented standard deviations are below the given accuracy of the GIM, and the PPP solution should achieve higher precision. Furthermore, table 6.7 and figure 6.16 support the magnitude of the ionospheric constraint presented in section 4.4.3 and weighting the ionospheric pseudo-observations dependent on elevation.

In the future, high precise ionospheric delays might be used as a tight ionospheric constraint fastening convergence. Furthermore, it might be possible to convert the estimated

slant ionospheric delays with a mapping function into VTEC values and integrate PPP to create GIMs.

6.6. Processing BeiDou

Due to the rapid development of the BeiDou system, a quickly evolving number of satellites is in space. The web page of the Test and Assessment Research Center of China Satellite Navigation Office (TARC) gives an overview of the current state[32]. Currently (March 2022), 44 BeiDou satellites operational for positioning are in orbit.
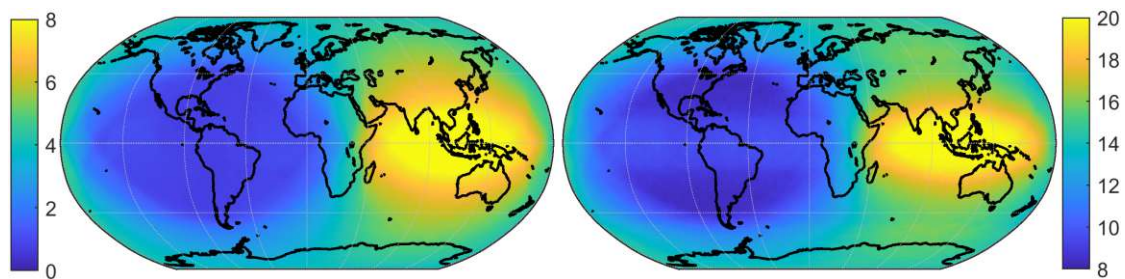
Figure 6.17: Mean number of visible BeiDou satellites covered by the MGEX products of CODE (left) and WUM (right) without the GEO satellites C01-C05 on December 31, 2020

Figure 6.17 shows the mean number of visible BeiDou satellites on December 31, 2020, calculated with the MGEX products of CODE (left side) and WUM (right side). Considering the different scales of the color-coding, it becomes clear that the average number of available satellites is considerably higher when using WUM. The reason is that WUM contains data for a total of 42 BeiDou satellites[33], while CODE products only hold data for 10 BeiDou satellites[34]. Furthermore, some ACs (e.g., TUG or CNES) do not involve BeiDou in their satellite products at all.

Contrary to other GNSS, the BeiDou system includes GEOs (e.g., C01-C05) and IGSOs in addition to MEO satellites (section 2.1.4). Usually, the orbit accuracy of GEO satellites is significantly lower compared to the other BeiDou satellite types because GEO satellites maintain almost stationary with respect to the Earth (Y. Liu et al., 2018). Therefore, the observations received from GEO satellites are typically excluded from the PPP solution.

In any case, some satellite products do not contain precise orbit and clock information for the GEO satellites of BeiDou. While WUM provides orbits, clocks, and biases for the GEO satellites C01-C05, CODE does not. To facilitate the comparison between CODE and WUM in figure 6.17, the GEO satellites C01-C05 have been excluded for WUM. Therefore, the number of available BeiDou satellites is even higher in the longitude belt from 50°E to 170°E (East Asia and Australia).

---

[32] TARC: http://www.csno-tarc.cn/en/system/constellation
[33] C01-C14, C16, C19-C30, C32-C46
[34] C06-C14, C16
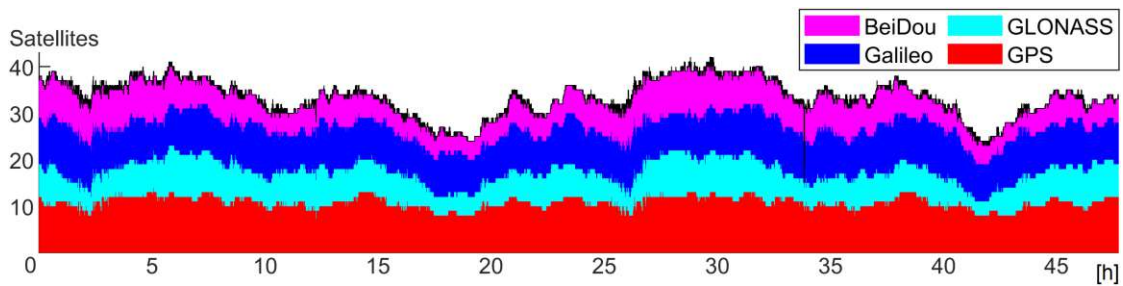
Figure 6.18: Number of observed GNSS satellites at station DJIG on December 30 and 31, 2020

To illustrate the performance of PPP solutions including BeiDou observations, the station DJIG (Djibouti, figure 6.3) at the border of the peak area of available BeiDou satellites is selected. This station performed at an average level previously (e.g., figure 6.6 or 6.14). Both days (December 30 and 31, 2020) of the test period are processed.

Figure 6.18 presents the number of observed GNSS satellites from the station DJIG on December 30 and 31, 2020. The total amount of satellites in view mainly ranges from 30 to 40 satellites. While the number of visible GPS and Galileo satellites is relatively consistent, it fluctuates considerably more for BeiDou and GLONASS. After excluding specific satellites during the processing (e.g., under the cutoff angle), the number of satellites used in the PPP solution varies from 8-12 for GPS, 8-10 for Galileo, 5-8 for GLONASS, and 4-8 for BeiDou. So, the global coverage of BeiDou is still improvable and worse than for the other GNSS.

In the following example, the satellite products of WUM (orbit, clock, biases) are used in the conventional model and uncombined model with three frequencies. Note that the corresponding ANTEX file (atx14.atx) does not contain corrections for the frequencies of Galileo and BeiDou for the receiver of DJIG (SEPT POLARX5). The GPS PCOs and PCVs are applied instead.

The station DJIG provides observations on three frequencies for GPS, Galileo, and BeiDou and two frequencies for GLONASS (table 6.1). Since WUM products do not enable ambiguity fixing, the inclusion of BeiDou into the float solution is investigated. For this reason, upper-case letters generally indicate the GNSS combinations in this section, although no ambiguity
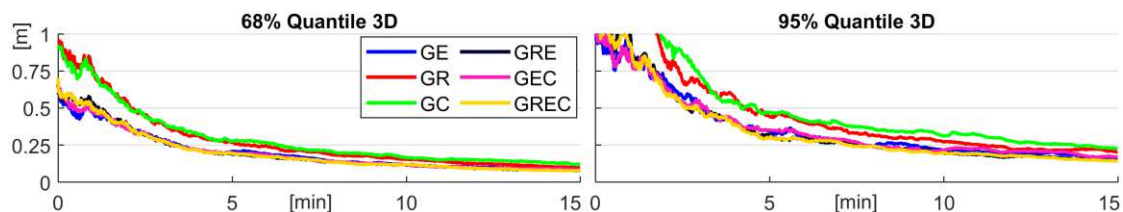
Figure 6.19: The 68% and 95% quantile of the 3D position difference using different GNSS combinations in the conventional model for the station DJIG on December 30 and 31, 2020

fixing is performed.

Figure 6.19 shows the 68% and 95% quantile of the 3D position difference for various PPP solutions calculated with different GNSS combinations and the conventional model. The corresponding graphic for the uncombined model looks quite similar. While GR and GC perform similarly, GE performs significantly better and is comparable to the solutions using GRE, GEC, and GREC. Adding GLONASS or BeiDou to GE (GRE or GEC) slightly improves the quantiles. Note that the performance (e.g., of the GRE solution) is comparable to the use of TUG products previously presented (section 6.3).

GNSS	(1)		(2)		(3)		(4)	
	IF	UC	IF	UC	IF	UC	IF	UC
GE	6.48	6.65	12.11	13.16	12.38	12.74	7.45	8.10
GR	8.63	8.55	15.26	16.84	16.50	16.35	8.86	9.31
GC	9.08	7.50	22.11	13.68	17.89	15.26	10.55	8.54
GRE	6.66	6.86	8.42	8.95	12.23	12.18	6.79	6.97
GEC	6.22	5.93	12.63	11.05	12.42	11.52	7.36	6.61
GREC	5.78	5.88	9.47	6.51	12.05	10.73	6.73	6.01

Table 6.8: The performance of different GNSS combinations for the station DJIG on December 30 and 31, 2020. The column blocks list the following values for the conventional (IF) and uncombined model (UC):
(1) Average convergence (2D < 10cm) time [min]
(2) Percentage of solutions without convergence in 15 minutes [%]
(3) Median 3D position error of all epochs [cm]
(4) Average 3D position error after 15 minutes [cm]

Table 6.8 exhibits some differences between the solutions of GE, GRE, GEC, and GREC. Altogether GREC performs best with the best statistics in nearly all regards. Furthermore, adding GLONASS or BeiDou (GRE or GEC) usually slightly improves the results compared to the GE solution.

Note that the uncombined model does not outperform the conventional model in all GNSS combinations in table 6.8. Their statistics are predominantly quite similar. However, the uncombined model performs much better with BeiDou observations added into the PPP solution. For example, the GEC solution's average convergence time and percentage of solutions without convergence are significantly lower with the uncombined model. Furthermore, the GREC solution of the uncombined model performs better than the GREC solution of the conventional model in all regards in table 6.8.

In addition to the number of satellites, the size of the code residuals is an explanation for shown behavior when combining various GNSS in a PPP solution. For example, in the conventional model, the code residuals have the following standard deviations: Galileo 0.459 m, GPS 0.654 m, GLONASS 0.995 m, BeiDou 1.127 m. The corresponding code residuals' biases are in the size of 2-5 cm and negligible. Therefore, the observation model fits worst for BeiDou and GLONASS. This may be a result of the GLONASS FDMA technique and the inhomo-

geneous character of the BeiDou system. Furthermore, the satellites' orbit and clock quality is usually lower for BeiDou and GLONASS than for GPS and Galileo, which is reflected in the residuals and PPP solutions.

In the case of the uncombined model and contrast to the conventional model, adding Bei-Dou observations increases the performance more than adding GLONASS observations. This behavior could be because the observation model of the uncombined model is not entirely adapted for the FDMA technique of GLONASS. For example, the estimation of the receiver DCBs does not consider the differing frequencies of the satellites.

A refinement of the observation model for BeiDou considering the in-homogeneous character of the BeiDou system (e.g., weighting depending on satellite type) and additional error sources might improve the results. Furthermore, it is essential (but not always straightforward) to apply the same definitions for BeiDou as during the computation of the satellite product. In the future, ambiguity fixing with BeiDou should be investigated with suitable satellite products.

Despite the challenging nature of BeiDou observations due to its rapid development and system characteristics, the inclusion of BeiDou causes a slight improvement in the PPP results. Typically, adding BeiDou to GPS or Galileo improves the results similarly or more than adding GLONASS. Furthermore, the PPP solution using observations from all four GNSS performances best due to an increased number of satellites (up to 30 or 40).

6.7. Real-time results

This section provides a short insight into real-time results achievable with the introduced PPP processing schemes. For this purpose, the satellite orbits, clocks, and biases from the real-time correction streams of CNES are applied instead of satellite products available in post-processing. Usually, the mentioned real-time corrections have an update rate of five seconds. Keep in mind that the main focus of this thesis lies on post-processed satellite products, and the PPP models are not optimized for real-time applications. Therefore, more careful handling of real-time corrections considering their characteristics might improve the results.

Generally, the accuracy of real-time correction streams can be considered lower than that of post-processed satellites products due to obvious reasons. Furthermore, real-time corrections streams are not as consistent, show outages, and occasionally lack corrections. The stream might not provide specific corrections for some satellites or periods. In the present case, the stream does not contain any phase biases (December 30 and 31, 2020). Consequently, only the float solution's results are presented for this test period. The real-time performance of the fixed solution is illustrated using observation data from December 24, 2020.

The correction streams of CNES only provide biases for Galileo X-signals during the chosen test period (table 6.9). In the presented test case, these signals are observed from the fol-

GNSS	Code Biases
GPS	C1C C1W C1X; C2C C2S C2L C2X C2W; C5Q C5X
GLONASS	C1C C1P; C2P C2C
Galileo	C1X; C5X; C6X; C7X; C8X
BeiDuo	C1P C1X; C2I; C5X; C6I; C7X

Table 6.9: Code biases included in the correction streams of CNES (e.g., SSRA00CNE0) during the chosen test period

lowing subset of stations: ASCG, CIBG, GAMB, KOKV, LMMF, MAYG, OWMG, RGDG, UFPR, and UNB3. The real-time tests are restricted on these ten stations and the conventional PPP model because it is not straightforward to obtain and apply a precise global ionosphere model in real-time. Furthermore, GPT3 is used as troposphere model to ensure real-time capability. Despite that, the same processing settings as described in section 6.2 and table 6.1-6.3 are used. Note that CNES provides an archive for their corrections streams used in the processing[35].

	Stream	TUG
Average convergence time (2D <10cm) [min]	7.59	7.52
Percentage of no convergence [%]	18.20	12.27
Median 3D position error of all epochs [cm]	15.49	14.05
Average 3D position error after 15.00 minutes [cm]	9.32	7.98

Table 6.10: The float solution's performance using stream corrections or TUG products on December 30 and 31, 2020

Table 6.10 presents the average convergence time, percentage of convergence periods without convergence, and accuracy of the float solutions using either streams corrections or TUG products on December 30 and 31, 2020. The real-time float solution performs nearly as well as using TUG products: The average convergence time is similar, and the real-time coordinate accuracy is slightly lower (1-1.5 cm). Also, the size and behavior of the float solution's code residuals are comparable for both PPP solutions. However, about 6 % more convergence periods of the real-time solution do not reach convergence (2D <10cm) within 15 minutes since the stream's corrections are less consistent.

Figure 6.20 shows the 68% and 95% quantiles of the ZTD difference of the ten stations for December 30 and 31, 2020, using stream corrections or TUG products in the PPP solution. The IGS troposphere product available after a few weeks with an accuracy of a few

---

[35] PPP-WIZARD: http://www.ppp-wizard.net/
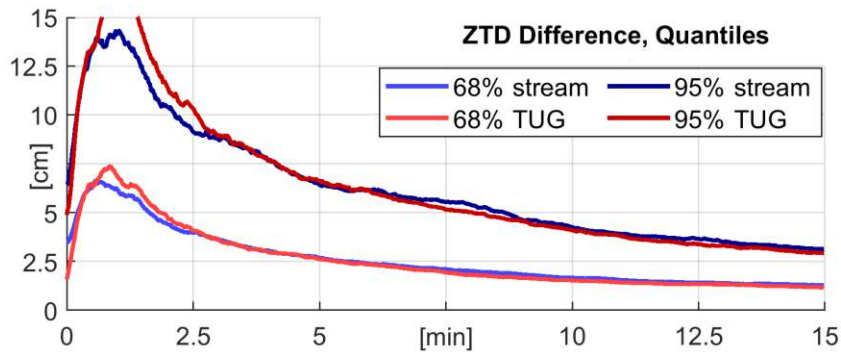
Figure 6.20: Quantiles of ZTD difference using stream corrections or TUG products

millimeters is used as reference like in section 6.4.

Although GTP3 is applied instead of VMF3 and real-time corrections instead of post-processed satellite products, the real-time estimation of the ZTD performs similarly to the estimation in post-processing using TUG products. In figure 6.20 the real-time 68% and 95% quantile of the ZTD difference perform better during the convergence period. However, the real-time ZTD difference is slightly less accurate after convergence.

The standard deviation of the ZTD difference (stream: 7.92 cm and TUG: 7.92 cm) is identical with negligible biases in the size of a few millimeters (0.42 cm and 0.44 cm). Note that the standard deviation's magnitude is mainly driven by the convergence of the ZTD in the first minutes explaining its size. After five to ten minutes, it is possible to estimate the ZTD in real-time with an accuracy of a few centimeters or below (figure 6.20).

The results presented in this section are restricted to Galileo X-signals due to the availability of code biases in the correction streams of CNES. The subset of stations observing Galileo X-signals achieves worse results when applying TUG products than in the previous sections. The convergence period and accuracy of the coordinates and ZTD difference are longer and lower, respectively. This fact matches the author's experience that PPP with Galileo X-signals (e.g., C1X, C5X) usually performs worse than with C and Q-signals (e.g., C1C and C5Q). A possible explanation is that better-performing Septentrio receivers do not observe Galileo X-signals (section 7.7).

Average time to correct fix [min]	5.99
Median time to correct fix [min]	4.87
Percentage of no fix [%]	18.29
Median 3D position error after 15.00 minutes	4.40
Average 3D position error after 15.00 minutes	10.12

Table 6.11: The fixed solution's performance using stream corrections on the first part of December 24, 2020

Observation data from December 24, 2020 (doy 359, 2020) is processed to illustrate the performance of the fixed solution applying real-time corrections. Unfortunately, the stream

does not provide any correction data from about 15:00 h on this day. For this reason and to keep things simple, only the first part of the day is used (from 00:00 to 12:00 hours).

Table 6.11 shows the average and median time to fix, the percentage of convergence periods without a correct fix in the first minutes, and the accuracy of the 3D position difference after 15 minutes statistics for this period. On average, the TTFF is completed after about five minutes. Almost 18% of the convergence periods do not achieve a correct fix within 15 minutes. If the position is correctly fixed, a 3D accuracy of about 4 centimeters is reached.

A comparison with the post-processed fixed coordinate's results must be interpreted with caution because the results presented in section 6.3.2 are based on another station set and time period. However, the TTFF is elongated by about two to three minutes with a comparable percentage of converge periods without a correct fix. Furthermore, the accuracy of the fixed solution is slightly lower.
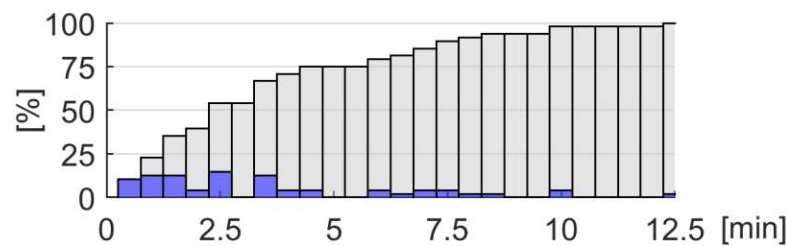
Figure 6.21: The real-time TTFF's distribution for the station UFPR on the first part of December 24, 2020

Figure 6.21 shows the TTFF's distribution for the best-performing station UFPR (Curitiba, Brazil) within the first part of December 24, 2020. Blue bars indicate the percentage of convergence periods achieving a correct fix at a specific point in time, and grey bars the percentage of convergence periods already correctly fixed until this point in time. The majority of TTFFs take place within the first few minutes. After 5 minutes 75% of the convergence periods have achieved a correct fix and nearly 100% after 10 minutes. This shows that a TTFF of a few minutes is feasible in real-time.

The presented examples show that the real-time float solution's coordinate and ZTD results are comparable to applying post-processed satellite products in the PPP solution. The TTFF is elongated by a few minutes (e.g., two to three). These findings suggest that the quality of the real-time satellite orbits and clocks is sufficient for float PPP. However, the phase biases' quality is lower, which is exhibited by the performance of the fixed solution.

Additionally, experience has shown that the PPP results applying real-time correction streams show more variations between different days. In some periods, the PPP performance is considerably worse than in other periods. This is especially true for the fixed solution and most likely results from the real-time correction stream's changing quality (e.g., accuracy, missing corrections). Furthermore, the real-time stream is less stable (e.g., outliers) and has outages.

The real-time coordinate and ZTD performance might improve with optimized handling of real-time correction streams. For example, better handling of outliers or considering the varying quality of the corrections (e.g., GNSS weighting) could lead to better results. It is expected that real-time corrections streams will reach the quality level (e.g., phase biases and stability) of post-processed satellite products in near future. Furthermore, global high-quality ionosphere models available in real-time will enable data processing schemes favouring the uncombined model with ionospheric constraint.

7. Prospects, Problems, and Potential

This chapter discusses several issues related to current limitations and further potential for improving the PPP technique. In this context, various examples are presented to highlight these challenges and opportunities. Therefore, the conventional PPP model is mainly used since it is more illustrative due to fewer parameters and dimensions. For example, only one set of ambiguities or residuals instead of two or three must be studied. Furthermore, often observation data with an interval of 30 seconds is used in the processing for similar reasons. However, the findings are also valid for the uncombined model and other observation intervals.

7.1. Satellite attitude handling

During the calculation of a PPP solution, the user needs to apply the same attitude model used during the computation of the utilized satellite products. Otherwise, error sources like satellite phase center corrections and Phase Wind-Up are not correctly modeled. These error sources are especially relevant for the precision of the phase observation and, therefore, the success of the fixing process.

Figure 7.1 shows the fixed coordinates of three different PPP solutions calculated with TUG products and observation data of the IGS station NKLG on January 1, 2020, starting at 0h (observation interval 1 second). The PPP solution shown in the left part of the figure uses the IGS convention for modeling the satellites' orientation without involving the cylindrical model to detect satellites in eclipse season (section 3.1.4). Due to the eclipsing GPS satellite 26 and discrepancies in the modeling of the satellite's orientation between the network and user side, the fixing is jeopardized, and even after 15 minutes not successful. If G26 was the reference satellite selected in the fixing process, the situation would be even worse.

Figure 7.2 illustrates the location of G26 at the beginning of the processing. The direction of view is along the negative z-axis of the ECEF coordinate system in the left part of figure
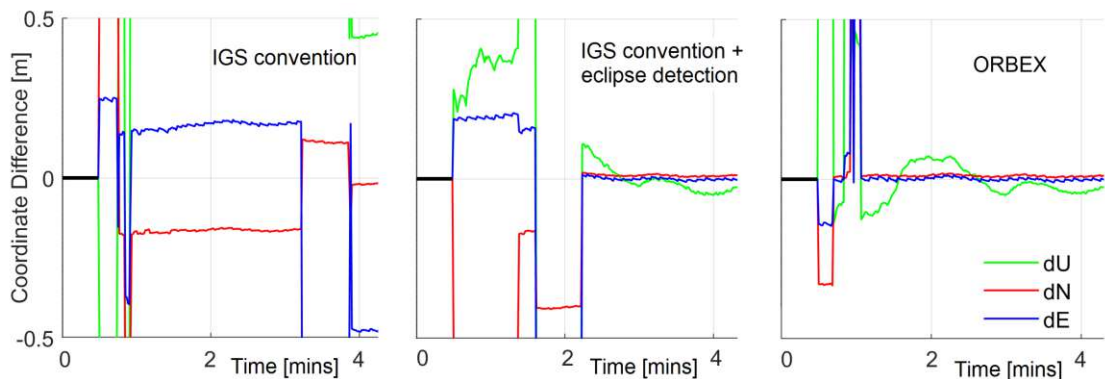
Figure 7.1: Three fixed solutions with different handling of the satellite attitude. The shown UTM coordinate differences refer to the final IGS coordinates of the station NKLG.
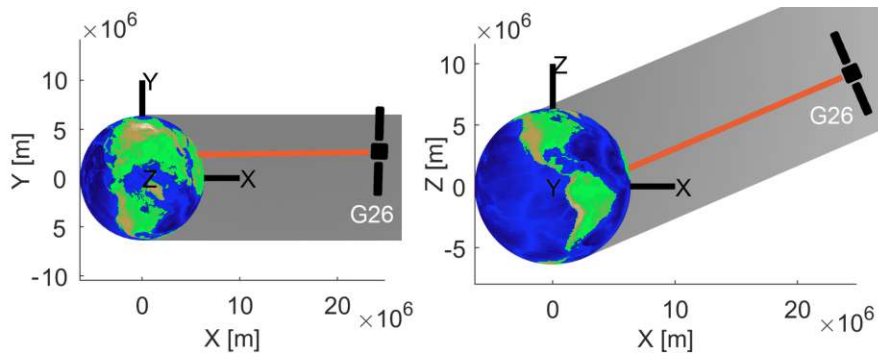
Figure 7.2: The location of the eclipsing satellite G26, the direction to the Sun (orange), and the cylindrical model for the Earth's shadow (grey) on January 1, 2020 at 0h

7.2 and along the positive y-axis in the right part. The Earth's shadow is represented in grey. Furthermore, the orange line illustrates the direction from the satellite G26 to the Sun. Note that the depiction of the GNSS satellite is not true to scale. Obviously, the satellite G26 is in the Earth's shadow.

The PPP solution presented in the middle part of figure 7.1 uses the cylindrical model of the Earth's shadow (section 3.1.4), which detects and excludes the eclipsing satellite G26. After 2 minutes and 14 seconds, the position is correctly fixed, a significant improvement to the previous PPP solution.

On the other hand, the PPP solution shown in the right part of figure 7.1 applies the corresponding ORBEX file from TUG providing satellite attitude entries in addition to the orbits, clocks, and biases. The consistent and accurate satellite orientation significantly reduces the TTFF to 1 minutes and 4 seconds without excluding the satellite G26.

The presented example illustrates that satellites in eclipse season should be detected to avoid discrepancies in the satellites' orientation if no attitude information is provided by the applied satellite products. However, excluding eclipsing satellites reduces the number of satellites and lowers the chances of a correct fix. The attitude entries of ORBEX files strengthen the observation model and improve the convergence of the fixed solution. All tests showed an improvement in the TTFF and the 3D accuracy of the fixed solution. Apart from that, there are no notable differences in the float solution because the estimated float ambiguities can absorb imperfections in the modeling of the satellite orientation. Currently, more institutions start to provide ORBEX files and attitude information in addition to their satellite products (Loyer et al., 2021). This development will further improve the performance of PPP-AR.

7.2. Cycle slips

PPP heavily relies on the precision of the phase measurements and the stability of the ambiguities to achieve its final accuracy. Usually, the presented cycle slip detection method

reliably detects almost all cycle slips (section 4.4.1). However, the PPP solution can tolerate unusable phase observations due to cycle slips only up to a certain level. If the number of usable phase observations and constant ambiguities gets too low, the coordinates' accuracy diminishes to a code-only solution. Of course, in this case, the calculation of a fixed solution is not feasible at all.
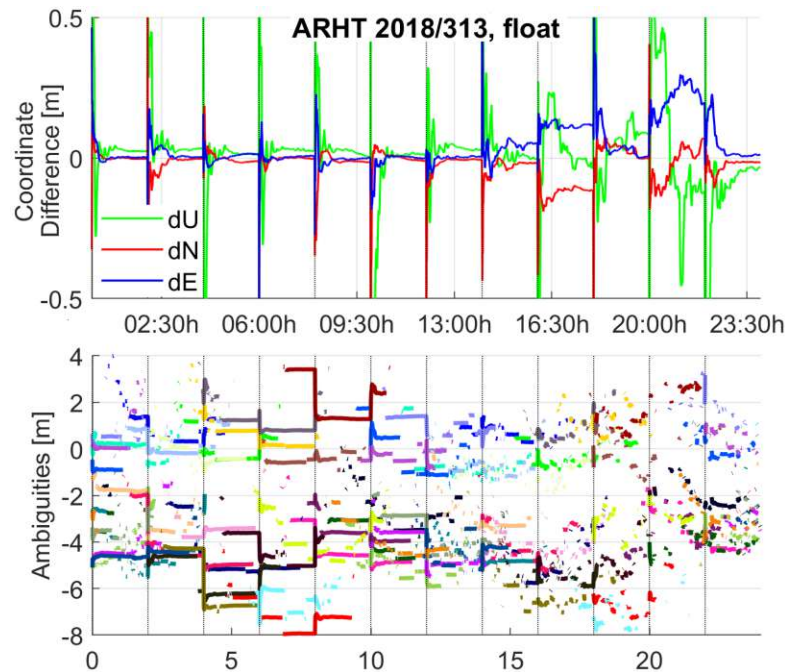
Figure 7.3: Float coordinates and ambiguities for ARHT on doy 313, 2018

Figure 7.3 shows the float solution's coordinates (top) and float ambiguities (bottom) of a PPP solution for IGS station ARHT (McMurdo Station, Antarctica) on doy 313, 2018. To make this example easily understandable, the presented PPP solution uses only GPS observations in the conventional model. However, the shown behavior is independent of the number of processed GNSS and the used PPP model.

During the first half of the day, phase observations are excluded from time to time due to cycle slips, perceptible in discontinuities of the float ambiguities. In the afternoon, the number of cycle slips increases significantly, clearly visible in the behavior of the float ambiguities. In the evening, no stable ambiguity is recognizable in the lower part of figure 7.3.

The float coordinates and their accuracy reflect the behavior and reliability of the phase observations. In the first part of the day, the number of cycle slips is tolerable, resulting in a reasonable coordinate solution (top part of figure 7.3). In the evening, the PPP solution is practically a code-only solution providing an accuracy at the decimetre level. Comparably, it is possible to fix the ambiguities to their correct integer value only in the first part of the day. It is not easy to find an explanation for this behavior, but cycle slip repair method might

help to improve the results in this case.

Generally, the LLI bit (section 4.4.1) indicates cycle slips and is typically used to exclude marked phase observations. Experience showed that the LLI bit can be ignored if a reliable cycle slip detection method is used. For example, some observation files contain epochs, where all phase measurements are marked without reason. While a stable float solution can handle a complete reset of all ambiguities, the fixed solution is ruined in any case, and the fixing has to be restarted.

7.3. Float versus fixed solution

The integer fixing of the ambiguities reduces the convergence time and increases the accuracy of coordinates. Therefore, the fixed solution usually outperforms the float solution. However, the float solution is preferable to the fixed solution in some cases.

Once the ambiguities are correctly fixed, the fixed solution has reached its final precision, which will then stay at the same level. The float solution converges slower but, on the other hand, does not abruptly stop increasing the accuracy of the estimated parameters. In this way, the float coordinates might be more accurate than the fixed coordinates at some point. A user interested in extremely precise coordinates, for example, might calculate a float PPP solution over many hours and ignore the fixed solution.
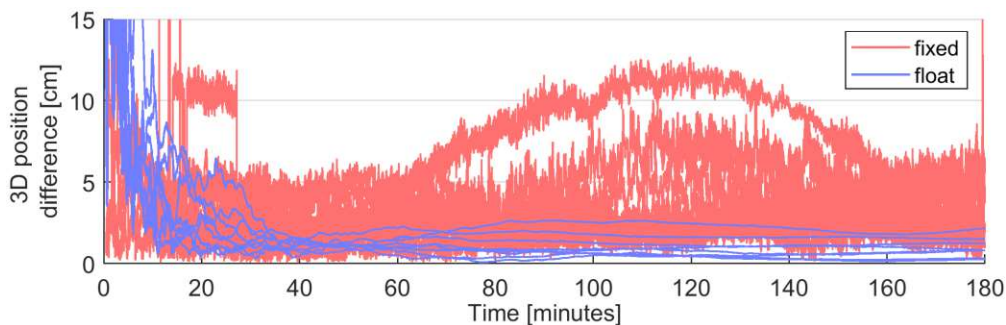
Figure 7.4: Float and fixed coordinates for the station YEL2 on December 31, 2020

To illustrate this point, observation data from the station YEL2 (Yellowknife, Canada) on December 31, 2020, is processed with the conventional model and the settings described in section 6.2. The test case in the last chapter already dealt with this station, but for this example a reset of the solution is performed every 3 hours. Figure 7.4 shows the resulting 3D coordinate difference for the corresponding eight convergence periods. The red lines represent the fixed coordinates, the blue lines the float coordinates. Note that the upper limit of the y-axis is only 15 cm.

At this high-precision level, it gets clear that the fixed coordinates are noisier than the float coordinates due to unmodeled error sources that are not absorbed by other estimated parameters like in the float solution. Note that this noise of the 3D position difference is only at the size of 2-3 millimeters and only visible due to the large scale of figure 7.4 and

the observation interval of 1 second. Apart from that, the fixed coordinate solution proves to be very stable, and only one time series of fixed coordinates deviates significantly for a longer period in figure 7.4. This probably results from an imperfection in the fixed solution's observation model (e.g., satellite orientation or ANTEX corrections) in this period, which is absorbed from other parameters in the float solution (e.g., ambiguities).

Furthermore, figure 7.4 allows a comparison of the float and fixed coordinate accuracy. After about 30 minutes the float coordinates are more precise and stable than the fixed coordinates. At a certain point (e.g., 40 minutes), the float solution's accuracy stays at the same level and reaches a 3D position accuracy of 1-2 cm or even at the millimeter level.

Beyond that, the float solution is more robust in specific cases since the fixed solution relies much more on the phase observations. If the phase measurement is interrupted, the estimation of the float ambiguities and fixing process has to be restarted. For example, all (phase) observations may be unusable in a specific epoch or period (e.g., cycle-slips, data holes). In that case, the fixed solution has to be completely recalculated.

On the other hand, the float solution possibly handles such adversities when the parameters are already reliable estimated in the Kalman filter process after a decent convergence time. Furthermore, the filter can rely only on code observations for a few epochs. The restart of (all) float ambiguities may not lead to a loss of coordinate accuracy.
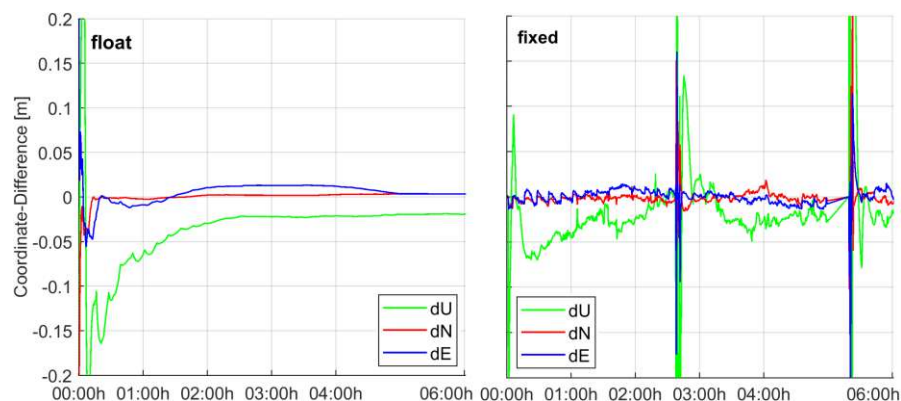
Figure 7.5: Float and fixed coordinates for the IGS station AREG on January 1, 2020. At 02:37h and between 05:00h and 05:19h data gaps occur.

Figure 7.5 shows the float and fixed coordinates for the IGS station AREG (Arequipa, Peru) on January 1, 2020, for the time period between 0h and 6h. In the presented test case, GPS and Galileo observation data with an interval of 30sec data was used in the conventional model with the satellite products from CODE. For one epoch at 02:37h and the period between 05:00h and 05:19h, data gaps occur, and the RINEX file does not contain any observations.

In both cases, cycle slips are detected for all satellites after the data gaps. Therefore, the float ambiguities are reset, and the fixed solution has to be recalculated clearly visible in the fixed coordinate solution (right part of figure 7.5). On the other hand, the float coordinates

are unaffected, although the estimation of the float ambiguities is restarted because the Kalman Filter preserves the parameters' estimates.

7.4. Multipath

Figure 7.6 shows three skyplots of the IGS station REYK (Reykjavik, Iceland) for February 2020. The left skyplot focuses on GPS satellites, the skyplot in the middle concentrates on GLONASS satellites, and the right skyplot on Galileo satellites. It is apparent from figure 7.6 that GPS covers the sky not as well as GLONASS and, especially, Galileo, due to the approximately daily orbit repetition period. Figure 7.6 also shows that the north hole is considerably smaller for GLONASS resulting from the higher inclination of the satellite orbits.
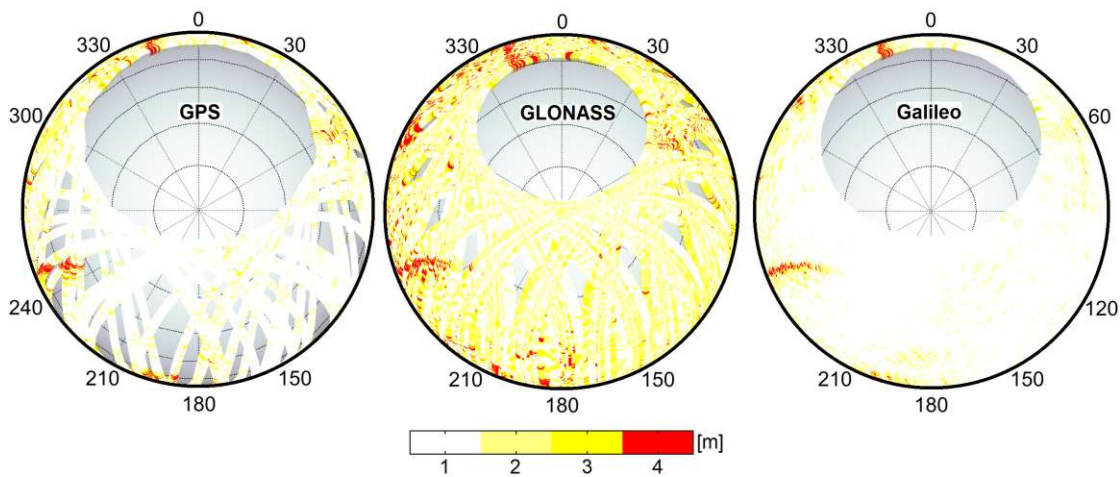
Figure 7.6: Skyplot of the IGS station REYK for February 2020 for GPS (left), GLONASS (middle) and Galileo (right side). The satellite tracks are color-coded according to the size of the float code residuals for a PPP solution using the conventional PPP model and CODE products.

The satellite tracks in figure 7.6 are color-coded based on the size of the float code residuals resulting from a PPP solution using GPS, GLONASS, and Galileo observations and CODE products in the conventional PPP model. Generally, the GLONASS residuals are larger than those from GPS and Galileo, motivating a weighting of the observations based on the GNSS (section 7.8).

Furthermore, we can observe certain regions where an increased number of higher residuals (red) show up. These regions emerge for all GNSS independently of the time period. Therefore, they most likely originate from multipath due to their size of several meters and explain the unsatisfactory performance of the PPP solution for the station REYK.

Unfortunately, the magnitude of the code residuals in these regions is too small for detecting the faulty observations with the simple observed minus computed check presented in section 4.4.1. Beyond that, the application of exclusion regions was tested to determine all satellites observed in a region of the skyplot with pronounced multipath and exclude

the observations from these satellites. However, this approach was ineffective because the exclusion regions' boundary, shape, and size are difficult to define. Potentially, too many satellites are excluded, weakening the PPP solution's performance in this way. Furthermore, this approach has to be adjusted to each site and requires long-term observation data and preparation.

Furthermore, various detection methods based on the MP LCs presented in section 2.4.6 were examined. Unfortunately, no effective application of the MP LCs and, in particular, thresholds could be found for the variance or absolute values (after subtracting the mean) of the MP LCs of the last few epochs. Also, a weighting scheme based on the MP LC as proposed by Seepersad and Bisnath (2015) did not improve the solution.

However, since this thesis focuses on high-quality data of static geodetic receivers (e.g., upmarket antennas), the amount of multipath can usually be assumed insignificant. Furthermore, the observed minus computed check detects major multipath events. When adapting the presented PPP processing schemes on low-cost data, deeper investigations of multipath detection have to be performed.

7.5. Different IF LCs

The 3+ frequency GNSS landscape opens new opportunities for building the IF LC in the conventional PPP model. Moreover, it is also possible to use a 3-frequency IF LC in the processing. Since all Galileo satellites provide signals on five frequencies, the resulting options are tested in a Galileo-only solution.

The IGS station BRST (Brest, France) and a three-day period from August 9 to 11, 2020 (doy 222-224) with a reset of the solution very 45 minutes are selected. This station is equipped with a Trimble Alloy receiver providing Galileo X observations on all frequencies (E1, E5, E5a, E5b, and E6). The post-processed biases from CNES are used in the processing. They provide code and phase corrections for all Galileo X signals and allow fixing any signal combination. Note that to the author's knowledge, no phase biases for E5 are included in general. Since these biases must be used together with the GFZ rapid orbits and clocks for reasons of consistency, the presented solutions have a short latency (e.g., the next day).

7.5.1. 2-frequency IF LCs

The five Galileo frequencies (E1, E5, E5a, E5b, and E6) allow ten options to build an IF LC (equations 2.19 and 2.20) in the conventional PPP model. Table 7.1 lists all these possibilities with the corresponding coefficients a_i of the LC and resulting noise amplification factor $\tilde{n}$ calculated with equation 2.10. Obviously, the listed 2-frequency Galileo IF LCs differ considerably in their noise amplification factor.

Figure 7.7 shows a box plot of the float convergence (2D < 10cm) for these ten IF LCs. To create this plot, the convergence time was set to 45 minutes for convergence periods that

f_1	f_2	a_1	a_2	$\tilde{n}$	(1)	(2)	(3)
E1	E5	2.3380	1.3380	2.69	20.00	10.10	-
E1	E5a	2.2606	1.2606	2.59	20.00	7.14	22.50
E1	E5b	2.4220	1.4220	2.81	22.50	6.38	25.50
E1	E6	2.9312	1.9312	3.51	22.00	7.94	23.00
E5a	E5	38.0850	39.0850	54.57	44.00	161.75	-
E5a	E5b	18.9199	19.9199	27.47	43.00	39.32	-
E5a	E6	5.5104	6.5104	8.53	36.50	13.45	-
E5b	E5	39.5849	38.5849	55.28	-	269.60	-
E5b	E6	8.1858	9.1858	12.30	34.50	16.42	-
E5	E6	6.6117	7.6117	10.08	40.50	30.95	-

Table 7.1: All options of Galileo IF LCs with the corresponding coefficients a_i and noise amplification factor $\tilde{n}$. Furthermore, (1) the median float convergence time [min], (2) median 3D accuracy after 45 minutes [cm], (3) and median TTFF [min] are listed for the presented test case.
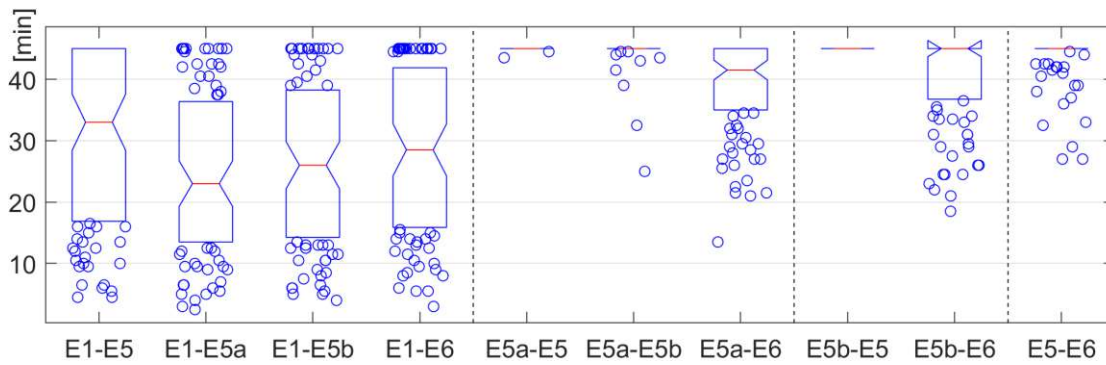
Figure 7.7: Box plot of the float convergence for all options of Galileo 2-frequency IF LCs

did not converge at all. In each box, the central red mark indicates the median convergence time in minutes. The bottom and top edges of the box indicate the 25th and 75th percentiles, respectively. Convergence times outside the 25th and 75th percentile are plotted individually using blue circles. The vertical dashed lines in figure 7.7 correspond to horizontal lines in table 7.1 indicating another first frequency in the LC.

It is apparent from figure 7.7 that IF LCs without the E1 frequency show a poor float convergence. This can be explained by the closeness of the E5, E5a, E5b, and E6 frequency (table 2.1) resulting in much higher noise amplification factors compared to IF LCs containing the E1 frequency (table 7.1). Note that nearly no convergence periods of the E5a-E5, E5a-E5b, and E5b-E5 are less than 45 minutes due to their enormous noise amplification factors from about 27 to 55. Therefore, only IF LCs containing the E1 frequency are considered in the following.

The right part of table 7.1 presents the median float convergence time for all convergence periods reaching convergence. Furthermore, the table lists the median 3D position difference

after 45 minutes. The IF LCs built from E1-E5a and E1-E5 converge slightly faster than the E1-E6 and E1-E5b combination (20 minutes vs. 22 - 22.5 minutes). However, the median 3D accuracy after 45 minutes of the E1-E5 is considerably worse (10.1 cm). That of the E1-E5b combination is slightly better (6.4 cm) than for the other two remaining IF LCs containing the E1 frequency (7.1 and 7.9 cm). In this test case, the IF LCs built from E1-E5a and E1-E5b show the best float performance combining satisfactory convergence times (for a single GNSS solution) and a high 3D accuracy after 45 minutes.

The far-right column of table 7.1 presents the median TTFF for these combinations ranging from 22.5 to 25.5 minutes. Note that due to missing phase biases for E5, no fixed solution can be calculated for the E1-E5 IF LC. Although the E1-E5a combination has the lowest median TTFF, about 20% of the convergence periods achieve no correct fix at all (not listed in table 7.1). For the IF LCs consisting of E1-E6 and E1-E5b, only about 12% of the convergence periods achieve no correct fix. Therefore, the IF LC built from the E1 and E6 frequencies performs best in the fixed solution because it has the shorter median TTFF from these two combinations.

The presented test case shows that there are varieties in convergence and accuracy for different IF LCs resulting from varying noise amplification factors. The findings might differ for other receiver types or satellite products. However, other IF LCs containing the E1 frequency should be considered in addition to the standard E1-E5a combination in the Galileo case if the satellite product allows their processing and fixing. In the presented test case, they are at least an equal alternative. Furthermore, the processing of multiple 2-frequency IF LCs together in one PPP solution should also be considered.

7.5.2. 3-frequency IF LC

Besides new combinations for the conventional PPP model presented in the last section, it is also possible to form and process a 3-frequency IF LC in the 3+ GNSS frequency landscape. L. Pan et al. (2019) provide the following formulas to calculate the coefficients of such a 3-frequency IF LC under the condition of minimum noise, eliminating the first-order ionospheric delay, and unchanged geometry range. These equations use the squared ratio of frequencies γ_{ij} provided in equation 2.17.

$$a_1 = \frac{\gamma_{12}^2 + \gamma_{23}^2 - \gamma_{12} - \gamma_{23}}{2(\gamma_{12}^2 + \gamma_{23}^2 - \gamma_{12}\gamma_{23} - \gamma_{12} - \gamma_{23} + 1)} \tag{7.1}$$

$$a_2 = \frac{\gamma_{23}^2 - \gamma_{12}\gamma_{23} - \gamma_{12} + 1}{2(\gamma_{12}^2 + \gamma_{23}^2 - \gamma_{12}\gamma_{23} - \gamma_{12} - \gamma_{23} + 1)} \tag{7.2}$$

$$a_3 = \frac{\gamma_{12}^2 - \gamma_{12}\gamma_{23} - \gamma_{23} + 1}{2(\gamma_{12}^2 + \gamma_{23}^2 - \gamma_{12}\gamma_{23} - \gamma_{12} - \gamma_{23} + 1)} \tag{7.3}$$

With the coefficients a_i from the equations 7.1 to 7.3, the 3-frequency IF LC is built for the code and phase observation with equation 7.4 and 7.5, respectively.

$$P_{3IF} = a_1 P_1 + a_2 P_2 + a_3 P_3 \tag{7.4}$$

$$L_{3IF} = a_1 L_1 + a_2 L_2 + a_3 L_3 \tag{7.5}$$

The resulting ten different combinations for five Galileo frequencies are listed in table 7.2 with their LC coefficients a_i and noise amplification factor $\tilde{n}$. Similar to the last section and the two frequency case, the noise amplification factor of the 3-frequency IF LCs differs considerably. Note that the horizontal lines in table 7.2 correspond to vertical dashed lines in figure 7.8 indicating another first frequency in the LC's formation.

f_1	f_2	f_3	a_1	a_2	a_3	$\tilde{n}$	(1)	(2)
E1	E5	E5a	2.2929	-0.5589	-0.7340	2.47	20.46	6.57
E1	E5	E5b	2.3730	-0.7796	-0.5934	2.57	22.02	5.79
E1	E5	E6	2.3787	-1.2461	-0.1327	2.69	20.28	6.13
E1	E5a	E5b	2.3149	-0.8363	-0.4787	2.51	21.11	5.77
E1	E5a	E6	2.2691	-1.2446	-0.0245	2.59	22.21	6.35
E1	E5b	E6	2.4888	-1.2354	-0.2534	2.79	22.65	5.65
E5	E5a	E5b	0.5833	-19.2059	19.6266	27.46	40.19	40.82
E5	E5a	E6	-2.0368	-3.8129	6.8497	8.10	35.30	11.43
E5	E5b	E6	-4.7582	-2.2948	8.0530	9.63	34.46	12.41
E5a	E5b	E6	-4.8279	-1.0139	6.8418	8.43	35.75	11.23

Table 7.2: All options of Galileo 3-frequency IF LCs with the corresponding coefficients a_i and noise amplification factor $\tilde{n}$. Furthermore, (1) the average float convergence time [min] and (2) median 3D accuracy after 45 minutes [cm] are listed for the presented test case.
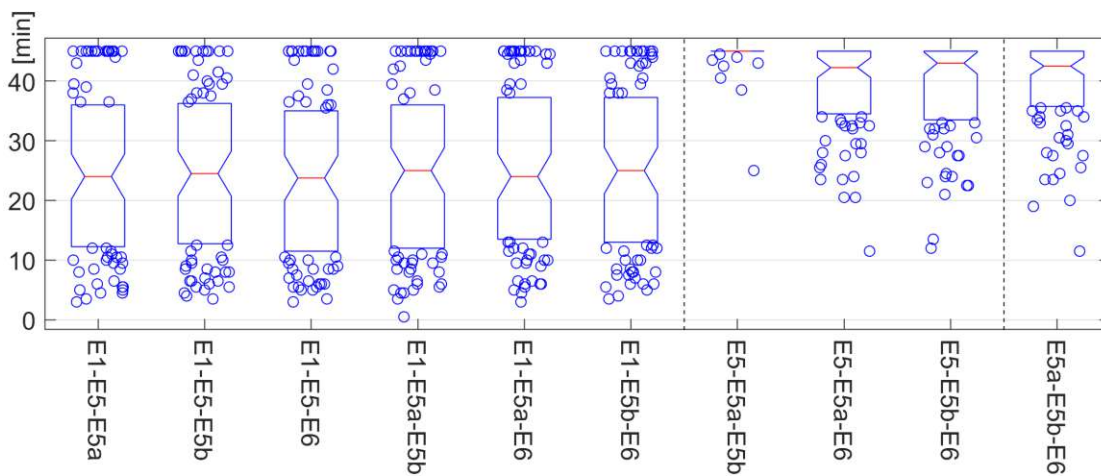
Figure 7.8: Box plot of the float convergence for all options of Galileo 3-frequency IF LCs

Figure 7.8 presents the bar plot of float convergence for all ten Galileo 3-frequency IF LCs, created in an identical approach as in the last section. Since 3-frequency IF LCs containing the E1 frequency have a lower noise amplification factor ranging from 2.47 to 2.79 than other 3-frequency IF LC, they perform best, resulting in an average float convergence time ranging from 20 to 22.5 minutes. Furthermore, they show a comparable median 3D accuracy after 45 minutes of around 6 centimeter. In the presented test case, all 3-frequency IF LCs containing the E1 frequency perform similarly. However, the E1-E5-E6 combination shows the fastest float convergence, and the E1-E5a-E5b combination the highest median 3D accuracy after 45 minutes.

We can identify a second group using a combination of the E6 and E5, E5a, or E5b frequency. These 3-frequency IF LCs have a considerably higher noise amplification factor ranging from roughly 8 to 10. Therefore, they perform significantly worse in terms of convergence time and accuracy. Finally, the E5, E5a, E5b combination delivers poor results explained by the highest noise amplification factor (about 27).

Generally, we can see a strong connection between the noise amplification factor of the IF LC and the performance of the PPP solution. This can be used as an argument for the uncombined model's superiority and outstanding convergence behavior since its noise amplification factor equals one.

Compared to table 7.1 and the various options for 2-frequency IF LCs in the conventional model, the convergence time and accuracy of 3-frequency IF LCs are comparable or slightly better due to a similar or marginally smaller noise amplification factor. Note that due to the additional condition on minimum noise, a 3-frequency IF LC can have a smaller noise amplification factor than a 2-frequency IF LC. Therefore, the processing of a 3-frequency IF LC can be considered as an alternative. Although processing three frequencies, the computational effort is small because the observations of these three frequencies are converted into only one observation. Furthermore, PPP-AR with 3-frequency IF LCs can be investigated in the future.

However, 3-frequency IF LCs are not usable in the current multi-GNSS landscape because only the Galileo and BeiDou system provide open signals on at least three frequencies at all satellites. Note that only one missing observation (e.g., GPS L5) prevents the formation of a 3-frequency IF LC.

7.6. Troposphere modelling options

Generally, the estimation of the ZWD is correlated with the receiver clock error, height component, and ambiguities, and these parameters absorb imperfections in the handling of the tropospheric delay. Since it is typically not possible to model the wet tropospheric delay with sufficient accuracy the (residual) ZWD is usually estimated during a PPP solution.

However, VMF3 produces site-wise coefficients resulting in highly precise values for the hydrostatic and wet delay at selected stations. Based on this accurate troposphere model,

it might be advantageous for the PPP solution to omit the estimation of the ZWD and completely rely on the VMF3 values.

Three arbitrary IGS stations (contained in the VMF3 station list) and dates were selected (table 7.3). Two PPP-AR solutions were calculated for these stations using GPS and Galileo in the fixing process, CODE products, and the conventional PPP model. Furthermore, GLONASS observations were used in the float solution. The first PPP solution uses VMF3 and estimates the residual wet part of the tropospheric delay. On the other hand, the second solution completely relies on VMF3 and the modeled hydrostatic and wet delay without estimating a residual wet part. Only the fixed solution is studied in the following because the variations of the float solution resulting from these two troposphere modelling options are negligible.

Table 7.3 contains the average TTFF, 2D, and 3D position difference after 20 minutes for the PPP solutions resulting from the two different troposphere modelling options. The left value in each cell belongs to the PPP solution with estimating the residual ZWD, the right value to the PPP solution where no residual ZWD is estimated. We observe from this table that there is no significant variation in the accuracy of the horizontal position. However, the 3D position is slightly worse without estimating the residual ZWD because the height component is absorbing small imperfections of the troposphere model.

Station	ULAB	GRAZ	BRUX
Date	January 1, 2020	June 9, 2020	March 9, 2020
Average TTFF (2D < 5cm) [min]	3.13; 2.51	3.46; 3.29	2.17; 2.07
Average 2D accuracy after 20 min [cm]	1.00; 1.01	1.16; 1.12	1.06; 1.09
Average 3D accuracy after 20 min [cm]	1.85; 1.98	2.75; 2.86	2.11; 2.42

Table 7.3: Average TTFF and accuracy of the fixed solution for three arbitrary IGS stations and days with estimation (left value) and modeling (right value) of the ZWD using site-wise VMF3
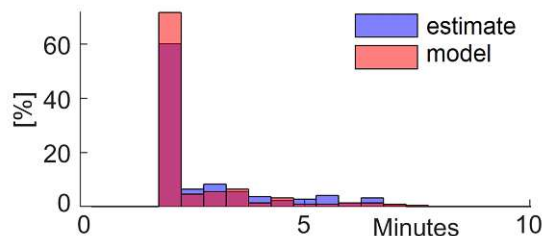

Figure 7.9: Distribution of the TTFF when estimation or modeling the ZWD using site-wise VMF3 for the stations listed in table 7.6

On the other hand, the omission of the ZWD estimation reduces at least slightly the TTFF when looking at the average TTFF values in table 7.3. Furthermore, figure 7.9 illustrates this

improvement by presenting the distribution of the TTFF of all convergence periods for these three stations and days. Without estimating the residual ZWD, the percentage of correct fixes right after the start of the fixing process (2 minutes) is increased from 60% to 70%.

This example shows that there is potential for reducing the TTFF with improved handling of the troposphere. However, highly precise tropospheric delays like the site-wise VMF3 or the IGS troposphere product are only available for certain locations. The grid-wise VMF3 for arbitrary sites using interpolation does not reach this level. Although a ray-tracing tool available on the VMF website[36] can be used for arbitrary sites, all these options are not available in real-time. Therefore, applying a PPP troposphere delay estimation from a nearby station or network available in real-time should be investigated to reduce the TTFF.

Since the precision of a high-quality troposphere model should be superior to the PPP solution in the first epochs of processing, the estimation of the ZWD could be started after some epochs of processing when the solution and its estimated parameters are stable enough. This could combine an improved convergence by reducing the correlation between the estimated parameters and avoiding the height component's deterioration. Alternatively and similar to the ionospheric constraint, it is possible to use a tropospheric constraint (Aggrey and Bisnath, 2019; Tomasz, 2015; R. Wang et al., 2019). In combination with the uncombined model with ionospheric constraint, this leads to the so-called atmospheric constraint.

7.7. Receiver type

The results in chapter 6 indicate that some stations perform better than other stations. In other words, there are good and bad stations differing in convergence time and accuracy. These variations are independent of the used satellite product and might originate from different receiver types (Glaner and Weber, 2021). Experience showed that Septentrio receivers tend to deliver better results than other receiver models.

The IGS stations WTZR, WTZS, and WTZZ located in Wettzell, Germany, are selected to study this in detail. These three stations are at a close distance from each other. While WTZZ and WTZR are only 1-2 meters apart, WTZS is in 65-70 meters distance from the other two stations. The stations operate with the following receiver types: Leica GR50 (WTZR), Septentrio PolaRx5TR (WTZS), and Javad TRE-3 Delta (WTZZ). Since they all are reference stations, they should be placed in similar conditions (e.g., ensuring an open sky). Indeed, the tracked satellites are identical with only minor differences.

Observation data of these three stations with an interval of 30 seconds for February 8, 2021 (doy 39) is processed with identical processing settings: GPS, GLONASS, Galileo and BeiDou observations are used in the conventional PPP model applying satellite orbits, clocks, and biases from WUM. The processed signals are listed in the upper part of table 7.4. A reset of the PPP solution is performed every 30 minutes.

---

[36] VMF Server: https://vmf.geo.tuwien.ac.at/index.html
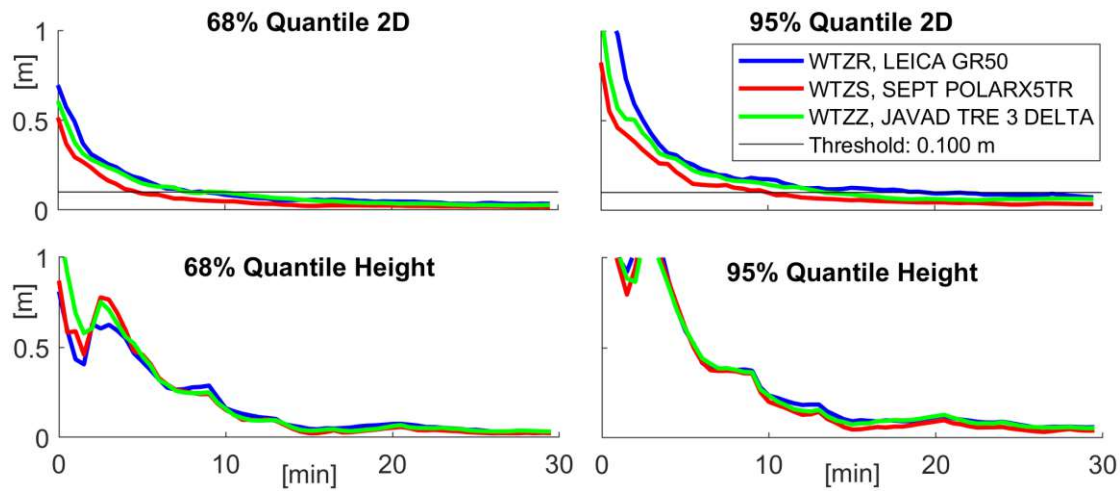
Figure 7.10: Quantile convergence for WTZR, WTZS, and WTZZ on February 8, 2021

Figure 7.10 shows the resulting 68% and 95% quantile of the 2D position difference and height component for these three stations. Furthermore, the lower part of table 7.4 shows the average convergence time, median 3D position difference of all epochs, and average 3D accuracy after 30 minutes. Although identical processing settings are used and the three station observe the same satellites, there are significant differences between the coordinate results of the three stations. WTZS (Septentrio PolaRx5TR) performs significantly better than the other two stations, and WTZZ (Javad TRE-3 Delta) slightly better than WTZR (Leica GR50). The convergence time and accuracy of WTZS are by a factor of 1.5 to 2 better than for the other two stations.

Station	WTZR	WTZS	WTZZ
Receiver type	Leica GR50	Septentrio PolaRx5TR	Javad TRE-3 Delta
Processed signals (GREC)	C1C, C2W C1C, C2P C1C, C5Q C2I, C7I	C1W, C2W C1P, C2P C1C, C5Q C2I, C7I	C1W, C2W C1P, C2P C1X, C5X C2I, C7I
Average convergence (2D <10cm) [min]	9.03	4.50	7.84
Median 3D position difference of all epochs	9.09	5.47	7.78
Average 3D accuracy after 30 minutes [cm]	4.36	2.74	3.93
Code residuals STD [m]	1.100	1.358	1.125

Table 7.4: Receiver type, processed signals, convergence time, accuracy, and residuals for WTZR, WTZS, and WTZZ on February 8, 2021

Table 7.4 also contains the standard deviation of the code observations' residuals (last

row). Interestingly, the Septentrio PolaRx5TR receiver (WTZS) does not have the smallest code residuals' standard deviation, although it provides the best coordinate solution. Actually, the residuals are even a little bit higher than for the other two receivers. However, it is possible to explain the better performance of the Septentrio PolaRx5TR receiver at the station WTZS when studying the residuals in more detail.
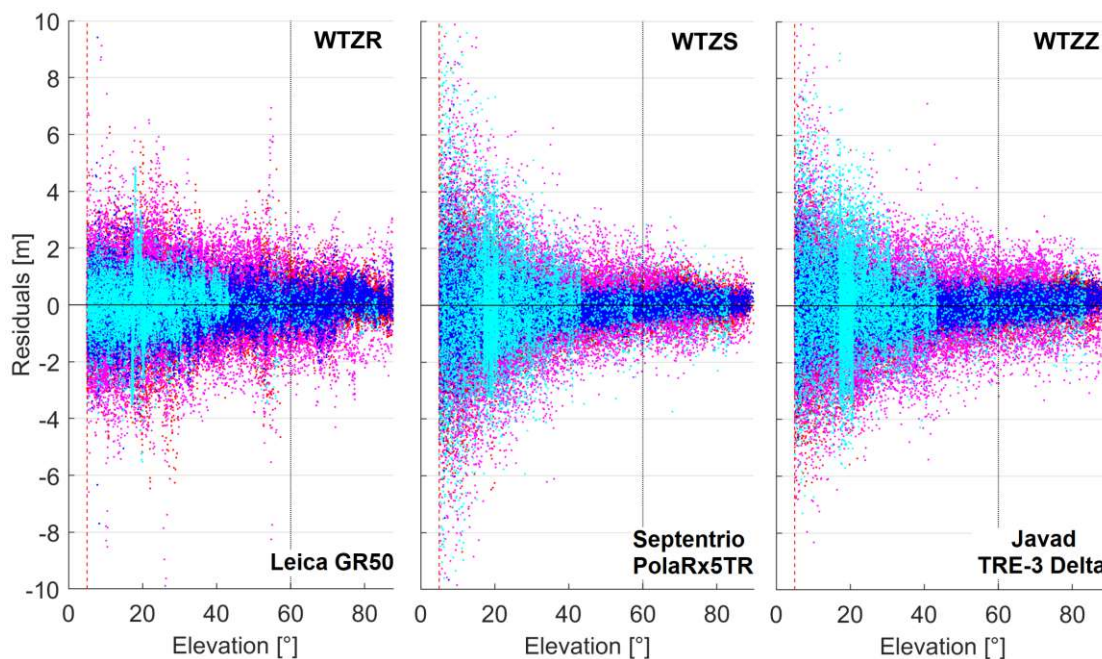
Figure 7.11: Code residuals over elevation for GPS (red), GLONASS (magenta), Galileo (blue), and BeiDou (cyan). The cutoff angle is plotted as red dashed line, and the limit for the histograms in figure 7.12 as black dotted line.

Figure 7.11 shows the code residuals of WTZR, WTZS, and WTZZ plotted over elevation for GPS (red), GLONASS (magenta), Galileo (blue), and Beidou (cyan). All three stations show a typical elevation-dependent behavior with bigger residuals for satellites in low elevation angles. The code residuals of the Septentrio PolaRx5TR (WTZS) show the strongest elevation-dependency behavior, and this receiver provides extremely precise code observations in high elevation angles (e.g., above 60°). On the other hand, the elevation dependency is significantly less pronounced for the Leica GR50 (WTZR) than for the other two receivers. Although WTZR has smaller residuals in low elevations, the Leica GR50 seems to provide less precise observations in higher elevation angles.

Figure 7.12 shows the code residuals' histogram for high elevation satellites with an elevation over 60°. The black dotted line in figure 7.11 shows this limit. The biases of all histograms are at the centimeter to decimetre level and comparable for the three receivers. When it comes to the standard deviation, we can find some differences between the histograms.

The Septentrio PolaRx5TR has the smallest code residuals for all GNSS, except for Bei-
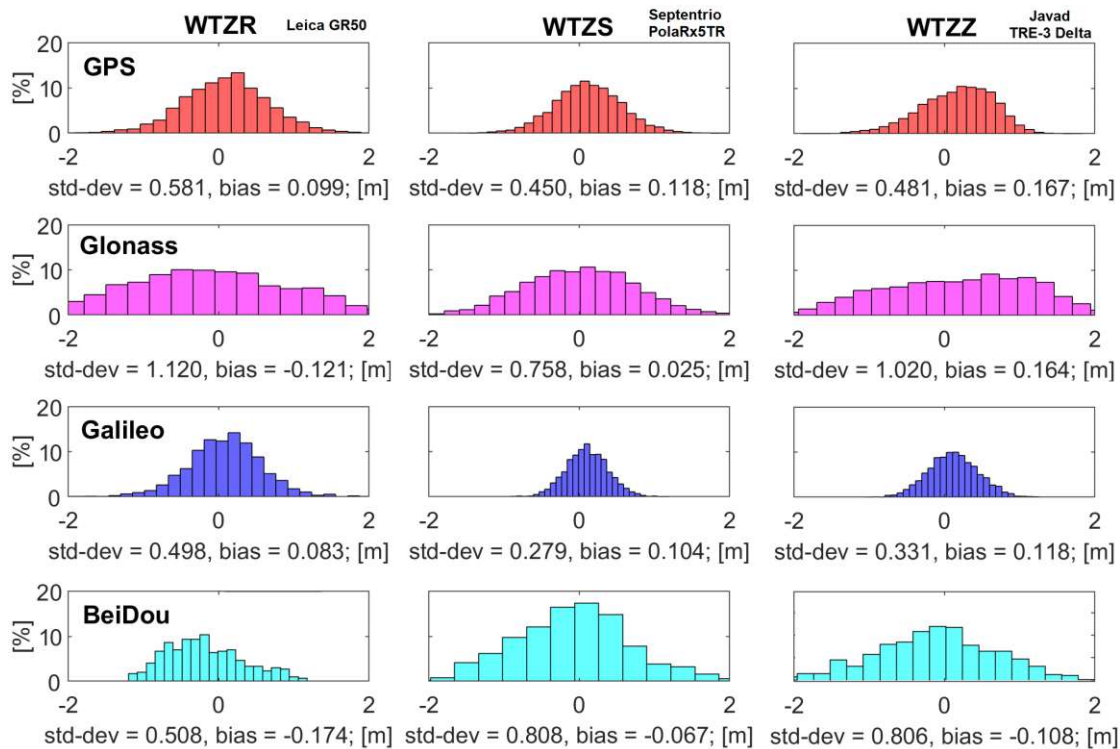
Figure 7.12: Histograms of the code residuals of high satellites (elevation over 60°) for the IGS stations WTZR, WTZS, and WTZZ on February 8, 2021

Dou. Particularly, the code residuals of high GLONASS satellites are much smaller than for the other two receivers. Due to the elevation-dependent weighting, regularly used in PPP, observations from high satellites contribute most to the solution. Therefore, the PPP solution of the Septentrio receiver performs significantly better than the PPP solution of the other two receivers.

Furthermore, because the Javad TRE-3 Delta (WTZZ) provides more precise GPS, GLONASS, and Galileo observations than the Leica GR50 (WTZR), WTZZ performs better than WTZR. Compared to the other two receivers, the code residuals of the Leica GR50 are considerably larger in high elevations.

Besides the variations between different receivers, differences in the code residuals' size between GNSS are visible in figure 7.11 (residuals over elevation) and 7.12 (histograms of high satellites' code residuals). The code observations of Galileo satellites have the smallest residuals of all processed GNSS, and they are are slightly smaller than the GPS code residuals. Furthermore, the code residuals of GLONASS and BeiDou are comparable in size and significantly larger than for Galileo and GPS. These variations are a combination of the quality of the GNSS signal, receiver tracking, and satellite product. Note that the Leica GR50 (WTZR) seems to track BeiDou significantly more precisely than the other two receivers.

Because Septentrio receivers provide more precise code observations in high elevations than other tested receivers, they tend to deliver better PPP results. Furthermore, the pro-

nounced elevation-dependent behavior of the observations' residuals is well described with the elevation-based weighting scheme. Of course, some stations might show a bad PPP performance, although they are equipped with a Septentrio receiver due to other more severe effects (e.g., Multipath).

Considering the presented residuals, a refinement of the observation weighting depending on the GNSS might improve the coordinate results (section 7.8). For example, a stronger weighting of observations from GPS and Galileo than GLONASS and BeiDou observations seems reasonable considering the presented test case.

7.8. GNSS weighting

The test case in the last section shows that the size of the code residuals and quality of observations alternates for the observations of different GNSS. Reasons might be a variable quality of the satellite products and precision of the receiver's signal tracking. Furthermore, the observation model might fit better for specific GNSS. Therefore, it is worth considering a GNSS-based observation weighting.

$$\sigma_{obs}^2 = \frac{\sigma_{obs,0}^2}{sin^2(el)} f_{GNSS} \tag{7.6}$$

In the presented equation, $\sigma_{obs,0}$ denotes the standard deviation of the raw measurements, for example, 30 cm for code and 2 mm for phase observations (section 4.4.3). In addition to the elevation-based weighting function $sin^2(el)$, a factor f_{GNSS} is introduced in equation 7.6. This factor is used to scale the variance of the observations depending on the GNSS. Ordinarily, all GNSS are weighted equally (factor 1). Ultimately, σ_{obs}^2 represents the resulting variance after elevation and GNSS weighting.

The presented GNSS weighting approach is tested using the same three IGS stations in Wettzell, observation data, period and processing settings as in the test case in section 7.7. However, the results are not assessed for each receiver individually this time. Based on the residuals shown in figure 7.12 three weighting options are introduced in table 7.5 differing in the intensity of the GNSS-based weighting.

The lower part of table 7.5 shows the resulting average convergence time and average 3D position difference after 30 minutes. Furthermore, figure 7.13 illustrates the convergence behavior of the different PPP solutions in a bar plot. The height of a bar indicates the percentage of convergence periods, which have reached convergence (2D <10 cm) using a specific weighting option at a particular point in time after the last reset. Note that the height component is not presented here because the variations are more pronounced in the horizontal position.

By applying a GNSS-based weighting on the observations, the float solution's convergence time is reduced compared to the default solution. The 'severe' weighting reduces the convergence time by about 8% and more than the other two options in this test case. 'Gentle' and

'fair' weighting equally lower the convergence by about 3%. However, all weighting options slightly decrease the accuracy, and the results suggest that a stronger weighting deteriorates accuracy more. Therefore, it might be reasonable to release the GNSS weighting over time.
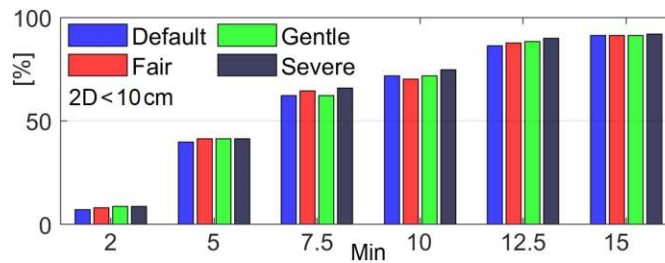
Figure 7.13: Bar plot of the float solution's convergence for different GNSS weighting options (table 7.5). The height of a bar indicates the percentage of convergence periods, which have converged at a specific point in time after the last reset.

Weighting	Default	Gentle	Fair	Severe
GPS	1	1	1.1	1.3
GLONASS	1	1.5	2	2.5
Galileo	1	1	1	1
BeiDou	1	1.5	2	2.5
Average convergence (2D <10 cm) [min]	7.23	6.99	6.99	6.66
Average 3D accuracy after 30 min [cm]	3.75	3.76	3.80	3.81

Table 7.5: The weight factors, convergence time, and accuracy for three GNSS weighting options

Since an incorrect weighting of the observations deteriorates the PPP solution and various factors like the satellite product and receiver type have to be considered in the choice of the weights, extensive tests are necessary for an optimal GNSS-based weighting. However, it seems reasonable to down-weight GLONASS and BeiDou observations because their satellite products are typically less precise. Furthermore, similar weights should be applied for GPS and Galileo observations or marginally higher weights for Galileo.

In a further step, it should be investigated if the residuals of different satellite types (e.g., BeiDou or new GPS satellites) show significant variances leading to further refinements of the observation weighting approach. Future studies should also consider frequency-dependent weighting in the uncombined model.

8. Discussion

This thesis introduced different PPP processing schemes utilizing multiple GNSS and frequencies to reduce the coordinate convergence time as far as possible. This chapter discusses the content, draws some conclusions, and provides a short outlook.

8.1. Summary and conclusions

Processing GNSS observations with an update rate of 1 second, the presented PPP schemes achieve typical convergence times of a few minutes for the float solution (2D < 10cm) and around one minute for the fixed solution (2D < 5cm). Beyond that, about fifty percent of the investigated stations show a median TTFF of one minute or below. In the case of the five best-performing stations, approximately forty percent of the convergence periods are instantaneously correctly fixed after 10 seconds. Additionally, the PPP solution offers a precise estimation of the tropospheric delay and, in the case of the uncombined model, also of the ionospheric delay.

The PPP coordinate solution provides a comparable position accuracy to relative positioning methods (e.g., RTK) either when the ambiguities are correctly fixed or in the case of the float solution after an extended convergence time (e.g., 30 minutes). Beyond that, the PPP float solution achieves higher accuracy than the fixed solution after about 30 minutes and provides an extremely high precision at the few millimeters level after, for example, 40 minutes.

These results are achieved with geodetic reference station data and post-processed satellite products. The environments might be more challenging in the surveying practice, making it more difficult to achieve such a PPP performance. When using the presented PPP models with real-time instead of post-processed satellites products the float solution performs nearly identical and the TTFF is elongated by two to three minutes. Note that the PPP approaches were not adapted to the characteristics of real-time correction streams, possibly improving the results. Furthermore, we can expect real-time satellite products to reach the same quality as post-processed satellite products for all GNSS in the future and, consequently, the corresponding fixed PPP solutions. Anyway, the presented results show that the PPP technique can keep up with relative position methods, at least under these circumstances.

The uncombined model is the future of PPP, opening up numerous possibilities to handle multi-GNSS and multi-frequency observations. This flexible PPP model excellently manages the current GNSS constellations (e.g., GPS L5), does not increase the raw observation noise, allows the inclusion of ionosphere models, and provides an estimation of the ionospheric delay. On the other hand, the conventional model is a reliable and stable approach, although showing some limitations.

The provided results demonstrate that a steady nearly-instantaneous coordinate convergence is achieved with the conventional model and ambiguity fixing. On the other hand,

the uncombined model performs better than the conventional model in the float solution. This applies particularly to the first minutes of the processing and the inclusion of BeiDou observations. Furthermore, including a third frequency in the processing generally improves the performance of the uncombined model and is not easily possible with the conventional model.

The introduced fixing process for the uncombined model is validated with Galileo observations and the satellite products of TUG. Although the fixing is less successful than its counterpart in the conventional model due to a lower number of fixable satellites, this approach shows the potential to challenge the fixed solution of the conventional model. Furthermore, there are some open issues regarding the available satellite products and antenna calibrations, which might be solved in the future.

The tests show that stations perform differently regarding all estimated parameters. One explanation is, among other things like multipath or faulty phase observations, the receiver type. Septentrio receivers perform better than other receivers due to more precise code signal tracking, especially for highly-elevated satellites. Furthermore, the observation model and fixing process might not fit other receiver types that well.

In the course of this thesis, the signals of all four globally operating GNSS were successfully processed with raPPPid. Galileo performs similar or better during the tests than GPS concerning the code observations' residuals and multi-GNSS combinations. Therefore, the satellite products of Galileo are at a comparable level to GPS, and the Galileo signals allow a more precise tracking by the receiver. Furthermore, the orbital repetition period of Galileo leads to a more changing satellite geometry and better sky coverage which may be beneficial in extensive tests. GLONASS satellites add less precise but viable observations to the float solution, and usually, a GRE solution outperforms a GE solution. Due to the FDMA technique, GLONASS is currently not used in the fixing process. Including BeiDou into the PPP solutions provides some challenges since it is not straightforward to correctly model the observations consistent with the satellite product. However, the tests show that the GREC solution including the observations of all four globally operating GNSS performs best, especially with the uncombined model.

Finally, chapter 7 illustrates open issues and problems offering the potential to further improve the PPP performance in future. Considering the presented points in the future development of PPP is essential. One example is handling the satellite attitude with the upcoming ORBEX format or appropriately weighting the observations from different GNSS. Furthermore, increasing the observation rate (e.g. 10 Hz) might be interesting to reduce the convergence time. However, the high correlation between subsequent observations has to be properly considered. Similar to the ionospheric constraint, future approaches may introduce more constraints in the PPP solution. For example, a tropospheric or height constraint may lead to faster convergence and a more stable solution, especially for kinematic and low-cost receivers facing regular signal obstructions.

8.2. Outlook

From the present perspective, it can be expected that the relevance and use of PPP will further increase - also due to upcoming markets like autonomous driving, smartphones, and other low-cost receivers. An essential step in this context is the Galileo High-Accuracy Service (HAS), enabling dm-level positioning for everyone in the near future. PPP will become more and more competitive to relative positioning methods and has the potential to overcome them. The future will show to what extent and in which application fields PPP will replace the well-established relative positioning methods like RTK. In any case, the operators of reference networks might think about providing products suitable for PPP (e.g., precise tropospheric and ionospheric delays).

The ongoing progression of satellite products from their current focus on GPS, the IF LC, and two frequencies to more flexible multi-GNSS and multi-frequency approaches will contribute to the advancement of PPP. At some point in the future PPP-AR in all kinds of PPP models and, probably, with all GNSS (e.g., GLONASS) will be possible. Furthermore, the quality of atmospheric models and RT products will increase, especially beneficial for the convergence time and TTFF of real-time solutions. Additionally, the number of GNSS satellites providing free signals at three or four frequencies will evolve (e.g., expansion of GPS L5).

Due to the flexible nature of PPP, a multitude of application fields exist, for example, the fusion with other geodetic space techniques (e.g., VLBI), the positioning of spacecraft, or reverse PPP for computing satellite orbits. Future work will concentrate on applying and adapting the presented PPP approaches to kinematic and low-quality observation data in RT or near-RT. The software raPPPid may be used and adapted, for example, to estimate tropospheric parameters from GNSS data tracked by trains (Aichinger-Rosenberger, 2021) or decimeter-level positioning with smartphone data.

A. Appendix

Statistic	Unit	Explanation
Convergence time (float solution)	[min]	The float solution has reached convergence when the 2D position difference with respect to the reference coordinates is under the threshold of 10 cm and does not exceed this limit for the remaining convergence period.
Average convergence time	[min]	The mean value of the convergence time of all convergence periods, where the float coordinate solution achieves convergence (2D < 10cm)
Median convergence time	[min]	The median value of the convergence time of all convergence periods, where the float coordinate solution achieves convergence (2D < 10cm)
Time to first fix (TTFF, fixed solution)	[min]	The TTFF is achieved when the 2D position difference of the fixed coordinates stays under the threshold of 5 cm and does not exceed this limit for the remaining convergence period.
Average TTFF	[min]	The mean value of the TTFF of all convergence periods, where the fixed coordinate solution achieves convergence (2D < 5cm)
Median TTFF	[min]	The mean value of the TTFF of all convergence periods, where the fixed coordinate solution achieves convergence (2D < 5cm)
Percentage of convergence periods without correct fix	[%]	The percentage of convergence periods which do not achieve a correct fix
Median 3D position difference of all epochs	[cm]	The median value of all 3D position differences of all epochs and convergence periods
Average 3D position difference after 15 minutes	[cm]	The mean value of the 3D position difference of all convergence periods after, for example, 15 minutes
Median 3D position difference after 15 minutes	[cm]	The median value of the 3D position difference of all convergence periods after, for example, 15 minutes

Table A.1: Detailed explanation of coordinate and convergence statistics provided in various tables in chapter 6 and 7

Station	Latitude [°]	Longitude [°]	Height [m]
AREG	-16.465	-71.493	2489.742
ASCG	-7.916	-14.333	38.354
BRUX	50.798	4.359	158.694
CIBG	-6.490	106.849	169.534
DJIG	11.526	42.847	711.812
GAMB	-23.130	-134.965	81.068
KIRU	67.857	20.968	391.348
KIT3	39.135	66.885	623.025
KOKV	22.126	-159.665	1167.930
LAUT	-17.609	177.447	90.074
LMMF	14.595	-60.996	-26.566
MAC1	-54.500	158.936	-6.259
MAS1	27.764	-15.633	197.570
MAW1	-67.605	62.871	59.633
MAYG	-12.782	45.258	-15.947
MIZU	39.135	141.133	117.427
NICO	35.141	33.396	192.145
NKLG	0.354	9.672	31.890
NNOR	-31.049	116.193	235.248
NYA2	78.930	11.859	81.914
OWMG	-44.024	-176.369	22.027
RGDG	-53.786	-67.752	32.800
UFPR	-25.448	-49.231	926.179
UNB3	45.950	-66.642	23.320
YEL2	62.481	-114.481	181.452

Table A.2: The stations used in the test case the with their approximate position

Station	Receiver type	GPS			GLONASS		Galileo		
AREG	SEPT POLARX5	C1W	C2W	C5Q	C1P	C2P	C1C	C5Q	C7Q
MAW1	SEPT POLARX5	C1C	C2W		C1P	C2P	C1C	C5Q	C7Q
YEL2	SEPT POLARX5TR	C1W	C2W	C5Q	C1P	C2P	C1C	C5Q	C7Q
BRUX	SEPT POLARX5TR	C1W	C2W	C5Q	C1P	C2P	C1C	C5Q	C7Q
KIRU	SEPT POLARX5	C1W	C2W	C5Q	C1P	C2P	C1C	C5Q	C7Q
NYA2	SEPT POLARX5	C1W	C2W	C5Q	C1P	C2P	C1C	C5Q	C7Q
MAC1	SEPT POLARX5	C1C	C2W		C1P	C2P	C1C	C5Q	C7Q
RGDG	TRIMBLE ALLOY	C1C	C2W		C1P	C2P	C1X	C5X	C7X
MAS1	SEPT POLARX5	C1W	C2W	C5Q	C1P	C2P	C1C	C5Q	C7Q
UNB3	TRIMBLE ALLOY	C1C	C2W		C1P	C2P	C1X	C5X	C7X
DJIG	SEPT POLARX5	C1W	C2W	C5Q	C1P	C2P	C1C	C5Q	C7Q
MIZU	SEPT ASTERX4	C1W	C2W	C5Q	C1C	C2P	C1C	C5Q	C7Q
LAUT	SEPT POLARX5	C1C	C2W		C1P	C2P	C1C	C5Q	C7Q
NICO	LEICA GR50	C1C	C2W	C5Q	C1C	C2P	C1C	C5Q	C7Q
OWMG	TRIMBLE ALLOY	C1C	C2W		C1P	C2P	C1X	C5X	C7X
ASCG	TRIMBLE NETR9	C1C	C2W		C1P	C2P	C1X	C5X	C7X
UFPR	TRIMBLE NETR9	C1C	C2W		C1P	C2P	C1X	C5X	C7X
GAMB	TRIMBLE NETR9	C1C	C2W		C1P	C2P	C1X	C5X	C7X
KOKV	JAVAD TRE_G3TH DELTA	C1W	C2W		C1P	C2P	C1X	C5X	C7X
KIT3	SEPT ASTERX4	C1W	C2W	C5Q	C1C	C2P	C1C	C5Q	C7Q
NKLG	SEPT POLARX5	C1W	C2W	C5Q	C1P	C2P	C1C	C5Q	C7Q
CIBG	TRIMBLE NETR9	C1C	C2W		C1P	C2P	C1X	C5X	C7X
MAYG	TRIMBLE ALLOY	C1C	C2W		C1P	C2P	C1X	C5X	C7X
NNOR	SEPT POLARX5TR	C1W	C2W	C5Q	C1P	C2P	C1C	C5Q	C7Q
LMMF	TRIMBLE ALLOY	C1C	C2W		C1P	C2P	C1X	C5X	C7X

Table A.3: Stations sorted by their mean convergence (figure 6.6). Furthermore, the receiver type and processed signals of the stations are shown.

Station	Convergence (1)			3D accuracy (2)			ZTD difference (3)		
	IF	UC2	UC3	IF	UC2	UC3	IF	UC2	UC3
AREG	4.55	4.05	4.31	4.43	4.75	4.15	1.71	1.78	1.69
MAW1	4.75	4.82	4.85	5.92	6.16	6.28	1.22	1.27	1.31
YEL2	4.65	4.65	4.60	3.66	3.96	4.19	1.06	1.09	1.06
BRUX	5.17	5.23	5.07	3.66	4.00	4.82	0.98	1.01	1.01
KIRU	5.05	5.15	4.93	3.97	4.00	4.12	1.76	1.79	1.77
NYA2	5.92	5.65	5.63	3.49	3.69	3.63	0.88	1.00	0.97
MAC1	5.33	5.28	5.32	3.98	4.16	4.22	1.00	1.02	1.02
RGDG	5.43	5.97	5.82	4.42	4.68	4.59	1.21	1.27	1.28
MAS1	5.83	6.06	5.93	5.31	5.28	5.98	2.00	2.04	2.02
UNB3	6.40	6.24	6.02	4.59	4.79	4.84	1.19	1.21	1.21
DJIG	6.85	6.53	6.27	5.55	5.73	6.12	1.84	1.93	1.91
MIZU	6.35	6.38	6.32	4.91	4.82	5.21	1.65	1.73	1.71
LAUT	6.63	6.23	6.60	5.70	6.06	6.00	2.80	2.95	2.99
NICO	6.82	6.42	7.13	4.56	4.57	5.16	1.44	1.46	1.61
OWMG	6.62	6.47	6.62	4.73	4.92	4.93	1.77	1.86	1.82
ASCG	6.85	6.82	6.62	4.90	5.41	5.02	2.32	2.39	2.41
UFPR	6.81	6.43	6.70	6.94	7.19	6.99	2.67	2.80	2.78
GAMB	6.89	6.78	6.78	6.12	6.43	6.42	3.17	3.24	3.24
KOKV	6.81	6.92	6.63	8.21	8.46	8.55	2.68	2.79	2.82
KIT3	7.87	7.80	7.44	6.21	6.36	6.31	2.58	2.76	2.56
NKLG	8.67	8.72	7.95	9.70	9.62	9.53	2.53	2.56	2.49
CIBG	8.83	8.77	8.75	7.71	7.85	7.58	2.22	2.35	2.29
MAYG	9.21	8.91	8.40	8.26	8.29	8.05	3.14	3.28	3.16
NNOR	9.03	9.13	8.77	8.32	8.29	7.81	2.67	2.84	2.77
LMMF	9.63	9.61	8.90	10.08	10.10	10.22	2.54	2.67	2.61

Table A.4: Station-wise statistics of the float solution. The stations are sorted by their mean
convergence time (figure 6.6). The column blocks list the following values:
(1) Median convergence time [min]
(2) Median 3D position difference after 15 minutes [cm]
(3) 68% quantile of the ZTD difference [cm]

Station	Receiver	TTFF (1)		No fix (2)		Accuracy (3)	
		TUG	CODE	TUG	CODE	TUG	CODE
AREG	SEPT POLARX5	0.50	0.50	23.56	14.58	3.17	2.80
BRUX	SEPT POLARX5TR	0.78	0.50	09.47	08.95	2.23	2.11
YEL2	SEPT POLARX5TR	0.83	0.62	26.04	17.19	3.06	2.22
MAW1	SEPT POLARX5	0.85	0.50	16.15	11.46	4.71	4.50
KIRU	SEPT POLARX5	0.97	1.00	17.19	08.85	2.44	2.61
DJIG	SEPT POLARX5	1.02	0.52	24.48	20.31	2.91	2.90
MAS1	SEPT POLARX5	1.08	0.88	09.90	01.04	3.73	3.44
MAC1	SEPT POLARX5	1.14	1.03	28.13	26.04	3.04	2.83
RGDG	TRIMBLE ALLOY	1.14	0.70	03.13	07.81	2.52	2.50
NYA2	SEPT POLARX5	1.17	0.50	17.37	06.77	2.59	1.88
OWMG	TRIMBLE ALLOY	1.22	1.08	09.42	22.40	2.23	2.79
MIZU	SEPT ASTERX4	1.70	0.98	11.46	12.50	3.05	2.77
ASCG	TRIMBLE NETR9	1.83	2.03	16.15	03.13	2.96	2.53
NICO	LEICA GR50	1.83	1.12	26.32	22.63	4.69	4.14
UFPR	TRIMBLE NETR9	2.06	1.73	26.04	19.27	4.38	3.92
NNOR	SEPT POLARX5TR	2.13	2.04	26.56	15.63	3.97	3.11
GAMB	TRIMBLE NETR9	2.18	1.72	26.70	21.35	5.41	4.70
UNB3	TRIMBLE ALLOY	2.61	2.14	27.37	21.05	2.28	1.99
CIBG	TRIMBLE NETR9	3.02	2.52	18.75	13.54	4.38	3.87
NKLG	SEPT POLARX5	3.10	1.60	22.51	18.75	5.38	5.05
LAUT	SEPT POLARX5	3.23	3.27	36.98	25.52	5.37	4.67
MAYG	TRIMBLE ALLOY	3.50	2.27	23.96	25.52	5.44	5.37
KIT3	SEPT ASTERX4	3.52	2.38	27.60	31.25	4.04	4.03
KOKV	JAVAD TRE_G3TH DELTA	4.00	3.82	27.60	24.48	5.29	4.82
LMMF	TRIMBLE ALLOY	4.53	4.21	21.69	22.11	4.40	4.27

Table A.5: Station-wise statistics of the conventional model's fixed solution applying TUG or
CODE products. The stations are sorted by their median convergence time when
applying TUG products (figure 6.8). The column blocks list the following values:
(1) Median TTFF [min]
(2) Percentage of convergence periods without correct fix [%]
(3) Median 3D position difference after 15 minutes [cm]

Station	Receiver	TTFF (1)	No fix (2)	Accuracy (3)
BRUX	SEPT POLARX5TR	06.12	13.12	02.85
MAS1	SEPT POLARX5	07.35	23.12	04.27
MAC1	SEPT POLARX5	07.65	21.91	03.01
AREG	SEPT POLARX5	07.78	22.58	06.40
MAW1	SEPT POLARX5	08.02	13.98	05.03
YEL2	SEPT POLARX5TR	08.10	19.34	03.48
NICO	LEICA GR50	08.27	25.27	03.86
DJIG	SEPT POLARX5	08.96	36.96	06.68
UFPR	TRIMBLE NETR9	09.35	24.73	04.84
MIZU	SEPT ASTERX4	09.41	30.68	04.66
KIRU	SEPT POLARX5	09.42	26.74	03.80
UNB3	TRIMBLE ALLOY	09.70	23.37	03.24
LAUT	SEPT POLARX5	09.98	38.55	06.97
NYA2	SEPT POLARX5	10.10	63.44	10.04
RGDG	TRIMBLE ALLOY	10.43	32.26	05.01
GAMB	TRIMBLE NETR9	10.53	27.84	06.76
ASCG	TRIMBLE NETR9	10.88	28.80	05.34
OWMG	TRIMBLE ALLOY	10.89	46.24	10.79
NNOR	SEPT POLARX5TR	11.25	48.35	11.04
KIT3	SEPT ASTERX4	11.27	43.61	06.87
MAYG	TRIMBLE ALLOY	11.82	63.39	12.98
NKLG	SEPT POLARX5	11.89	54.10	11.36
KOKV	JAVAD TRE_G3TH DELTA	12.31	60.40	09.65
CIBG	TRIMBLE NETR9	12.35	46.07	08.15
LMMF	TRIMBLE ALLOY	13.52	64.09	12.49

Table A.6: Station-wise statistics of the uncombined model's fixed solution (grE) using three frequencies and TUG products. The stations are sorted by their median convergence time. The columns list the following values:
(1) Median TTFF [min]
(2) Percentage of convergence periods without correct fix [%]
(3) Median 3D position difference after 15 minutes [cm]

Weblinks

BKG Ntrip Client. (2021). Retrieved February 10, 2021, from https://igs.bkg.bund.de/ntrip/bnc

BNC. (2021). *Manual*. Retrieved February 7, 2021, from https://software.rtcm-ntrip.org/export/HEAD/ntrip/trunk/BNC/src/bnchelp.html

Bos, M., & Scherneck, H.-G. (2021). *Free ocean tide loading provider*. Retrieved February 15, 2021, from http://holt.oso.chalmers.se/loading/index.html

CNES. (2021). *Unfixed Satellites*. Retrieved February 9, 2021, from ftp://ftpsedr.cls.fr/pub/igsac/GRG_ELIMSAT_all.dat

Drotek. (2021). *Improve your GNSS position thanks to multi-constellation and multi-frequency*. Retrieved February 7, 2021, from https://electronics.drotek.com/?p=6201

European Union Agency for the Space Programme. (2022). *Galileo Services*. Retrieved February 16, 2022, from https://www.euspa.europa.eu/galileo/services

Galileo HAS. (2021). *Info Note*. Retrieved April 15, 2021, from https://www.gsc-europa.eu/sites/default/files/sites/all/files/Galileo_HAS_Info_Note.pdf

GPS. (2021a). *Interface control document*. Retrieved February 10, 2021, from https://www.gps.gov/technical/icwg/

GPS. (2021b). *New civil signals*. Retrieved January 25, 2021, from https://www.gps.gov/systems/gps/modernization/civilsignals/

Higher Geodesy, TU Wien. (2021). Retrieved April 14, 2021, from https://hg.geo.tuwien.ac.at/

IGS. (2021). *The Receiver Independent Exchange Format*. Retrieved March 29, 2021, from https://www.igs.org/wg/rinex/#documents-formats

IGS Analysis Center Coordinator. (2021). *Experimental Multi-GNSS Combination*. Retrieved February 8, 2021, from http://acc.igs.org/mgex_experimental.html

IGS Formats and Standards. (2021). Retrieved February 7, 2021, from https://www.igs.org/formats-and-standards/

IGS Real-time Service. (2021). Retrieved February 10, 2021, from https://www.igs.org/rts

IGS Troposphere Products. (2021). Retrieved January 28, 2021, from https://www.igs.org/products/#tropospheric_products

International GNSS Service. (2021). Retrieved January 20, 2021, from https://www.igs.org/

MathWorks. (2022). *MATLAB Website*. Retrieved August 20, 2022, from https://www.mathworks.com/products/matlab.html

MGEX Products. (2021). Retrieved February 8, 2021, from https://www.igs.org/mgex/data-products#products

PPP-WIZARD. (2021). Retrieved February 10, 2021, from http://www.ppp-wizard.net/

Regina. (2021). Retrieved April 11, 2021, from https://regina.cnes.fr/en/

Royal Observatory of Belgium. (2021). *Ionosphere Tuturial*. Retrieved February 12, 2021, from http://gnss.be/ionosphere_tutorial

TARC. (2022). *BeiDou Constellation Status*. Retrieved March 4, 2022, from http://www.csno-tarc.cn/en/system/constellation

VMF Server. (2021). Retrieved January 27, 2021, from https://vmf.geo.tuwien.ac.at/index.html

Bibliography

Adavi, Z., Weber, R., & Glaner, M. F. (2022). Assessment of regularization techniques in GNSS tropospheric tomography based on single- and dual-frequency observations. *GPS Solutions*, 16.

Aggrey, J., & Bisnath, S. (2019). Improving GNSS PPP Convergence: The Case of Atmospheric-Constrained, Multi-GNSS PPP-AR. *Sensors*, *19*(3), 587. https://doi.org/10.3390/s19030587

Aichinger-Rosenberger, M. (2021). *Tropospheric parameter estimation based on GNSS tracking data of a fleet of trains* (Doctoral dissertation). Wien.

Alizadeh, M. M., Wijaya, D. D., Hobiger, T., Weber, R., & Schuh, H. (2013). Ionospheric Effects on Microwave Signals. In J. Böhm & H. Schuh (Eds.), *Atmospheric Effects in Space Geodesy* (pp. 35–71). Springer Berlin Heidelberg. https://doi.org/10.1007/978-3-642-36932-2_2

An, X., Meng, X., & Jiang, W. (2020). Multi-constellation GNSS Precise Point Positioning with multi-frequency raw observations and dual-frequency observations of ionospheric-free linear combination. *Satellite Navigation*, *1*(1), 7. https://doi.org/10.1186/s43020-020-0009-x

Askne, J., & Nordius, H. (1987). Estimation of tropospheric delay for microwaves from surface weather data. *Radio Science*, *22*(3), 379–386. https://doi.org/10.1029/RS022i003p00379

Banville, S., Geng, J., Loyer, S., Schaer, S., Springer, T., & Strasser, S. (2020). On the inter-operability of IGS products for Precise Point Positioning with ambiguity resolution. *Journal of Geodesy*, *94*(1), 10. https://doi.org/10.1007/s00190-019-01335-w

Beard, R., & Senior, K. (2017). Clocks. In P. J. G. Teunissen & O. Montenbruck (Eds.), *Springer Handbook of Global Navigation Satellite Systems* (pp. 121–164). Springer International Publishing. https://doi.org/10.1007/978-3-319-42928-1_5

Beer, S., Wanninger, L., & Heßelbarth, A. (2020). Galileo and GLONASS group delay variations. *GPS Solutions*, *24*(1), 23. https://doi.org/10.1007/s10291-019-0939-7

Böhm, J., & Schuh, H. (Eds.). (2013). *Atmospheric Effects in Space Geodesy*. Springer Berlin Heidelberg. https://doi.org/10.1007/978-3-642-36932-2

Boisits, J., Glaner, M. F., & Weber, R. (2020). Regiomontan: A Regional High Precision Ionosphere Delay Model and Its Application in Precise Point Positioning. *Sensors*, *20*(10), 2845. https://doi.org/10.3390/s20102845

REFERENCES

Cai, C., Gong, Y., Gao, Y., & Kuang, C. (2017). An Approach to Speed up Single-Frequency PPP Convergence with Quad-Constellation GNSS and GIM. *Sensors*, *17*(6), 1302. https://doi.org/10.3390/s17061302

Chen, J., Zhang, Y., Wang, J., Yang, S., Dong, D., Wang, J., Qu, W., & Wu, B. (2015). A simplified and unified model of multi-GNSS Precise Point Positioning. *Advances in Space Research*, *55*(1), 125–134. https://doi.org/10.1016/j.asr.2014.10.002

Choy, S., Bisnath, S., & Rizos, C. (2017). Uncovering common misconceptions in GNSS Precise Point Positioning and its future prospect. *GPS Solutions*, *21*(1), 13–22. https://doi.org/10.1007/s10291-016-0545-x

Cocard, M., Bourgon, S., Kamali, O., & Collins, P. (2008). A systematic investigation of optimal carrier-phase combinations for modernized triple-frequency GPS.

Collins, P., Bisnath, S., Lahaye, F., & Héroux, P. (2010). Undifferenced GPS Ambiguity Resolution Using the Decoupled Clock Model and Ambiguity Datum Fixing. *Navigation*, *57*(2), 123–135. https://doi.org/10.1002/j.2161-4296.2010.tb01772.x

De Bakker, P. F. (2016). *On User Algorithms for GNSS Precise Point Positioning* (Doctoral dissertation). Delft University of Technology. Netherlands.

Deng, Z., Fritsche, M., Nischan, T., & Bradke, M. (2016). Multi-GNSS Ultra Rapid Orbit-, Clock- and EOP-Product Series. *GFZ Data Services*. https://doi.org/https://doi.org/10.5880/GFZ.1.1.2016.003

Dow, J. M., Neilan, R. E., & Rizos, C. (2009). The International GNSS Service in a changing landscape of Global Navigation Satellite Systems. *Journal of Geodesy*, *83*(3), 191–198. https://doi.org/10.1007/s00190-008-0300-3

Dragert, H., James, T., & Lambert, A. (2000). Ocean loading corrections for continuous GPS: A case study at the Canadian coastal site Holberg. *Geophysical Research Letters*, *27*, 2045–2048. https://doi.org/10.1029/2000GL011536

Ge, M., Gendt, G., Rothacher, M., Shi, C., & Liu, J. (2008). Resolution of GPS carrier-phase ambiguities in Precise Point Positioning (PPP) with daily observations. *Journal of Geodesy*, *82*(7), 389–399. https://doi.org/10.1007/s00190-007-0187-4

Geng, J., Chen, X., Pan, Y., Mao, S., Li, C., Zhou, J., & Zhang, K. (2019a). PRIDE PPP-AR: an open-source software for GPS PPP ambiguity resolution. *GPS Solutions*, *23*(4), 91. https://doi.org/10.1007/s10291-019-0888-1

Geng, J., Chen, X., Pan, Y., & Zhao, Q. (2019b). A modified phase clock/bias model to improve PPP ambiguity resolution at Wuhan University. *Journal of Geodesy*, *93*(10), 2053–2067. https://doi.org/10.1007/s00190-019-01301-6

Geng, J., Meng, X., Dodson, A. H., & Teferle, F. N. (2010). Integer ambiguity resolution in Precise Point Positioning: method comparison. *Journal of Geodesy*, *84*(9), 569–581. https://doi.org/10.1007/s00190-010-0399-x

Glaner, M. F. (2017). *Eigenschaften und Einsatzmöglichkeiten von GPS und Galileo Signal-Linearkombinationen* (Master's thesis). Technische Universität Wien. Austria.

REFERENCES

Glaner, M. F., & Weber, R. (2021). PPP with integer ambiguity resolution for GPS and Galileo using satellite products from different analysis centers. *GPS Solutions*, *25*(3), 102. https://doi.org/10.1007/s10291-021-01140-z

Gu, S., Lou, Y., Shi, C., & Liu, J. (2015). BeiDou phase bias estimation and its application in precise point positioning with triple-frequency observable. *Journal of Geodesy*, *89*(10), 979–992. https://doi.org/10.1007/s00190-015-0827-z

Günther, C. (2018). Kepler - Satellite Navigation without Clocks and Ground Infrastructure, 849–856. https://doi.org/10.33012/2018.15997

Guo, J., Xu, X., Zhao, Q., & Liu, J. (2016). Precise orbit determination for quad-constellation satellites at Wuhan University: strategy, result validation, and comparison. *Journal of Geodesy*, *90*(2), 143–159. https://doi.org/10.1007/s00190-015-0862-9

Hadas, T., Kazmierski, K., & Sośnica, K. (2019). Performance of Galileo-only dual-frequency absolute positioning using the fully serviceable Galileo constellation. *GPS Solutions*, *23*(4), 108. https://doi.org/10.1007/s10291-019-0900-9

Håkansson, M., Jensen, A. B. O., Horemuz, M., & Hedling, G. (2017). Review of code and phase biases in multi-GNSS positioning. *GPS Solutions*, *21*(3), 849–860. https://doi.org/10.1007/s10291-016-0572-7

Hatch, R. (1982). The Synergism of GPS Code and Carrier Measurements. *Proceedings of the Third International Symposium on Satellite Doppler Positioning at Physical Sciences Laboratory of New Mexico State University*, *2*, 1213–1231.

Hauschild, A. (2017). Basic Observation Equations. In P. J. G. Teunissen & O. Montenbruck (Eds.), *Springer Handbook of Global Navigation Satellite Systems* (pp. 561–582). Springer International Publishing. https://doi.org/10.1007/978-3-319-42928-1_19

Hernández-Pajares, M., Juan, J. M., Sanz, J., Orus, R., Garcia-Rigo, A., Feltens, J., Komjathy, A., Schaer, S., & Krankowski, A. (2009). The IGS VTEC maps: a reliable source of ionospheric information since 1998. *Journal of Geodesy*, *83*(3), 263–275. https://doi.org/10.1007/s00190-008-0266-1

Héroux, P., & Kouba, J. (1995). GPS Precise Point Positioning with a Difference, 12.

Hinterberger, F. (2016). *Influence of GPS satellite orbits and clock corrections on the estimation of single difference uncalibrated phase delays* (Doctoral dissertation). Technische Universität Wien. Austria.

Hobiger, T., & Jakowski, N. (2017). Atmospheric Signal Propagation. In P. J. G. Teunissen & O. Montenbruck (Eds.), *Springer Handbook of Global Navigation Satellite Systems* (pp. 165–193). Springer International Publishing. https://doi.org/10.1007/978-3-319-42928-1_6

Hofmann-Wellenhof, B., Lichtenegger, H., & Wasle, E. (2008). *GNSS - Global Navigation Satellite Systems: GPS, GLONASS, Galileo, and more*. Springer-Verlag Wien.

REFERENCES

Hopfield, H. S. (1969). Two-quartic tropospheric refractivity profile for correcting satellite data. *Journal of Geophysical Research*, *74*(18), 4487–4499. https://doi.org/10.1029/JC074i018p04487

Hu, J., Zhang, X., Li, P., Ma, F., & Pan, L. (2020). Multi-GNSS fractional cycle bias products generation for GNSS ambiguity-fixed PPP at Wuhan University. *GPS Solutions*, *24*(1), 15. https://doi.org/10.1007/s10291-019-0929-9

Huber, K. (2015). *Precise Point Positioning with Ambiguity Resolution for real-time applications* (Doctoral dissertation). Technische Universität Graz. Austria.

Hugentobler, U., & Montenbruck, O. (2017). Satellite Orbits and Attitude. In P. J. G. Teunissen & O. Montenbruck (Eds.), *Springer Handbook of Global Navigation Satellite Systems* (pp. 59–90). Springer International Publishing. https://doi.org/10.1007/978-3-319-42928-1_3

Jekeli, C., & Montenbruck, O. (2017). Time and Reference Systems. In P. J. G. Teunissen & O. Montenbruck (Eds.), *Springer Handbook of Global Navigation Satellite Systems* (pp. 25–58). Springer International Publishing. https://doi.org/10.1007/978-3-319-42928-1_2

Johnston, G., Riddell, A., & Hausler, G. (2017). The International GNSS Service. In P. J. G. Teunissen & O. Montenbruck (Eds.), *Springer Handbook of Global Navigation Satellite Systems* (pp. 967–982). Springer International Publishing. https://doi.org/10.1007/978-3-319-42928-1_33

Kalman, R. E. (1960). A New Approach to Linear Filtering and Prediction Problems. *Journal of Basic Engineering*, *82*(1), 35–45. https://doi.org/10.1115/1.3662552

Katsigianni, G., Loyer, S., Perosanz, F., Mercier, F., Zajdel, R., & Sośnica, K. (2019). Improving Galileo orbit determination using zero-difference ambiguity fixing in a Multi-GNSS processing. *Advances in Space Research*, *63*(9), 2952–2963. https://doi.org/10.1016/j.asr.2018.08.035

Kazmierski, K., Sośnica, K., & Hadas, T. (2018). Quality assessment of multi-GNSS orbits and clocks for real-time Precise Point Positioning. *GPS Solutions*, *22*(1), 11. https://doi.org/10.1007/s10291-017-0678-6

Ke, C., Zheng, Y., & Wang, S. (2020). Characterization of Inter-System Biases in GPS + BDS Precise Point Positioning. *Applied Sciences*, *10*(14), 4968. https://doi.org/10.3390/app10144968

Klobuchar, J. A. (1987). Ionospheric Time-Delay algorithm for Single-Frequency GPS Users. *IEEE Transactions on Aerospace and Electronic Systems*, *AES-23*, 325–331. https://doi.org/10.1109/TAES.1987.310829

Kouba, J. (2015). A guide to using International GNSS Service (IGS) products.

Kouba, J., Lahaye, F., & Tétreault, P. (2017). Precise Point Positioning. In P. J. G. Teunissen & O. Montenbruck (Eds.), *Springer Handbook of Global Navigation Satellite Systems*

(pp. 723–751). Springer International Publishing. https://doi.org/10.1007/978-3-319-42928-1_25

Landskron, D., & Böhm, J. (2018a). Refined discrete and empirical horizontal gradients in VLBI analysis. *Journal of Geodesy*, *92*(12), 1387–1399. https://doi.org/10.1007/s00190-018-1127-1

Landskron, D., & Böhm, J. (2018b). VMF3/GPT3: refined discrete and empirical troposphere mapping functions. *Journal of Geodesy*, *92*(4), 349–360. https://doi.org/10.1007/s00190-017-1066-2

Langley, R., Teunissen, P. J. G., & Montenbruck, O. (2017). Introduction to GNSS. In P. J. G. Teunissen & O. Montenbruck (Eds.), *Springer Handbook of Global Navigation Satellite Systems* (pp. 3–23). Springer International Publishing. https://doi.org/10.1007/978-3-319-42928-1_1

Laurichesse, D., Mercier, F., Berthias, J.-P., Broca, P., & Cerri, L. (2009). Integer Ambiguity Resolution on Undifferenced GPS Phase Measurements and Its Application to PPP and Satellite Precise Orbit Determination. *Navigation*, *56*(2), 135–149. https://doi.org/10.1002/j.2161-4296.2009.tb01750.x

Leick, A., Rapoport, L., & Tatarnikov, D. (2015). *GPS satellite surveying* (Fourth edition). Wiley.

Li, P., Jiang, X., Zhang, X., Ge, M., & Schuh, H. (2020). GPS + Galileo + BeiDou Precise Point Positioning with triple-frequency ambiguity resolution. *GPS Solutions*, *24*(3), 78. https://doi.org/10.1007/s10291-020-00992-1

Li, X., Han, X., Li, X., Liu, G., Feng, G., Wang, B., & Zheng, H. (2021). GREAT-UPD: An open-source software for uncalibrated phase delay estimation based on multi-GNSS and multi-frequency observations. *GPS Solutions*, *25*(2), 66. https://doi.org/10.1007/s10291-020-01070-2

Li, Z., Wang, N., Hernández-Pajares, M., Yuan, Y., Krankowski, A., Liu, A., Zha, J., García-Rigo, A., Roma-Dollase, D., Yang, H., Laurichesse, D., & Blot, A. (2020). IGS real-time service for global ionospheric total electron content modeling. *Journal of Geodesy*, *94*(3), 32. https://doi.org/10.1007/s00190-020-01360-0

Liu, T., Wang, J., Yu, H., Cao, X., & Ge, Y. (2018). A New Weighting Approach with Application to Ionospheric Delay Constraint for GPS/GALILEO Real-Time Precise Point Positioning. *Applied Sciences*, *8*(12), 2537. https://doi.org/10.3390/app8122537

Liu, Y., Ye, S., Song, W., & Li, Q. (2018). Estimating the orbit error of BeiDou GEO satellites to improve the performance of multi-GNSS PPP ambiguity resolution. *GPS Solutions*, *22*(3), 84. https://doi.org/10.1007/s10291-018-0751-9

Lou, Y., Zheng, F., Gu, S., Wang, C., Guo, H., & Feng, Y. (2016). Multi-GNSS Precise Point Positioning with raw single-frequency and dual-frequency measurement models. *GPS Solutions*, *20*(4), 849–862. https://doi.org/10.1007/s10291-015-0495-8

REFERENCES

Loyer, S., Banville, S., Geng, J., & Strasser, S. (2021). Exchanging satellite attitude quaternions for improved GNSS data processing consistency. *Advances in Space Research*, S0273117721003720. https://doi.org/10.1016/j.asr.2021.04.049

Loyer, S., Banville, S., Perosanz, F., & Mercier, F. (2017). *Disseminating GNSS attitude for improved clock correction consistency*.

Loyer, S., Montenbruck, O., & Hilla, S. (2019). GNSS Attitude quaternions exchange using ORBEX. http://acc.igs.org/misc/proposal_orbex_april2019.pdf

Magnet, N. (2019). *Giomo: A robust modeling approach of ionospheric delays for GNSS real-time positioning applications* (Doctoral dissertation). Technische Universität Wien. Austria.

Malys, S., & Jensen, P. A. (1990). Geodetic point positioning with GPS carrier beat phase data from the CASA UNO Experiment. *Geophysical Research Letters*, *17*(5), 651–654. https://doi.org/https://doi.org/10.1029/GL017i005p00651

Maqsood, M., Gao, S., & Montenbruck, O. (2017). Antennas. In P. J. G. Teunissen & O. Montenbruck (Eds.), *Springer Handbook of Global Navigation Satellite Systems* (pp. 505–534). Springer International Publishing. https://doi.org/10.1007/978-3-319-42928-1_17

Montenbruck, O., Hauschild, A., & Steigenberger, P. (2014). Differential Code Bias Estimation using Multi-GNSS Observations and Global Ionosphere Maps: Multi-GNSS DCB Estimation. *Navigation*, *61*(3), 191–201. https://doi.org/10.1002/navi.64

Montenbruck, O., Hugentobler, U., Dach, R., Steigenberger, P., & Hauschild, A. (2012). Apparent clock variations of the Block IIF-1 (SVN62) GPS satellite. *GPS Solut*, 11.

Montenbruck, O., Schmid, R., Mercier, F., Steigenberger, P., Noll, C., Fatkulin, R., Kogure, S., & Ganeshan, A. (2015). GNSS satellite geometry and attitude models. *Advances in Space Research*, *56*(6), 1015–1029. https://doi.org/10.1016/j.asr.2015.06.019

Montenbruck, O., Steigenberger, P., & Hauschild, A. (2018). Multi-GNSS signal-in-space range error assessment – Methodology and results. *Advances in Space Research*, *61*(12), 3020–3038. https://doi.org/10.1016/j.asr.2018.03.041

Montenbruck, O., Steigenberger, P., Prange, L., Deng, Z., Zhao, Q., Perosanz, F., Romero, I., Noll, C., Stürze, A., Weber, G., Schmid, R., MacLeod, K., & Schaer, S. (2017). The Multi-GNSS Experiment (MGEX) of the International GNSS Service (IGS) – Achievements, prospects and challenges. *Advances in Space Research*, *59*(7), 1671–1697. https://doi.org/10.1016/j.asr.2017.01.011

Nava, B., Coïsson, P., & Radicella, S. M. (2008). A new version of the NeQuick ionosphere electron density model. *Journal of Atmospheric and Solar-Terrestrial Physics*, *70*, 1856–1862. https://doi.org/https://doi.org/10.1016/j.jastp.2008.01.015

Nie, Z., Yang, H., Zhou, P., Gao, Y., & Wang, Z. (2019). Quality assessment of CNES real-time ionospheric products. *GPS Solutions*, *23*(1), 11. https://doi.org/10.1007/s10291-018-0802-2

Nilsson, T., Böhm, J., Wijaya, D. D., Tresch, A., Nafisi, V., & Schuh, H. (2013). Path Delays in the Neutral Atmosphere. In J. Böhm & H. Schuh (Eds.), *Atmospheric effects in space geodesy* (pp. 73–136). Springer Berlin Heidelberg. https://doi.org/10.1007/978-3-642-36932-2_3

Ning, Y., Han, H., & Zhang, L. (2019). Single-frequency Precise Point Positioning enhanced with multi-GNSS observations and global ionosphere maps. *Measurement Science and Technology*, *30*(1), 015013. https://doi.org/10.1088/1361-6501/aaf0f6

Odijk, D., & Wanninger, L. (2017). Differential Positioning. In P. J. Teunissen & O. Montenbruck (Eds.), *Springer Handbook of Global Navigation Satellite Systems* (pp. 753–780). Springer International Publishing. https://doi.org/10.1007/978-3-319-42928-1_26

Pan, L., Zhang, X., & Liu, J. (2019). A comparison of three widely used GPS triple-frequency Precise Point Positioning models. *GPS Solutions*, *23*(4), 121. https://doi.org/10.1007/s10291-019-0914-3

Pan, Z., Chai, H., & Kong, Y. (2017). Integrating multi-GNSS to improve the performance of Precise Point Positioning. *Advances in Space Research*, *60*(12), 2596–2606. https://doi.org/10.1016/j.asr.2017.01.014

Paziewski, J., Sieradzki, R., & Wielgosz, P. (2018). On the Applicability of Galileo FOC Satellites with Incorrect Highly Eccentric Orbits: An Evaluation of Instantaneous Medium-Range Positioning. *Remote Sensing*, *10*(2), 19. https://www.mdpi.com/2072-4292/10/2/208

Petit, G., & Luzum, B. (Eds.). (2010). IERS Conventions 2010. In *Iers technical note* (pp. 99–119). Verlag des Bundesamts für Kartographie und Geodäsie.

Prange, L., Villiger, A., Sidorov, D., Schaer, S., Beutler, G., Dach, R., & Jäggi, A. (2020). Overview of CODE's MGEX solution with the focus on Galileo. *Advances in Space Research*, S0273117720302908. https://doi.org/10.1016/j.asr.2020.04.038

Rebischung, O., & Schmid, R. (2016). IGS14/igs14.atx: a new framework for the IGS products [poster]. *AGU Fall Meeting 2016, San Francisco, USA*.

Reussner, N., & Wanninger, L. (2011). GLONASS inter-frequency biases and their effects on RTK and PPP carrier-phase ambiguity resolution.

Revnivykh, S., Bolkunov, A., Serdyukov, A., & Montenbruck, O. (2017). GLONASS. In P. J. G. Teunissen & O. Montenbruck (Eds.), *Springer Handbook of Global Navigation Satellite Systems* (pp. 219–245). Springer International Publishing. https://doi.org/10.1007/978-3-319-42928-1_8

Richert, T., & El-Sheimy, N. (2006). Optimal linear combinations of triple frequency carrier phase data from future global navigation satellite systems. *GPS Solutions*, *11*(1), 11–19. https://doi.org/10.1007/s10291-006-0024-x

Saastamoinen, J. (1972). Atmospheric Correction for the Troposphere and Stratosphere in Radio Ranging Satellites. In S. W. Henriksen, A. Mancini, & B. H. Chovitz (Eds.),

Geophysical monograph series (pp. 247–251). American Geophysical Union. https://doi.org/10.1029/GM015p0247

Schaer, S. (2015). SINEX BIAS—Solution (Software/technique) INdependent EXchange Format for GNSS Biases Version 1.00.

Schaer, S., Gurtner, W., & Feltens, J. (1998). IONEX: The IONosphere Map EXchange Format Version 1. In J. M. Dow, J. Kouba, & T. Springer (Eds.), *Proceeding of the IGS AC Workshop* (pp. 233–247).

Seeber, G. (2003). *Satellite geodesy* (2., completely rev. and extended ed..). De Gruyter.

Seepersad, G., & Bisnath, S. (2015). Reduction of PPP convergence period through pseudo-range multipath and noise mitigation. *GPS Solutions*, *19*(3), 369–379. https://doi.org/10.1007/s10291-014-0395-3

Seepersad, G., & Bisnath, S. (2017). An assessment of the interoperability of PPP-AR network products. *The Journal of Global Positioning Systems*, *15*(1). https://doi.org/10.1186/s41445-017-0009-9

Shi, C., Gu, S., Lou, Y., & Ge, M. (2012). An improved approach to model ionospheric delays for single-frequency Precise Point Positioning. *Advances in Space Research*, *49*(12), 1698–1708. https://doi.org/10.1016/j.asr.2012.03.016

Shi, J., & Gao, Y. (2014). A comparison of three PPP integer ambiguity resolution methods. *GPS Solutions*, *18*(4), 519–528. https://doi.org/10.1007/s10291-013-0348-2

Steigenberger, P., Fritsche, M., Dach, R., Schmid, R., Montenbruck, O., Uhlemann, M., & Prange, L. (2016). Estimation of satellite antenna phase center offsets for Galileo. *Journal of Geodesy*, *90*(8), 773–785. https://doi.org/10.1007/s00190-016-0909-6

Steigenberger, P., & Montenbruck, O. (2019). Consistency of MGEX Orbit and Clock Products. *Engineering*, *6*. https://doi.org/10.1016/j.eng.2019.12.005

Strasser, S. (2022). *Reprocessing Multiple GNSS Constellations and a Global Station Network from 1994 to 2020 with the Raw Observation Approach* (Doctoral dissertation). Technische Universität Graz. Austria.

Strasser, S., Mayer-Gürr, T., & Zehentner, N. (2018). Processing of GNSS constellations and ground station networks using the raw observation approach. *Journal of Geodesy*. https://doi.org/10.1007/s00190-018-1223-2

Teunissen, P. J. G. (1995). The least-squares ambiguity decorrelation adjustment: a method for fast GPS integer ambiguity estimation. *Journal of Geodesy*, *70*(1), 65–82. https://doi.org/10.1007/BF00863419

Teunissen, P. J. G., & Khodabandeh, A. (2015). Review and principles of PPP-RTK methods. *Journal of Geodesy*, *89*(3), 217–240. https://doi.org/10.1007/s00190-014-0771-3

Teunissen, P. J. G., & Khodabandeh, A. (2019). GLONASS ambiguity resolution. *GPS Solutions*, *23*(4), 101. https://doi.org/10.1007/s10291-019-0890-7

REFERENCES

Teunissen, P. J. G., & Montenbruck, O. (Eds.). (2017). *Springer Handbook of Global Navigation Satellite Systems*. Springer International Publishing. https://doi.org/10.1007/978-3-319-42928-1

Tomasz, H. (2015). GNSS-Warp Software for Real-Time Precise Point Positioning. *Artificial Satellites*, *50*(2), 59–76. https://doi.org/10.1515/arsa-2015-0005

Urquhart, L. (2008). *An Analysis of Multi-Frequency Carrier Phase Linear Combinations for GNSS* (Senior technical report No. 263). University of New Brunswick.

Verhagen, S., & Teunissen, P. J. G. (2017). Least-Squares Estimation and Kalman Filtering. In P. J. G. Teunissen & O. Montenbruck (Eds.), *Springer Handbook of Global Navigation Satellite Systems* (pp. 639–660). Springer International Publishing. https://doi.org/10.1007/978-3-319-42928-1_22

Wang, N., Li, Z., Duan, B., Hugentobler, U., & Wang, L. (2020). GPS and GLONASS observable-specific code bias estimation: comparison of solutions from the IGS and MGEX networks. *Journal of Geodesy*, *94*(8), 74. https://doi.org/10.1007/s00190-020-01404-5

Wang, N., Yuan, Y., Li, Z., Montenbruck, O., & Tan, B. (2016). Determination of differential code biases with multi-GNSS observations. *Journal of Geodesy*, *90*(3), 209–228. https://doi.org/10.1007/s00190-015-0867-4

Wang, R., Gao, J., Zheng, N., Li, Z., Yao, Y., Zhao, L., & Wang, Y. (2019). Research on Accelerating Single-Frequency Precise Point Positioning Convergence with Atmospheric Constraint. *Applied Sciences*, *9*(24), 5407. https://doi.org/10.3390/app9245407

Wanninger, L., & Beer, S. (2015). BeiDou satellite-induced code pseudorange variations: diagnosis and therapy. *GPS Solutions*, *19*(4), 639–648. https://doi.org/10.1007/s10291-014-0423-3

Wanninger, L., Sumaya, H., & Beer, S. (2017). Group delay variations of GPS transmitting and receiving antennas. *Journal of Geodesy*, *91*(9), 1099–1116. https://doi.org/10.1007/s00190-017-1012-3

Wu, J.-T., Wu, S.-C., Hajj, G. A., Bertiger, W., & Lichten, S. (1993). Effects of antenna orientation on GPS carrier phase. *Manuscripta Geodetica*, *18*, 91–98.

Xu, G. (2007). *GPS: Theory, Algorithms and Applications*. Springer Berlin Heidelberg New York. https://doi.org/10.1007/978-3-540-72715-6

Xu, Y., Jiang, N., Xu, G., Yang, Y., & Schuh, H. (2015). Influence of meteorological data and horizontal gradient of tropospheric model on Precise Point Positioning. *Advances in Space Research*, *56*(11), 2374–2383. https://doi.org/10.1016/j.asr.2015.09.027

Zhang, H., Gao, Z., Ge, M., Niu, X., Huang, L., Tu, R., & Li, X. (2013). On the Convergence of Ionospheric Constrained Precise Point Positioning (IC-PPP) Based on Undifferential Uncombined Raw GNSS Observations. *Sensors*, *13*(11), 15708–15725. https://doi.org/10.3390/s131115708

REFERENCES

Zhou, F., Dong, D., Li, W., Jiang, X., Wickert, J., & Schuh, H. (2018). GAMP: An open-source software of multi-GNSS Precise Point Positioning using undifferenced and uncombined observations. *GPS Solutions*, *22*(2), 33. https://doi.org/10.1007/s10291-018-0699-9

Zumberge, J. F., Heflin, M. B., Jefferson, D. C., Watkins, M. M., & Webb, F. H. (1997). Precise Point Positioning for the efficient and robust analysis of GPS data from large networks. *Journal of Geophysical Research: Solid Earth*, *102*, 5005–5017. https://doi.org/10.1029/96JB03860

Zus, F., Deng, Z., & Wickert, J. (2017). The impact of higher-order ionospheric effects on estimated tropospheric parameters in Precise Point Positioning: Higher-Order Ionospheric Effects. *Radio Science*, *52*(8), 963–971. https://doi.org/10.1002/2017RS006254